Universidade do Minho
Escola de Ciências

Raquel Diana Carneiro Alves

Ionic conductivity biomembranes for application in opto-electronics

julho de 2018

FCT
Fundação para a Ciência e a Tecnologia
MINISTÉRIO DA EDUCAÇÃO E CIÊNCIA

POPH
QUALIFICAR É CRESCER.

QREN
QUADRO DE REFERÊNCIA ESTRATÉGICO NACIONAL
PORTUGAL 2007.2013

Governo da República Portuguesa

UNIÃO EUROPEIA
Fundo Social Europeu

Raquel Diana Carneiro Alves **Ionic conductivity biomembranes for application in opto-electronics**

UMinho | 2018

Universidade do Minho
Escola de Ciências

Raquel Diana Carneiro Alves

Ionic conductivity biomembranes for application in opto-electronics

Tese de Doutoramento em Ciências
Especialidade em Química

Trabalho efetuado sob a orientação da
Professora Doutora Maria Manuela da Silva Pires da Silva

julho de 2018

STATEMENT OF INTEGRITY

I hereby declare having conducted my thesis with integrity. I confirm that I have not used plagiarism or any form of falsification of results in the process of the thesis elaboration.

I further declare that I have fully acknowledged the Code of Ethical Conduct of the University of Minho.

University of Minho, 06 do julho do 2018

Full name: Raquel Diana Carmeiro Alves

Signature: Raquel Diana Carmeiro Alves

Acknowledgments

In order to avoid unfair omissions, I would like to acknowledge to all the persons who somehow contributed for the development of this work.

Firstly, I would like to acknowledge Fundação para a Ciência e Tecnologia (FCT) (grant SFRH/BD/97232/2013) for the financial support to this project.

The development of this work was only possible due the accompaniment of my supervisor. In this sense, I'm grateful for the opportunity to work with Professora Maria Manuela Silva, and so I would like to acknowledge her availability, encouragement, sympathy, patience, as well as all the scientific knowledge transmitted.

Concerning the personal domain, I would like to thank my laboratory colleagues for fellowship, and all my friends for the help, and for always believing in me and in my capabilities. Finally, I would like to acknowledge my husband, parents, brother, godfathers, for their crucial support, persistence, patience, and love paid to me throughout my academic journey, and in this way express and recognize the importance of them in my life.

Thank you everyone!

To my husband, parents, brother, and godfathers to everything…

Abstract

Polymer electrolytes (PEs) are ionically conducting materials that appeared as a good alternative to replace the traditional liquid ones. To prepare a PE, one host polymer is required to acting as a base matrix, and over the years, many polymers have been used. Natural polymers appeared as alternative of synthetic ones and chitosan has been largely investigated due to its high availability and its interesting properties. Ion conducting polymers are key materials for developing commercial devices and so the ionic conductivity is a very important parameter of an electrolyte. Thus, various approaches have been made to enhance the ionic conductivity including plasticization, addition of salts, mixed salt, and blend of polymers.

The influence of the different lanthanide salts in the chitosan matrix was evaluated. The salt concentration influences the ionic conductivity and the optimum salt amount varies depending on the lanthanide used. For the samples with 0.05 g of salt, the electrolyte with cerium triflate presented the highest conductivity values of 9.25×10^{-7} S cm^{-1} at 30ºC. In the case of the samples with 0.15 and 0.25 g of lanthanide salts, the ionic conductivity increased and reached maximum values of 9.18×10^{-7} S cm^{-1} and 1.52×10^{-6} S cm^{-1}, respectively, for the samples with europium triflate at 30ºC.

The photoluminescent properties of solid polymer electrolytes based on chitosan and europium triflate were evaluated, and these studies indicated the characteristic emission and excitation transitions of Eu^{3+}. The presence of a single peak for the $^5D_0\rightarrow{}^7F_0$ transition is an indication that europium ions occupied a single, low symmetry site in the polymeric host, which was also corroborated by the intense emission at 615 nm ($^5D_0\rightarrow{}^7F_2$ transition).

In biohybrid electrolyte doped with $LiCF_3SO_3$ and $Eu(CF_3SO_3)_3$ the ionic conductivity values in the range 5.38×10^{-6} (30ºC) to 8.77×10^{-5} (80ºC) S cm^{-1} were obtained, which are higher than those of analogous polymer electrolytes singly doped with Eu^{III} salts, and very similar to those doped with lithium salts. In a binary system of two salts: cerium and lithium triflates, the best ionic conductivity, 10^{-6} S cm^{-1} (at 30ºC), was obtained for the samples with 0.15 g of total salt amount.

In the case of the chitosan materials containing different glycerol amounts an increase in glycerol amount promotes an increase of ionic conductivity by 1 or 2 orders of magnitude, and thus these samples were chosen to assemble small electrochromic devices. The ECDs

with WO_3 electrochromic layer ($CHLnTrif_xGly_{0.70}$, for $LnTrif_x$ = $CeTrif_{0.10}$, $DyTrif_{0.15}$, and $SmTrif_{0.05}$) are almost transparent just after assembling, and after the negative potential application, the devices changed from almost transparent to blue color. This change in color is associated with WO_3 reduction and simultaneous positive ion insertion, while the application of inverse potential promotes a return of the device to its initial state, as a result of WO_3 oxidation and cation disinsertion. The ΔT varies between 3.7 - 5.3 % and 4.6 - 8.1 % at 550 and 663 nm, respectively. In the devices with PB ($CHLnTrif_xGly_{0.70}$, for $LnTrif_x$ = $DyTrif_{0.15}$, $SmTrif_{0.05}$, $ErTrif_{0.05}$, and $TmTrif_{0.05}$), during negative potential application, a reduction of PB occurs leading to the bleaching of the device, while the inverse process, coloration and/or oxidation, changes the ECD from transparent to blue. In these cases, the ΔT varies between 4.1 - 5.6 % and 4.1 - 9.2 % at 550 and 663 nm, respectively. Although in both cases, the transmittance change values are not very high, the color change differences are clearly visible in almost whole visible spectral range. Then, the obtained results showed that these electrolytes are promising materials to be applied in this kind of applications.

In plasticized chitosan-PEO electrolytes doped with europium triflate, the sample with composition 50:50 presented the highest conductivity value of 1.92×10^{-8} S cm^{-1} at 30ºC and lowest activation energy of 85.26 kJ mol^{-1}.

Resumo

Eletrólitos poliméricos (PEs) são materiais ionicamente condutores que apareceram como uma boa alternativa para substituir os tradicionais líquidos. Para preparar um PE é necessário um polímero hospedeiro, para atuar como uma matriz de base e, ao longo dos anos, muitos polímeros têm sido utilizados. Os polímeros naturais apareceram como alternativa aos sintéticos, e o quitosano tem sido amplamente investigado devido à sua elevada disponibilidade e às suas propriedades interessantes. Os polímeros condutores de iões são materiais-chave para o desenvolvimento de dispositivos comerciais e, portanto, a condutividade iónica é um parâmetro muito importante de um eletrólito. Assim, várias abordagens foram feitas para melhorar a condutividade iónica incluindo a plastificação, adição de sais, mistura de sais e mistura de polímeros.

A influência dos diferentes sais de lantanídeos na matriz de quitosano foi avaliada. A concentração de sal influencia a condutividade iónica e a quantidade ideal de sal varia de acordo com o lantanídeo utilizado. Para as amostras com 0,05 g de sal, o eletrólito com triflato de cério apresentou valores de condutividade mais altos de $9{,}25\times10^{-7}$ S cm^{-1} a 30ºC. No caso das amostras com 0,15 e 0,25 g de sais de lantanídeos, a condutividade iónica aumentou e atingiu valores máximos de $9{,}18\times10^{-7}$ S cm^{-1} e $1{,}52\times10^{-6}$ S cm^{-1}, respetivamente, para as amostras com triflato de európio a 30ºC.

As propriedades fotoluminescentes dos eletrólitos sólidos poliméricos à base de quitosano e triflato de európio foram avaliadas, e esses estudos indicaram as transições características de emissão e excitação do Eu^{3+}. A presença de um único pico para a transição $^5D_0 \rightarrow {}^7F_0$ é uma indicação de que os iões de európio ocuparam um único local de baixa simetria no hospedeiro polimérico, o que também foi corroborado pela emissão intensa a 615 nm (transição $^5D_0 \rightarrow {}^7F_2$).

No eletrólito bio-híbrido dopado com $LiCF_3SO_3$ e $Eu(CF_3SO_3)_3$, obtiveram-se os valores de condutividade iónica na faixa de $5{,}38\times10^{-6}$ (30ºC) a $8{,}77\times10^{-5}$ (80ºC) S cm^{-1}, que são superiores aos análogos eletrólitos poliméricos individualmente dopados com sais de Eu^{III} e muito similares aos dopados com sais de lítio. Em um sistema binário de dois sais: triflatos de cério e lítio obteve-se a melhor condutividade iónica, 10^{-6} S cm^{-1} (a 30ºC), para as amostras com 0,15 g de quantidade total de sal.

No caso dos materiais de quitosano com diferentes quantidades de glicerol, um aumento na quantidade de glicerol promoveu um aumento da condutividade iónica em 1 ou 2

ordens de grandeza e, portanto, essas amostras foram escolhidas para montar pequenos dispositivos electrocrómicos. Os ECDs com camada electrocrómica de WO_3 ($CHLnTrif_xGly_{0,70}$, para $LnTrif_x$ = $CeTrif_{0,10}$, $DyTrif_{0,15}$ e $SmTrif_{0,05}$) são quase transparentes logo após a montagem e, após a aplicação de potencial negativo, os dispositivos mudaram de quase transparente para cor azul. Essa mudança de cor está associada à redução do WO_3 e à inserção simultânea de iões positivos, enquanto a aplicação do potencial inverso promove o retorno do dispositivo ao seu estado inicial, como resultado da oxidação do WO_3 e desinserção de catiões. O ΔT varia entre 3,7 - 5,3% e 4,6 - 8,1% a 550 e 663 nm, respetivamente. Nos dispositivos com PB ($CHLnTrif_xGly_{0,70}$, para $LnTrif_x$ = $DyTrif_{0,15}$, $SmTrif_{0,05}$, $ErTrif_{0,05}$ e $TmTrif_{0,05}$)), durante a aplicação do potencial negativo, uma redução de PB ocorre levando ao branqueamento do dispositivo, enquanto o processo inverso, coloração e/ou oxidação, altera o ECD de transparente para azul. Nestes casos, o ΔT varia entre 4,1 - 5,6% e 4,1 - 9,2% a 550 e 663 nm, respetivamente. Embora em ambos os casos, os valores de mudança de transmitância não sejam muito altos, as diferenças de mudança de cor são claramente visíveis em quase todo o alcance espectral visível. Os resultados obtidos mostram que esses eletrólitos são materiais promissores a serem aplicados neste tipo de aplicações.

Nos eletrólitos de quitosano-PEO plastificados e dopados com triflato de európio, a amostra com composição 50:50 apresentou o maior valor de condutividade de $1{,}92 \times 10^{-8}$ S cm^{-1} a 30ºC e a menor energia de ativação de 85,26 kJ mol^{-1}.

Table of contents

List of figures

List of tables

List of symbols

σ	Ionic condictivity
σ_0	Pre-exponential factor
μ_i	Mobility of charge carriers
γ	Gyromagnetic ratio
β_e	Bohr magneton
β_n	Nuclear magneton
α, β, γ	Euler angles
τ	Lifetime
ΔT	Transmittance change
φ	Quantum yield
A	Contact area
A	Constant proportional to the number of carriers ions
A^H	Tensor
a_{iso}	Isotropic hyperfine coupling
B	Pseudo energy of activation
E_a	Apparent activation energy
g	g-factor
g_e	Electron g-factor
g_n	^{1}H nuclear g-factor
H	Spin Hamiltonian
h	Planck constant
I	Nuclear spin
I^H	^{1}H nuclear spin
n_i	Number of charge carriers
q_i	Charge of charge carriers
R	Gas constant
R_2	Charge-transfer resistance
R_b	Bulk resistance
r	Distance
T	Temperature
T	Traceless tensor
T_0	Temperature at which the configurational entropy of polymer becomes zero

T_g	Glass transition temperature
T_m	Melting point
T_{onset}	Onset temperature
t	Thickness
Z’	Real impedance
-Z’’	Imaginary impedance
Z_w	Warburg impedance

List of abbreviations

A

AFM	Atomic force microscopy

C

CA	Chitosan acetate
CH	Chitosan
CN	Carbon nanotubes
CPE	Composite polymer electrolyte
CPE_2	Double-layer capacitance
CW-EPR	X-band continuous wave

D

DNA	Deoxyribonucleic acid
DSC	Differential scanning calorimetry
DSSC	Dye-sensitized solar cell
DTGA	Differential thermogravimetric analysis

E

EC	Ethylene carbonate
ECDs	Electrochromic devices
EDFS	Echo-detected field-sweep absorption spectra
EDS	Energy-dispersive spectroscopy
EPR	Electron paramagnetic resonance
ESEEM	Electron spin echo envelope modulation

F

FTO	Fluorine thin oxide

G

Gly	Glycerol

H

HAGG	Gellan Gum
HPC	Hydroxypropylcellulose
HYSCORE	Hyperfine sublevel correlation experiments

I

ITO	Indium tin oxide

L

LECs	Light-emitting electrochemical cells
Ln	Lanthanides

N

NIR	Near-infrared

O

OD	Optical density change
OLEDs	Organic and polymer light-emitting diodes

P

PAA	Poly(acrylic acid)
PAN	Polyacrylonitrile
PB	Prussian blue
PC	Propylene carbonate
PEG	Poly(ethylene glycol)
PG	Prussiangreen
PEO	Poly(ethylene oxide)
PE	Polymer electrolyte
PMMA	Poly(methylmethacrylate)
PVA	Poly(vinyl alcohol)
PVC	Poly(vinyl chloride)
PVdF	Poly(vinylidene fluoride)
PW	Everitt's salt

R

R	Remaining structural moiety
RMS	Roughness average

S

SEM	Scanning electron microscopy
SPE	Solid polymer electrolyte

T

TGA	Thermogravimetric analysis
Trif	Triflate

U

UV	Ultraviolet

V

VTF	Vogel-Tamman-Fulcher

X

XRD	X-Ray diffraction

Chapter 1

Introduction

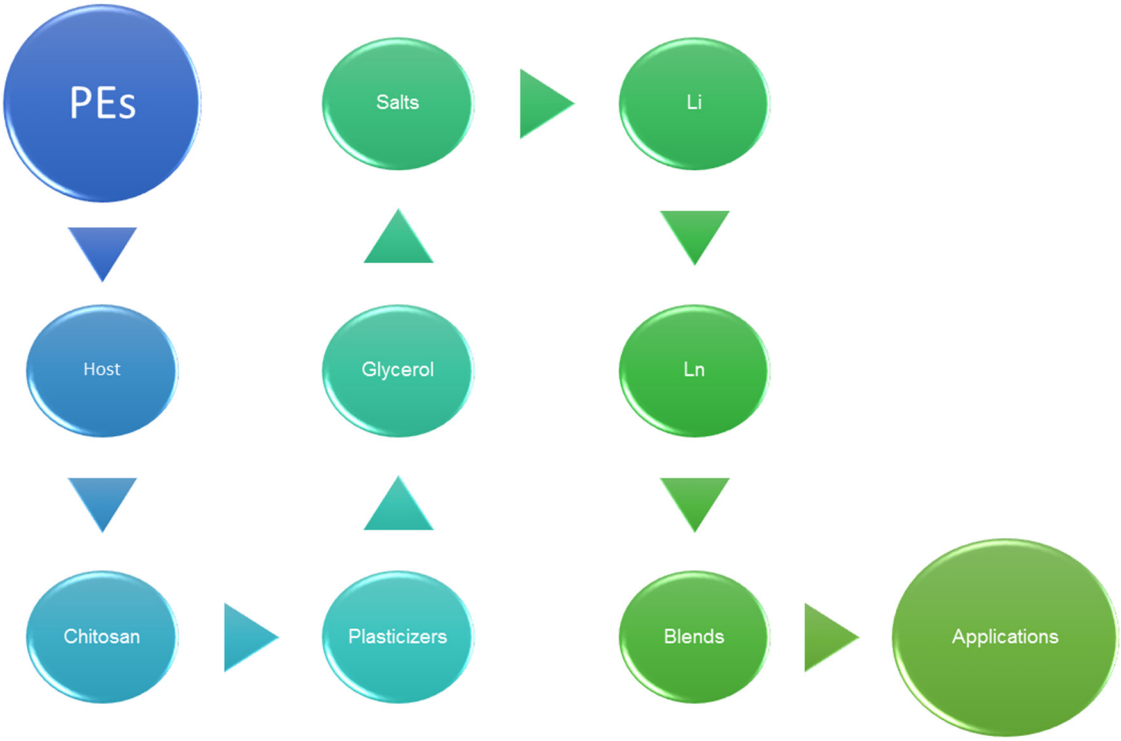

1.1. Objective

The present chapter reports a state of art of the main concepts of polymer electrolytes, namely, types, principal constituents, polymer blending and some applications, more focused on electrochromic devices, where some samples were applied. This chapter also indicates the main objectives of this work and the structure of the document.

1.2. Polymer electrolytes

Polymer electrolytes (PEs) are ionically conducting materials that appeared as a good alternative to replace the traditional liquid electrolytes [1-4]. PEs are a class of solvent-free polymer-salt complexes formed by dissolving suitable salts in high molecular weight polymers containing heteroatoms such as O, N, S, etc. [4-6]. According to the preparation routes and physical conditions of film casting, the PEs can be divided in five main categories, namely, conventional/dry solid polymer electrolytes (SPEs), plasticized polymer-salt complexes, polymer gel electrolytes, rubbery electrolytes, composite polymer electrolytes (CPEs), as can be seen in Figure 1.1 [7].

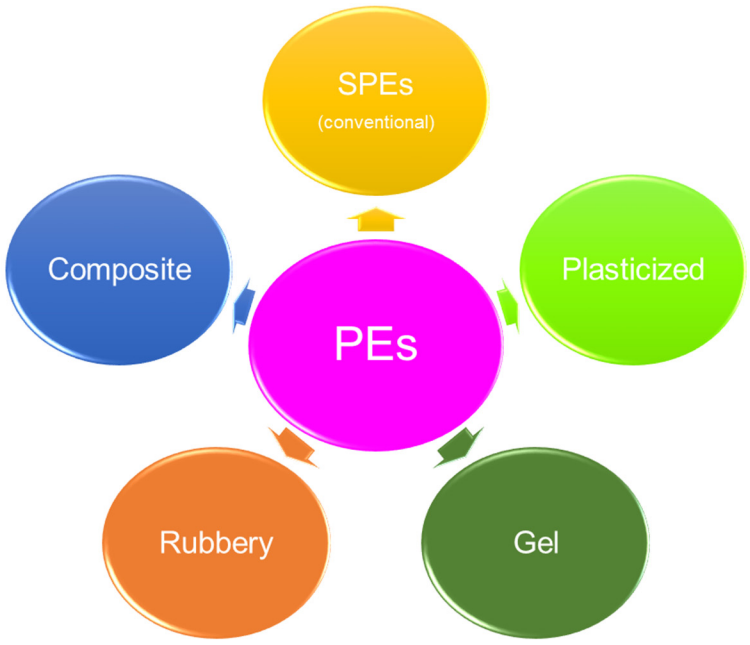

Figure 1.1 Different categories of polymer electrolytes.

SPEs are prepared usually by solvent cast method and ionic salts are dissolved in a host polymer. In plasticized polymer-salt complexes a substantial amount of plasticizers, with low molecular weight, is added into SPEs. Polymer gel electrolytes are prepared by adding a large amount of liquid solvent(s) and/or plasticizer to the SPE matrix. In rubbery electrolytes, a large amount of salt is mixed with a small amount of polymer. CPEs are prepared by dispersing a small fraction of organic/inorganic (ceramic) filler into the SPE host.

SPEs have been widely synthesized and they are systems based on solutions where salts are dissolved in an appropriate polymer matrix, that forming an ion conducting solution, and they synergize the mechanical strength and flexibility of the solid with the high ionic conductivity of the liquid state resulting in a single system ideal for the compact, and lightweight devices of the modern age [8, 9]. Since the first reports in the 70's by Wright (1975) and the subsequent recognition by Armand *et al* (1979), where they demonstrate that poly(ethylene oxide) (PEO) could dissolve lithium salts and promote ionic conductivity, SPEs have gained a lot of interest as electrolytes for solid-state electrochemical devices [10-12]. These materials have a number of desirable properties, such as, the configuration in any shape due to their flexible polymer matrix, leak free behavior, high energy density, simplified processability, no new technology requirements, improved safety and no issues related to the presence of solvent, wide electrochemical stability windows, long cycling life, good electrode-electrolyte contact, light weight, negligible vapor pressure, and environmental friendly that makes them interesting materials [2, 13-17]. However, a series of drawbacks, such as, a marked tendency to crystallize, substantially lower ionic conductivity at room temperature (10^{-8}-10^{-5} S cm^{-1}), and a tendency for to salt out, at high salt concentration, were observed and so a lot of efforts have been devoted in order to overcome these problems and improve the ionic conductivity and the mechanical properties of these materials [18].

Ion conducting polymers are key materials for developing commercial devices and so the ionic conductivity is a very important parameter of an electrolyte. The ionic transport in polymer electrolytes depends on the dielectric constant of host polymer, the salt concentration, the degree of salt dissociation, the degree of ion aggregation, and the mobility of polymer chains, and so the ionic conduction mechanism is still not well understood [19, 20].

The total ionic conductivity (σ) is a complex process related to the charge carriers and their mobility, according to the following equation 1.1:

$$\sigma = \sum n_i q_i \mu_i \tag{1.1}$$

where n_i is the number of charge carriers, and q_i and μ_i are the charge and mobility of charge carriers, respectively [21].

There are two dominant conduction mechanisms, based on the temperature dependent conductivity, that may obeys to Arrhenius (equation 1.2) or Vogel-Tamman-Fulcher (VTF) (equation 1.3) rules:

$$\sigma = \sigma_0 exp\left(\frac{-E_a}{RT}\right) \tag{1.2}$$

$$\sigma = Aexp\left[-\frac{E_a}{R(T-T_0)}\right] \tag{1.3}$$

where σ_0, E_a, R and T are the pre-exponential factor, the apparent activation energy for ion transport, the gas constant and the temperature, respectively, and A, and T_0 are the constant proportional to the number of carrier ions, and the temperature at which the configurational entropy of polymer becomes zero (suggested to be 50 K below the glass transition temperature), respectively [22, 23].

When the ionic conductivity increases linearly as a function of temperature, the system obeys to Arrhenius law and this means that the mechanism governing the ionic conductivity is due to the ion hopping between the complexation sites [24]. Due to the non-linear behavior of the ionic conductivity with temperature, the samples follow the VTF model where the ionic transport is promoted by the polymeric chain movement [25, 26]. In this case, the main mechanism of ion conduction can be related with free volume theory, and with the increase in temperature, the polymer acquires faster internal modes, the bond rotation promotes segmental motion, that favors the intra-chain ion movements and the inter-chain hopping [27].

Due to their fascinating properties, polymer electrolytes are widely studied for application in technological devices, and batteries, sensors, fuel cells, dye-sensitized solar cell, and electrochromic devices are just some examples [28].

1.2.1. Polymer host

To prepare a polymer electrolyte, one host polymer with high molecular weight is required to acting as a base matrix, and over the years, many polymers have be used for this purpose. These polymers can be classified in two main categories, and based on their sources and origins they can be synthetic or natural.

Since decades, different polymeric electrolyte systems have been extensively studied based on synthetic polymers such as PEO [6], poly(vinyl alcohol) (PVA) [29], and poly(vinyl chloride) (PVC) [30], among others. These polymers present some advantages, such as, batch-to-batch uniformity, predictable properties, and can been tailored easily [31]. On another hand, the traditional ones are non-renewable, non-biodegradable, and petroleum-based polymers, and so in recent years, great attention have be focused in polymers from renewable sources [31, 32]. Natural polymers appear as alternative of synthetic ones due to the effort to find new polymers with good mechanical and electrical properties that can act as an electrolyte in commercial devices. They are available in nature and so environmentally friendly, less expensive, and they have convenient biodegradability and biocompatibility properties [25, 33]. Polysaccharides such as chitosan [34], starch [35], cellulose [36], gelatin [37], pectin [38], gellan-gum [39] and agar-agar [40] are some candidates due to their film forming capability and abundance in nature. Chitosan appear as a promising polymer due to its fascinating properties, and its ability to form transparent films, to which salts may been added, resulting in materials with good electrochemical properties and high ionic conductivity [41]. Then, in the present work, chitosan was chosen as polymer host.

1.2.1.1. Chitosan

In nature, one can find many types of polysaccharides and chitin is the most abundant natural polymer after cellulose. Chitin, Figure 1.2, consists of 2-acetamido-2-deoxy-β-D-glucose trough a β (1→4) linkage and it is one of the important polysaccharide obtained from the exoskeleton of crustacean as well as of insects [42, 43].

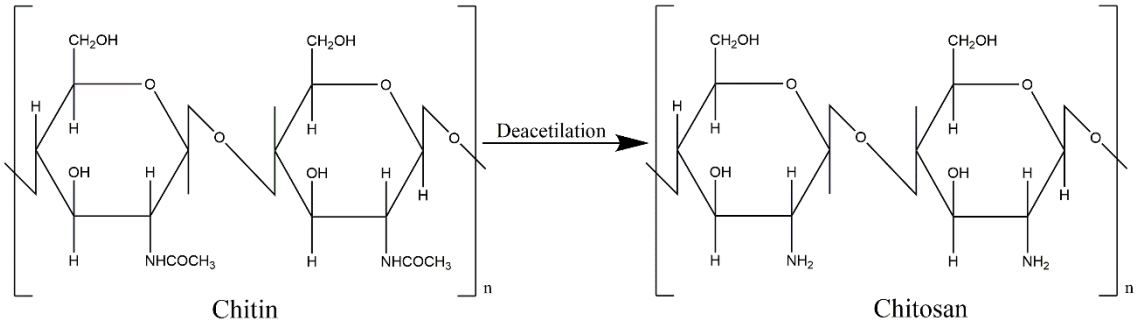

Figure 1.2 Structure of chitin and chitosan.

When chitin reaches about 50% of the degree of deacetylation, it becomes soluble in acid media and it is called chitosan [44]. Chitosan (CH) is a polymer of β-1,4-linked 2-amino-2-deoxy-D-glucopyranose derived by deacetylation of chitin and both are linear polymers [45]. It is able to dissolve in dilute acids, such as, acetic, hydrochloric, formic and burytic and normally their films were prepared using dilute acetic acid solvent [46, 47]. The chemical reaction between CH and acetic acid in aqueous medium results in a protonation of the amine group and their dissolution, as can be seen from the reaction in Figure 1.3, where NH_2 is the main functional group, R is the remaining structural moiety and CH_3COOH is the acetic acid [48]. On another hand, the lone pair electrons in the nitrogen and oxygen atom can act as electron donors, and they are responsible for its polycationic character and enables the coordination of the ions from the added salt [49, 50].

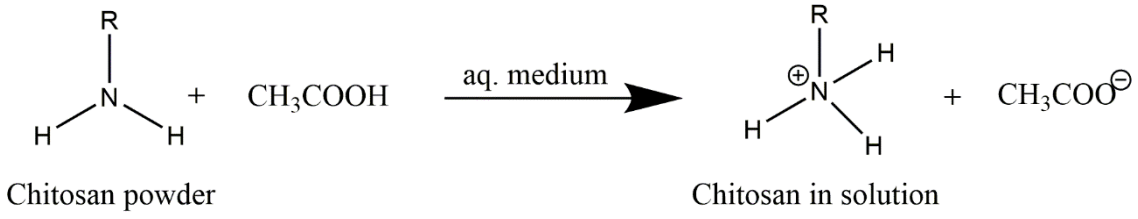

Figure 1.3 Chemical reaction between CH and acetic acid in aqueous medium [48].

CH has been largely investigated due to its high availability and also due to its interesting properties, such as, biodegradability, biocompatibility, bioactivity, non-toxicity, absorption properties, and with a wide safety margin [41, 51, 52]. Their fascinating properties make him a promising material in areas as pharmaceutical, biomedical engineering, paper production, waste water treatment, textile finishes, heavy metal chelation, and photographic products, for example [53].

CH is readily converted into beads, coatings and fibbers [54]. The films may be easily obtained by solvent cast technique, they do not possess any pores, they have high mechanical strength, and they are homogeneous [54, 55]. On another hand, due to their good chemical properties and high hydrophilicity, it is a promising candidate for the polymer host of proton conducting polymer electrolytes, as it is able to dissolve ionic salts [56, 57].

There are many studies where CH was used as polymer host and in the Table 1.1 are presented a few examples.

Table 1.1 Some examples of different CH systems.

System	Reference
CH-Phosphoric acid	[58]
CH-$NH_4CF_3SO_3$	[59]
CH-$LiCF_3SO_3$-EC	[60]
CH-$NaClO_4$	[61]
CH-oxalic acid	[62]
CH-adipic acid	[63]
CH-NH_4NO_3	[64]

In PEs, both crystalline and amorphous phases are present but it is believed that only the amorphous phase is the high conducting phase [65]. The low ionic conductivity obtained limits the SPEs applications and so various approaches have been made to enhance the amorphous region and thereby the ionic conductivity including plasticization [66], addition of salts [67], mixed salt [68], and blend of polymers [69], which are some examples.

1.2.2. Plasticizers

The addition of plasticizers to the polymer matrix has been reported as one of the most effective way to enhance the ionic conductivity [70]. These plasticizers help in: i) dissociating ions because they tend to dissociate ion-pairs into free cations and anions, which increase the number of mobile ions; ii) decrease the crystallinity by dismantling the compact periodic arrangement of polymer chains; and iii) lowering the glass transition temperature and so softens the polymer backbone and increases the molecular motion, which results in an enhancement in conductivity values [60, 71, 72]. The mechanism of how plasticizers act is not well-known yet but it is believed that they separate the polymer chain and the interactions between them and the polymer can be explained by either Van der Walls forces and/or formation of hydrogen bonds due polymer-plasticizer and polymer-polymer interactions [73]. However, the role of the plasticizer in separating the charge from polymer backbone seems to be crucial in the determination of ionic conductivity [12].

In plasticization process small organic molecules with low molecular weight, high dielectric constant and low vapor pressure, such as, ethylene carbonate (EC), poly(ethylene glycol) (PEG), propylene carbonate (PC), and glycerol (Gly) are used [40, 71]. The use of polyols, as glycerol, a fruitful and versatile plasticizer, can increase the flexibility of the final product, and assist the salt dissociation by weakening the Coulombic force between anion and cation [74, 75]. This increase in salt dissociation increases the number density of ions leading to conductivity enhancement.

The main advantage of use plasticizers consists on ease of processing into transparent membranes with good adhesion to glass and metal surfaces [76].

1.2.3. Salts

As mentioned above the main drawback of the PEs is the low ionic conductivity and one way to overcoming this shortcoming is doping the matrix with salt. Salt is an important constituent of an electrolyte because it acts as ion provider and gives strong influence on the properties of the electrolytes such as thermal stability, conductivity and amorphousness [77]. Also referred above, in polymer electrolytes the ionic conductivity has been attributed to the amorphous phase and with the dissolution of inorganic acids

and salts in a suitable polymer matrix an increase in amorphous phase is observed [78]. To choose the salt is important it has low dissociation energy, large size of anion and small size of cation [79]. It is believed that the ionic mobility is influenced by the ion-polymer interactions, the ion association and the local relaxations of the polymer, and lithium salts are often chosen because their cations are easily coordinate and solvated to exhibit ionic conductivity character [67].

According to the literature, lithium salts such as, lithium perchlorate ($LiClO_4$), lithium bis(trifluoromethanesulfonyl)imide (LiTFSI) or lithium tetrafluoroborate ($LiBF_4$), were preferably used to produce SPEs because they provide electrolytes with best conductivity values [80, 81]. $LiClO_4$ has small size of cation, large size of anion, and low dissociation energy, which allows reduce the local viscosity, facilitating the mobility of Li^+ ions within the medium, and enhances the conductivity [79]. LiTFSI is used as doping salt due to its bulk anion and low lattice energy [81]. The low lattice energy facilitates the solvation of the Li by the polymer, and to the delocalized negative charge on the nitrogen and four oxygens atoms, which reduces ion-pairing tendency and contribute to the improvement of ionic conductivity, and provide average higher conductivities than other lithium salts [82-85]. On the other hand, due to its shape and internal flexibility, the $TFSI^-$ anion has a plasticizing effect and reduces the crystallinity of the electrolytes, leading to the lowering in the T_g values. Lithium hexafluorophosphate ($LiPF_6$) was also used, and the interest in replace him is because it pose too many problems, such as, it is thermally unstable, can decompose into LiF and PF_5 and absorbing the room temperature moisture [86]. $LiBF_4$ appear as a good alternative to $LiPF_6$ as component in low temperature Li-ion batteries with improved performance [87-89]. Although its lower ionic conductivity and higher freezing temperature than the analogue $LiPF_6$, the $LiBF_4$ may be a good choice because it had lower charge-transfer resistance than $LiPF_6$ and slightly lower polarization. $LiBF_4$ is also chosen due to its low lattice energy [90].In literature, some examples of SPEs based on $LiBF_4$ have been reported, which support the acceptable levels of room temperature ionic conductivity obtained [91-93]. Although of their advantages, the lithium is intrinsically unstable and Li conducting salts still lacks many desirable properties [94]. In this way, studies of PEs containing multivalent ions, that include trivalent rare earth cations, can create new opportunities for innovative devices due to the luminescent behavior of the guest salt, and so these salts have been investigated [95].

Rare earth salts can effect considerably the structure and properties of polymer. Lanthanides (Ln) are part of the family of the rare earths and they are considered hard acids and tend to react with hard bases, especially those containing oxygen donor atoms [96, 97]. The fascinating optical properties of lanthanide ions are originated from the special features of the electronic configurations [Xe]$4f^n$ (n = 0-14, from $4f^0$ for La^{3+} to $4f^{14}$ for Lu^{3+}), which generate a rich variety of electronic levels [98]. These electronic levels have well defined energies due to the shielding of the 4f orbitals by the filled $5s^25p^6$ sub-shells that present a little variation to the chemical environments in which Ln ions are inserted, and this shielding is responsible for the specific properties of the lanthanide luminescence and the long lifetimes of the excited state [99].

In lanthanide ions three types of transitions are involved, namely: i) charge transfer transitions, ii) 4f - 5d transitions, and iii) ff transitions, and the first two occur at higher energies, and in the last one the transitions were known as corollary, sharp, and easily recognizable [100]. Most of the lanthanide ions are luminescent, some are fluorescent, some are phosphorescent, and some ions are both fluorescent and phosphorescent [101]. The fluorescent process occur without change in spin, normally $S_1 \rightarrow S_0$ transitions, as example in the case of Pr^{3+} and Er^{3+}, in phosphorescent process the transitions implying a change in spin, normally $T_1 \rightarrow S_0$ transitions, as occur for example in Sm^{3+}, Eu^{3+}, Dy^{3+}, and Tm^{3+} ions, and some ions, such as Pr^{3+}, present both fluorescent and phosphorescent transitions [102]. However, in La^{3+} and Lu^{3+} the f - f transitions are not possible and they are not luminescent, while Ce^{3+} ions have and intense d - f emission (turned from 290 to 500 nm) [101]. The emission color depends on the lanthanide ion, and Tm^{3+} emits in blue light, Tb^{3+} and Er^{3+} emits in green light, Dy^{3+} emits in yellow light, Sm^{3+} emits in orange light, Eu^{3+} emits in red light, while Ce^{3+} ions display efficient emissions in the near-UV, and Nd^{3+}, Er^{3+}, Tm^{3+} and Yb^{3+} in the NIR [23].

The interest in PEs containing trivalent lanthanides has grown considerably due to their luminescent features [103]. Little work has been published of the use of trivalent cations as mobile species in PEs but many efforts have been made to obtain polymeric materials containing rare earths ions and study their properties [104, 105]. The lanthanide ions are strongly electropositive and they have large ionic radii, from 1.061 Å for La^{3+} to 0.848 Å for Lu^{3+}, Figure 1.4 [106]. The Ln^{3+} cations have relatively large size in comparison with other trivalent cations, such as, Fe^{3+}, Cr^{3+}, Al^{3+}, etc., and so they are characterized by the weak electrostatic interactions between the cation and the negatively charged ligands, the

low capacity for covalent-bond formation, and the reduced affinity to complex formation, which are mainly formed with ionic bonds [107].

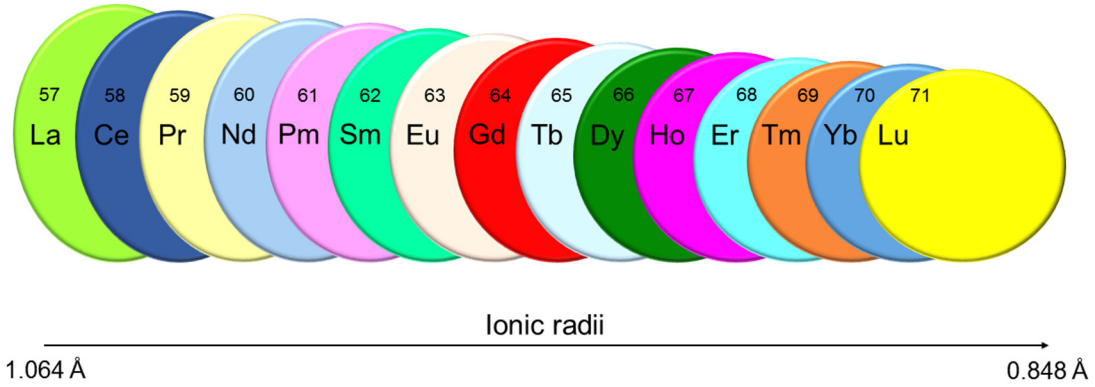

Figure 1.4 Scheme of lanthanide series, the atomic number and ionic radii behavior.

Multivalent cations have generally low mobility probably due to the large ionic radii and the strong electrostatic force between them and the polar groups of the polymeric matrix [108]. So, a binary salt system using Li salt as the auxiliary component has been produced in order to improve the performance of the electrolytes. Lithium triflate ($LiCF_3SO_3$) is a salt with great charge delocalization, which is favorable to ionic dissociation in a solvating polymer matrix, and when added to this, the increase in amorphous nature is observed, leading to the increase in the conductivity [109]. The samples with mixed cations can potentially exhibit both the emission properties due to the lanthanide ions (Ln^{3+}) and the conductivity due to the lithium ions (Li^{+}). Furthermore, in the mixed cation approaches, as mixtures of $LiCF_3SO_3$ and $Eu(CF_3SO_3)_3$ with various concentrations, the resulting electrolyte samples are white light emitters [23, 110].

1.2.4. Polymer Blending

Polymer blending is a useful technique to design PEs not only with a wide variety of properties but also with increase in the ionic conductivity and it is a promising and feasible approach to produce electrolytes in a suitable amorphous form [111]. Blending of two polymers is a method of ease of preparation that consists of mixtures of different polymers, which are miscible at molecular level, and can interact through secondary forces [78]. The characteristics of the blends are mainly dependent on the properties, and composition of its polymeric components as well as its miscibility, which is one key factor

that influences the structure and properties of the polymer blend [112]. On another hand, the choice of a common solvent used to prepare the polymer blends is very important, and at the same time, a difficult problem [113].

The main advantages of the polymer blends are the superior properties than the individual components, the easy of compositional change and so easy in control of physical properties, and also the simplicity in preparation, and the low cost [114]. The merits of using blend of polymers are exemplified in the literature by several research groups, and PVA:PAN (poly(vinyl alcohol):polyacrylonitrile), PMMA:PVdF (poly(methylmethacrylate):poly(vinylidene fluoride)), and PVA:PAA (poly(vinyl alcohol):poly(acrylic acid)) blend-based polymer electrolytes are just some examples reported [115-117].

A new class of materials can be formed with blend of natural and synthetic polymers, which results in improved mechanical properties, and biocompatibility when compared with the single ones [118]. When CH is combined with other film-forming materials their functional properties can be improved, and so blending CH with other natural and synthetic polymers is an attractive method used to improve CH's properties, and a wide of examples are referred in the literature [119, 120]. In CH blends with PVA, starch and hydroxypropylcellulose (HPC) revealed improving stability in the blends [121]. In CH:methylcellulose system, the semi-crystalline domain of pure polymers decrease upon blending [114]. In CH:starch films, the crystalline structure of CH depressed with the addition of starch, and a broad amorphous peak appeared [122].

Blending of CH with synthetic polymers have been reported to improve the mechanical properties of the films based on CH [123]. PEO ($(-CH_2CH_2O-)_n$) is a synthetic polymer with high water solubility, relatively poor mechanical and physical properties, and it was chosen as a second component because it is a flexible-chain polymer, a biologically inert material, and would greatly change the properties of the blends [124, 125]. It is also widely used as host polymer in PEs because it is able to solvate a variety of inorganic salts but its high crystallinity is a major barrier for ion transport [126]. CH and PEO have common properties, such as, biocompatibility and biodegradability, they are soluble in aqueous solutions, and on another hand, they can dissolve salts, and so they can be used as matrix in PEs [127].

CH and PEO blends were prepared in aqueous acetic acid solution by solvent casting technique and the remaining acetic acid can exhibit protonic conduction, and make in these blends a useful functionality [128]. The amine and hydroxyl groups of CH can interact with the ether groups of PEO and provides a homogeneous polymer blend that exhibit improvement in thermal, mechanical and electrical properties [128]. The amorphous nature of CH chains may facilitate a decrease in crystallinity and on another hand, may decrease the water solubility, and improve the mechanical properties of PEO, while the PEO make the blended films colorless and their flexible chains may compensate the rigidity of CH [129]. Blending CH with PEO it is expected to create more "donor sites" for the ions to hop throughout the material leading to an increase in conductivity, and in CH:PEO+NH_4I, the blending promotes an increase in the electrolyte's flexibility, and in ions mobility, leading to the enhancement in conductivity [130].

1.2.5. Applications

1.2.5.1. Electrochromic devices

Chromogenic materials can be photochromic, thermochromic, and electrochromic, and they change their light absorption/reflection level and their color as a function of light intensity, temperature and applied potential, respectively [131]. Electrochromic materials can change their color when an external potential is applied, and this color change should be reversible when the polarity is reversed [80]. Electrochromic devices (ECDs) are opto-electrochemical systems with interesting behavior to be applied in many applications, namely, sunroofs, skylight, shades, visor or rear view mirrors for automotive, and mass transportation applications, windows ("smart windows"), displays, and other electro-optical devices [132, 133].

There are many configurations of ECDs with layers of different compositions, and prepared by various techniques, and typically, an ECD has five-layer structure, as can be seen in Figure 1.5, composed by a glass substrate, a transparent conductor, an ion storage coating, an ionic conductor, and an electrochromic coating.

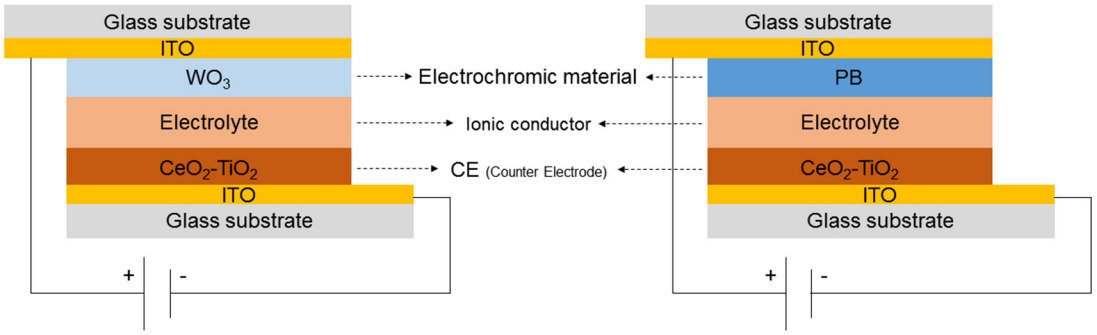

Figure 1.5 Typical configuration of ECDs with different layers.

The transparent conductors appear as the top and bottom electrodes and ITO (indium tin oxide) and FTO (fluorine thin oxide) are commonly used [134].

The ion storage (counter electrode) is needed to balance the charges shutted from the electrochromic layer through the electrolyte, and CeO_2 (cerium oxide), NiO (nickel oxide) and IrO_2 (iridium oxide) are promising materials to be used [134]. Pure or modified CeO_2 thin films can serve as transparent ion storage coating in ECDs. The films CeO_2-TiO_2 (titanium dioxide) of mixed structure showed optical transparency and good electrochemical properties with ability to insert/extract large charge densities, and they can be achieved by sol-gel and dip-coating technique is a common method of film deposition [135-137].

The electrolyte is an important constituent of an ECD, and therefore is must have some characteristics, such as, high transparency, adequate room temperature conductivity, mechanical flexibility, low thermal expansion or component volatility [138]. Many ECDs have been reported with electrolytes based on natural polymers and in Table 1.2 are presented some examples.

Table 1.2 Some ECDs with electrolytes based on natural polymers.

Configuration	Reference
WO_3/Starch-Glycerol/CeO_2-TiO_2	[139]
PB/DNA-Er$(CF_3SO_3)_3$/CeO_2-TiO_2	[140]
WO_3/Gelatin-Zn$(CF_3SO_3)_2$/CeO_2-TiO_2	[141]
WO_3/Agar-Mg$(CF_3SO_3)_2$/CeO_2-TiO_2	[142]
PB orWO_3/Chitosan-Tm$(CF_3SO_3)_3$/CeO_2-TiO_2	[143]

Several electroactive species have been used as electrochromic materials, such as, inorganic transition metal oxides (WO_3, IrO_2, MoO_3), hexacyanometallates ($[Fe^{III}Fe^{II}(CN)_6]^-$), viologens (bipyridilium compounds), and conjugated polymers [144].

Tungsten trioxide (WO_3) is one of the first studied electrochromic oxides [140]. ECDs with WO_3 films have been extensively studied [145], and the reaction in equation (1.4) ascribed the transitions and they are responsible for the peaks observed in the voltammograms:

$$\underset{\text{Colorless}}{WO_3} + xM^+ + xe^- \leftrightharpoons \underset{\text{Blue Color}}{M_xWO_3} \tag{1.4}$$

where the cation M^+ can be either H^+ or a metal ion [134]. After the negative potential application, the WO_3 reduction by simultaneous electrons and ions insertion leads to the coloration of the device, from transparent to blue color. Upon reversing the polarity of the applied voltage, the WO_3 is oxidized and the ions are extracted leading to the bleaching of the device that returns to its initial state (transparent).

Prussian Blue (PB) was discovered to the 18th century, and it is a well-known material whose electrochromic properties were observed in 1978 [146]. It is obtained by electrodeposition and it changes it color from blue to transparent [140]. PB, also called ferric ferrocyanide, is a famous electrochromic material extensively studied and it is the first synthetic pigment, whose it's molecule ($Fe_4[Fe(CN)_6)_3]$ nH_2O) is used in a variety of applications [147, 148]. There are two forms of PB, namely, insoluble and soluble, and the reactions in equations 1.5 and 1.6 ascribed the transitions and they are responsible for the four peaks observed in the voltammograms that are characteristic to the PB [140]:

$$\underset{\text{Water insoluble PB}}{Fe_4^{3+}[Fe^{2+}(CN)_6]_3} + 4K^+ + 4e^- \leftrightharpoons \underset{\text{Everitt's salt (PW)}}{K_4Fe_4^{2+}[Fe^{2+}(CN)_6]_3} \tag{1.5}$$

$$\underset{\text{Water insoluble PB}}{Fe_4^{3+}[Fe^{2+}(CN)_6]_3} - 3e^- + 3A^- \leftrightharpoons \underset{\text{Prussiangreen (PG)}}{Fe_4^{3+}[Fe^{3+}(CN)_6A^-]_3} \tag{1.6}$$

The ECD is initially blue color and after the negative potential application, the reduction of PB occur leading to the PW, and the bleaching of the device, that becomes transparent. In the inverse process, the oxidation of PW occurs and the device returns to initial state (blue color).

1.2.5.2 Other devices

Li-based batteries have dominated the portable electronic industry and the use of PEs instead of the liquid ones in these batteries allowed an enhancement in mechanical strength and safe use [149]. The polymer electrolyte plays a key role in the electrochemical properties of the batteries and it can act as a medium to transport the ions involved in the charging/discharging cycle of the cell [150, 151]. Lithium ion batteries have been widely used in technological devices due to their high energy and power density, and their main characteristics are no memory effect, many charge/discharge cycles, light in weight, cheap, and environmentally friendly [152, 153].

"Stimuli-responsive" materials, such as sensors and actuators, are devices with ability to undergo a reversible change upon exposure to an external stimulus, such as, changes in pH, temperature, and electrolyte concentration [154]. In these materials, the classical liquid electrolytes have been replaced by SPEs due to its main drawbacks, like as, drying or leakage of the electrolyte, which limits the sensor's lifetime and impair its function [155]. In electrochemical sensors, the most common SPE has a commercial name Nafion and it is a copolymer manufactured by DuPont, USA [155].

Fuel cells are devices that directly convert chemical energy stored in fuels, for example hydrogen, to electrical energy [156]. These cells are preferable over other energy conversion devices due to their advantages, such as, high efficiency of energy conversion, savings in fossil fuels, low pollution, noise, and maintenance costs emissions [157]. The PE membrane is responsible for proton transport from the anode to the cathode, and so by fuel cell's performance [158].

A dye-sensitized solar cell (DSSC) consists of a dye-coated mesoporous oxide sandwiched between two conductive transparent electrodes and an electrolyte [159]. The TiO_2 has been choice as mesoporous material and traditionally the electrolyte was liquid and containing redox couple iodide/triiodide (I^-/I^{3-}), which acts as medium to regenerate

the photo excited dye molecules [160, 161]. Due to the potential problems caused by the use of these electrolytes, such as leakage and volatilization of the liquid, some researches have been reported the high-performance of DSSC with SPEs [159].

Light-emitting electrochemical cells (LECs) provide an alternative way for achieving light emission, and they consist of an ionic luminescent material in an ionic environment sandwiched between two electrodes [162, 163]. They appear in order to try to solve limitations of OLEDs (organic and polymer light-emitting diodes), and when compared both, the LECs have a much simpler architecture [163]. LECs can be easily prepared via solution-based technologies (spin-coating, printing or slot-die coating) and they are simple single-layer devices [164].

1.3. Outline

The main objective of this thesis was develop new PEs based on natural polymers and containing rare earth ions, via solvent casting method. Furthermore, the properties of the materials were evaluated by several techniques, and in some cases, their luminescent features and their performance when applied in ECDs were investigated.

The present thesis is divided in 9 chapters, and practically all of them are based on published or submitted scientific papers.

Chapter 1 presents a literature review with a general overview on PEs, namely, their constitution and practical applications. Finally, the main goals and the structure of the document are also reported in this chapter.

The **chapter 2** is dedicated to the experimental section, where the samples preparation and the techniques used to characterize the electrolytes are described.

The **chapter 3** reports the effect of the different lanthanide salts in the CH matrix. The influence of the kind of salt and their quantity in the properties of the materials are reported.

Chapter 4 shows the luminescent properties of CH-based electrolytes doped with europium triflate.

In **chapter 5** a fundamental investigation of CH based luminescent materials doped with Eu^{III} and Li^{I} triflate salts, from the structural, photophysical and conducting points of view is perform.

Chapter 6 shows the characterization of SPEs using CH matrix doped with cerium and lithium triflates binary salt composition.

Chapter 7 reports the effect of the glycerol amount in the CH samples. Also in this chapter, some electrolytes are applied in small ECDs and their performance are evaluated.

In **chapter 8** CH and PEO powders were mixed in different ratios, and the effect of the blending of polymers is evaluated.

Finally, **chapter 9** presents the overall conclusions and suggestions for future work.

1.4. References

[1] R. Leones, F. Sentanin, L.C. Rodrigues, I.M. Marrucho, J.M.S.S. Esperança, A. Pawlicka, M. Silva, Investigation of polymer electrolytes based on agar and ionic liquids, Express Polymer Letters, 6 (2012) 1007-1016.

[2] A. Wang, H. Xu, Q. Zhou, X. Liu, Z. Li, R. Gao, N. Wu, Y. Guo, H. Li, L. Zhang, A new all-solid-state hyperbranched star polymer electrolyte for lithium ion batteries: synthesis and electrochemical properties, Electrochimica Acta, 212 (2016) 372-379.

[3] F.M. Gray, Polymer Electrolytes, Royal Society of Chemistry, Cambridge, 1997.

[4] F.M. Gray, Solid Polymer Electrolytes: Fundamentals and Technological Applications, Wiley, 1991.

[5] K. Sownthari, S.A. Suthanthiraraj, Synthesis and characterization of an electrolyte system based on a biodegradable polymer, Express Polymer Letters, 7 (2013) 495-504.

[6] M.M. Silva, M.J. Smith, Morphology and conductivity of electrolytes based on poly(ethylene oxide)-Eu(ClO_4)$_3$ films, Ionics, 3 (1997) 134-138.

[7] R.C. Agrawal, G.P. Pandey, Solid polymer electrolytes: materials designing and all-solid-state battery applications: an overview, Journal of Physics D: Applied Physics, 41 (2008) 223001 (18pp).

[8] E. Raphael, C.O. Avellaneda, M.A. Aegerter, M.M. Silva, A. Pawlicka, Agar-based gel electrolyte for electrochromic device application, Molecular Crystals and Liquid Crystals, 554 (2012) 264-272.

[9] B. Chatterjee, N. Kulshrestha, P.N. Gupta, Nano composite solid polymer electrolytes based on biodegradable polymers starch and poly vinyl alcohol, Measurement, 82 (2016) 490-499.

[10] P.V. Wright, Electrical conductivity in ionic complexes of poly(ethylene oxide), Polymer International, 7 (1975) 319-327.

[11] M.B. Armand, J.M. Chabagno, M. Duclot, Fast ion transport in solids, in: P. Vashista, J.N. Mundy, G.K. Shenoy ed., North-Holland, Amsterdam, 1979, pp. 131-136.

[12] A. Pawlicka, A.C. Sabadini, E. Raphael, D.C. Dragunski, Ionic conductivity thermogravimetry measurements of starch-based polymeric electrolytes, Molecular Crystals and Liquid Crystals, 485 (2008) 804-816.

[13] A. Perea, M. Dontigny, K. Zaghib, Safety of solid-state Li metal battery: Solid polymer versus liquid electrolyte, Journal of Power Sources, 359 (2017) 182-185.

[14] N. Shukla, A.K. Thakur, Role of salt concentration on conductivity optimization and structural phase separation in a solid polymer electrolyte based on PMMA-$LiClO_4$, Ionics, 15 (2009) 357-367.

[15] P.C. Barbosa, L.C. Rodrigues, M.M. Silva, M.J. Smith, Characterization of $pTMC_nLiPF_6$ solid polymer electrolytes, Solid State Ionics, 193 (2011) 39-42.

[16] C.-W. Liew, H.M. Ng, A. Numan, S. Ramesh, Poly(Acrylic acid)-Based Hybrid Inorganic-Organic Electrolytes Membrane for Electrical Double Layer Capacitors Application, Polymers, 8 (2016) 179 (17pp).

[17] M.F. Shukur, R. Ithnin, M.F.Z. Kadir, Electrical characterization of corn starch-LiOAc electrolytes and application in electrochemical double layer capacitor, Electrochimica Acta, 136 (2014) 204-216.

[18] R. Leones, F. Sentanin, L.C. Rodrigues, R.A.S. Ferreira, I.M. Marrucho, J.M. Esperança, A. Pawlicka, L.D. Carlos, M.M. Silva, Novel polymer electrolytes based on gelatin and ionic liquids, Optical Materials, 35 (2012) 187-195.

[19] S.L. Agrawal, M. Singh, M. Tripathi, M.M. Dwivedi, K. Pandey, Dielectric relaxation studies on [PEO-SiO_2]:NH_4SCN nanocomposite polymer electrolyte films, Journal of Materials Science, 44 (2009) 6060-6068.

[20] S.B. Aziz, Z.H.Z. Abidin, Electrical conduction mechanism in solid polymer electrolytes: new concepts to arrhenius equation, Journal of Soft Matter, 2013 (2013) (8pp).

[21] S.B. Aziz, M.F.Z. Kadir, Z.H.Z. Abidin, Structural, morphological and electrochemical impedance study of CS:LiTf based solid polymer electrolyte:

Reformulated Arrhenius equation for ion transport study, International Journal of Electrochemical Science, 11 (2016) 9228-9244.

[22] K. M. Diederichsen, H. G. Buss, B. D. McCloskey, The Compensation Effect in the Vogel-Tammann-Fulcher (VTF) Equation for Polymer-Based Electrolytes, Macromolecules 50 (2017) 3831-3840.

[23] R. Alves, L.P. Ravaro, A. Pawlicka, M.M. Silva, A.S.S. de Camargo, Eco-Friendly Luminescent Hybrid Materials Based on Eu^{III} and Li^{I} Co-Doped Chitosan, Journal of the Brazilian Chemical Society, 26 (2015) 2590-2597.

[24] A. Firmino, J.G. Grote, F. Kajzar, I. Rau, A. Pawlicka, Application of DNA In Electrochromic Cells with Switchable Transmission, Nonlinear Optics and Quantum Optics: Concepts in Modern Optics, 42 (2011) 181-201.

[25] Y.O. Iwaki, M.H. Escalona, J.R. Briones, A. Pawlicka, Sodium alginate-based ionic conducting membranes, Molecular Crystals and Liquid Crystals, 554 (2012) 221-231.

[26] J.R. Andrade, E. Raphael, A. Pawlicka, Plasticized pectin-based gel electrolytes, Electrochimica Acta, 54 (2009) 6479-6483.

[27] R. Leones, J.M.S.S. Esperança, A. Pawlicka, V. de Zea Bermudez, M.M. Silva, Polymer electrolyte based on DNA and N,N,N-trimethyl-N-(2-hydroxyethyl) ammonium bis(trifluoromethylsulfonyl)imide, Journal of Electroanalytical Chemistry, 748 (2015) 70-75.

[28] K.S. Ngai, S. Ramesh, K. Ramesh, J.C. Juan, A review of polymer electrolytes: fundamental, approaches and applications, Ionics, 22 (2016) 1259-1279.

[29] Y.-D. Kim, Y.-K. Jo, N.-J. Jo, Electrochemical performance of poly(vinyl alcohol)-based solid polymer electrolyte for lithium polymer batteries, Journal of Nanoscience and Nanotechnology, 12 (2012) 3529-3533.

[30] S. Ramesh, A.H. Yahaya, A.K. Arof, Dielectric behaviour of PVC-based polymer electrolytes, Solid State Ionics, 152 (2002) 291-294.

[31] D.R. Lu, C.M. Xiao, S.J. Xu, Starch-based completely biodegradable polymer materials, Express Polymer Letters, 3 (2009) 366-375.

[32] C.-W. Liew, S. Ramesh, K. Ramesh, A.K. Arof, Preparation and characterization of lithium ion conducting ionic liquid-based biodegradable corn starch polymer electrolytes, Journal of Solid State Electrochemistry, 16 (2012) 1869-1875.

[33] F. Xie, B.M. Flanagan, M. Li, P. Sangwan, R.W. Truss, P.J. Halley, E.V. Strounina, A.K. Whittaker, M.J. Gidley, K.M. Dean, Characteristics of starch-based films plasticised

by glycerol and by the ionic liquid 1-ethyl-3-methylimidazolium acetate: A comparative study, Carbohydrate Polymers, 111 (2014) 841-848.

[34] M.F. Shukur, Y.M. Yusof, S.M.M. Zawawi, H.A. Illias, M.F.Z. Kadir, Conductivity and transport studies of plasticized chitosan-based proton conducting biopolymer electrolytes, Physica Scripta, 2013 (2013) 014050.

[35] A.S.A. Khiar, A.K. Arof, Conductivity studies of starch-based polymer electrolytes, Ionics, 16 (2010) 123-129.

[36] N.H.B. Ahmad, M.I.N.B.M. Isa, Proton conducting solid polymer electrolytes based carboxymethyl cellulose doped ammonium chloride: ionic conductivity and transport studies, International Journal of Plastics Technology, 19 (2015) 47-55.

[37] R.I. Mattos, A. Pawlicka, J.F. Lima, C.E. Tambelli, C.J. Magon, J.P. Donoso, Magnetic resonance and conductivity study of gelatin-based proton conductor polymer electrolytes, Electrochimica Acta, 55 (2010) 1396-1400.

[38] J.P. Mendes, J.M.S.S. Esperança, M.J. Medeiros, A. Pawlicka, M.M. Silva, Structural, morphological, ionic conductivity, and thermal properties of pectin-based polymer electrolytes, Molecular Crystals and Liquid Crystals, 643 (2017) 266-273.

[39] I.S.M. Noor, S.R. Majid, A.K. Arof, D. Djurado, S.C. Neto, A. Pawlicka, Characteristics of gellan gum-$LiCF_3SO_3$ polymer electrolytes, Solid State Ionics, 225 (2012) 649-653.

[40] E. Raphael, C.O. Avellaneda, B. Manzolli, A. Pawlicka, Agar-based films for application as polymer electrolytes, Electrochimica Acta, 55 (2010) 1455-1459.

[41] R.I. Mattos, E. Raphael, S.R. Majid, A.K. Arof, A. Pawlicka, Enhancement of electrical conductivity in plasticized chitosan based membranes, Molecular Crystals and Liquid Crystals, 554 (2012) 150-159.

[42] M.N.V.R. Kumar, A review of chitin and chitosan applications, Reactive and functional polymers, 46 (2000) 1-27.

[43] A. Toffey, G. Samaranayake, C.E. Frazier, W.G. Glasser, Chitin derivatives. I. Kinetics of the heat-induced conversion of chitosan to chitin, Journal of Applied Polymer Science, 60 (1996) 75-85.

[44] M. Rinaudo, Chitin and chitosan: properties and applications, Progress in Polymer Science, 31 (2006) 603-632.

[45] Z. Osman, Thermal and conductivity studies of chitosan acetate-based polymer electrolytes, Ionics, 11 (2005) 397-401.

[46] S. Demarger-Andre, A. Domard, Chitosan carboxylic acid salts in solution and in the solid state, Carbohydrate Polymers, 23 (1994) 211-219.

[47] T. Winie, A.K. Arof, Effect of various plasticizers on the transport properties of hexanoyl chitosan-based polymer electrolyte, Journal of Applied Polymer Science, 101 (2006) 4474-4479.

[48] N.A. Choudhury, P.W.C. Northrop, A.C. Crothers, S. Jain, V.R. Subramanian, Chitosan hydrogel-based electrode binder and electrolyte membrane for EDLCs: experimental studies and model validation, Journal of Applied Electrochemistry, 42 (2012) 935-943.

[49] A.S. Khiar, R. Puteh, A.K. Arof, Characterizations of chitosan-ammonium triflate ($NH_4CF_3SO_3$) complexes by FTIR and impedance spectroscopy, Physica Status Solidi (a), 203 (2006) 534-543.

[50] S. Navaratnam, K. Ramesh, S. Ramesh, A. Sanusi, W.J. Basirun, A.K. Arof, Transport mechanism studies of chitosan electrolyte systems, Electrochimica Acta, 175 (2015) 68-73.

[51] A. Pawlicka, R.I. Mattos, C.E. Tambelli, I.D.A. Silva, C.J. Magon, J.P. Donoso, Magnetic resonance study of chitosan bio-membranes with proton conductivity properties, Journal of Membrane Science, 429 (2013) 190-196.

[52] M.Z.A. Yahya, A.K. Arof, Effect of oleic acid plasticizer on chitosan-lithium acetate solid polymer electrolytes, European Polymer Journal, 39 (2003) 897-902.

[53] Y. Wan, K.A.M. Creber, B. Peppley, V.T. Bui, Synthesis, characterization and ionic conductive properties of phosphorylated chitosan membranes, Macromolecular Chemistry and Physics, 204 (2003) 850-858.

[54] M.Z.A. Yahya, A.K. Arof, Conductivity and X-ray photoelectron studies on lithium acetate doped chitosan films, Carbohydrate Polymers, 55 (2004) 95-100.

[55] T. Winie, A.K. Arof, Dielectric behaviour and AC conductivity of $LiCF_3SO_3$ doped H-chitosan polymer films, Ionics, 10 (2004) 193-199.

[56] J.F. Du, Y. Bai, W.Y. Chu, L.J. Qiao, Synthesis and performance of proton conducting chitosan/NH_4Cl electrolyte, Journal of Polymer Science Part B: Polymer Physics, 48 (2010) 260-266.

[57] N.A. Aziz, S.R. Majid, A.K. Arof, Synthesis and characterizations of phthaloyl chitosan-based polymer electrolytes, Journal of Non-Crystalline Solids, 358 (2012) 1581-1590.

[58] S.R. Majid, A.K. Arof, Electrical behavior of proton-conducting chitosan-phosphoric acid-based electrolytes, Physica B: Condensed Matter, 390 (2007) 209-215.
[59] A.S.A. Khiar, R. Puteh, A.K. Arof, Conductivity studies of a chitosan-based polymer electrolyte, Physica B: Condensed Matter, 373 (2006) 23-27.
[60] Z. Osman, A.K. Arof, FTIR studies of chitosan acetate based polymer electrolytes, Electrochimica Acta, 48 (2003) 993-999.
[61] R.H.Y. Subban, A.K. Arof, S. Radhakrishna, Polymer batteries with chitosan electrolyte mixed with sodium perchlorate, Materials Science and Engineering: B, 38 (1996) 156-160.
[62] I.A. Fadzallah, S.R. Majid, M.A. Careem, A.K. Arof, Relaxation process in chitosan-oxalic acid solid polymer electrolytes, Ionics, 20 (2014) 969-975.
[63] N.K. Idris, N.A.N. Aziz, M.S.M. Zambri, N.A. Zakaria, M.I.N. Isa, Ionic conductivity studies of chitosan-based polymer electrolytes doped with adipic acid, Ionics, 15 (2009) 643-646.
[64] S.R. Majid, A.K. Arof, Proton-conducting polymer electrolyte films based on chitosan acetate complexed with NH_4NO_3 salt, Physica B: Condensed Matter, 355 (2005) 78-82.
[65] D.F. Vieira, C.O. Avellaneda, A. Pawlicka, Conductivity study of a gelatin-based polymer electrolyte, Electrochimica Acta, 53 (2007) 1404-1408.
[66] A. Pawlicka, M. Danczuk, W. Wieczorek, E. Zygadło-Monikowska, Influence of plasticizer type on the properties of polymer electrolytes based on chitosan, The Journal of Physical Chemistry A, 112 (2008) 8888-8895.
[67] S. Ramesh, K.C. Wong, Conductivity, dielectric behaviour and thermal stability studies of lithium ion dissociation in poly(methyl methacrylate)-based gel polymer electrolytes, Ionics, 15 (2009) 249-254.
[68] S.N.F. Yusuf, A.D. Azzahari, V. Selvanathan, R. Yahya, M.A. Careem, A.K. Arof, Improvement of N-phthaloylchitosan based gel polymer electrolyte in dye-sensitized solar cells using a binary salt system, Carbohydrate Polymers, 157 (2017) 938-944.
[69] A.M. Stephan, R. Thirunakaran, N.G. Renganathan, V. Sundaram, S. Pitchumani, N. Muniyandi, R. Gangadharan, P. Ramamoorthy, A study on polymer blend electrolyte based on PVC/PMMA with lithium salt, Journal of Power Sources, 81 (1999) 752-758.
[70] R. Arunkumar, R.S. Babu, M.U. Rani, S. Rajendran, Influence of plasticizer on ionic conductivity of PVC-PBMA polymer electrolytes, Ionics, 23 (2017) 3097-3109.

[71] A. Ahmad, K.B.M. Isa, Z. Osman, Conductivity and structural studies of plasticized polyacrylonitrile (PAN)-lithium triflate polymer electrolyte films, Sains Malaysiana, 40 (2011) 691-694.

[72] K. Mishra, S.S. Pundir, D.K. Rai, Effect of polysorbate plasticizer on the structural and ion conduction properties of PEO-NH_4PF_6 solid polymer electrolyte, Ionics, 23 (2017) 105-112.

[73] M. Mîndroiu, R.G. Zgârian, F. Kajzar, I. Rău, H.C.L. De Oliveira, A. Pawlicka, G.T. Tihan, DNA-based membranes for potential applications, Ionics, 21 (2015) 1381-1390.

[74] M.F. Shukur, R. Ithnin, M.F.Z. Kadir, Ionic conductivity and dielectric properties of potato starch-magnesium acetate biopolymer electrolytes: the effect of glycerol and 1-butyl-3-methylimidazolium chloride, Ionics, 22 (2016) 1113-1123.

[75] M. Lavorgna, F. Piscitelli, P. Mangiacapra, G.G. Buonocore, Study of the combined effect of both clay and glycerol plasticizer on the properties of chitosan films, Carbohydrate Polymers, 82 (2010) 291-298.

[76] A. Pawlicka, D.F. Vieira, R.C. Sabadini, Gelatin-HCl biomembranes with ionic-conducting properties, Ionics, 19 (2013) 1723-1731.

[77] N.N.A. Amran, N.S.A. Manan, M.F.Z. Kadir, The effect of $LiCF_3SO_3$ on the complexation with potato starch-chitosan blend polymer electrolytes, Ionics, 22 (2016) 1647-1658.

[78] M.V.L. Chandra, S. Karthikeyan, S. Selvasekarapandian, D.V. Pandi, S. Monisha, S.A. Packiaseeli, Characterization of high ionic conducting PVAc-PMMA blend-based polymer electrolyte for electrochemical applications, Ionics, 22 (2016) 2409-2420.

[79] Y.N. Sudhakar, M. Selvakumar, Lithium perchlorate doped plasticized chitosan and starch blend as biodegradable polymer electrolyte for supercapacitors, Electrochimica acta, 78 (2012) 398-405.

[80] L. Ponez, F.C. Sentanin, S.R. Majid, A.K. Arof, A. Pawlicka, Ion-conducting membranes based on gelatin and containing LiI/I_2 for electrochromic devices, Molecular Crystals and Liquid Crystals, 554 (2012) 239-251.

[81] N.K. Idris, H.B. Senin, A.K. Arof, Dielectric spectra of LiTFSI-doped chitosan/PEO blends, Ionics, 13 (2007) 213-217.

[82] W. Gorecki, M. Jeannin, E. Belorizky, C. Roux, M. Armand, Physical properties of solid polymer electrolyte PEO (LiTFSI) complexes, Journal of Physics: Condensed Matter, 7 (1995) 6823.

[83] A. Vallée, S. Besner, J. Prud'Homme, Comparative study of poly(ethylene oxide) electrolytes made with $LiN(CF_3SO_2)_2$, $LiCF_3SO_3$ and $LiClO_4$: Thermal properties and conductivity behaviour, Electrochimica acta, 37 (1992) 1579-1583.

[84] M. Hernandez, L. Servant, J. Grondin, J.C. Lassègues, Spectroscopic characterization of metal chloride/polyamide complexes, Ionics, 1 (1995) 454-468.

[85] S. Lascaud, M. Perrier, A. Vallee, S. Besner, J. Prud'Homme, M. Armand, Phase diagrams and conductivity behavior of poly(ethylene oxide)-molten salt rubbery electrolytes, Macromolecules, 27 (1994) 7469-7477.

[86] A.R. Polu, H.-W. Rhee, Ionic liquid doped PEO-based solid polymer electrolytes for lithium-ion polymer batteries, International Journal of Hydrogen Energy, 42 (2017) 7212-7219.

[87] S.S. Zhang, K. Xu, T.R. Jow, Study of $LiBF_4$ as an electrolyte salt for a Li-ion battery, Journal of The Electrochemical Society, 149 (2002) A586-A590.

[88] S.S. Zhang, K. Xu, T.R. Jow, A new approach toward improved low temperature performance of Li-ion battery, Electrochemistry Communications, 4 (2002) 928-932.

[89] S. Zhang, K. Xu, T. Jow, Low-temperature performance of Li-ion cells with a $LiBF_4$-based electrolyte, Journal of Solid State Electrochemistry, 7 (2003) 147-151.

[90] S. Rajendran, M. Sivakumar, R. Subadevi, Effect of salt concentration in poly(vinyl alcohol)-based solid polymer electrolytes, Journal of Power Sources, 124 (2003) 225-230.

[91] P. Barbosa, L. Rodrigues, M. Silva, M. Smith, A. Gonçalves, E. Fortunato, Application of di-ureasil ormolytes based on lithium tetrafluoroborate in solid-state electrochromic displays, Journal of Materials Chemistry, 20 (2010) 723-730.

[92] S.M. Zahurak, M.L. Kaplan, E.A. Rietman, D.W. Murphy, R.J. Cava, Phase relationships and conductivity of the polymer electrolytes poly(ethylene oxide)/lithium tetrafluoroborate and poly(ethylene oxide)/lithium trifluoromethanesulfonate, Macromolecules, 21 (1988) 654-660.

[93] M.M. Silva, S.C. Barros, M.J. Smith, J.R. MacCallum, Characterization of solid polymer electrolytes based on poly(trimethylenecarbonate) and lithium tetrafluoroborate, Electrochimica Acta, 49 (2004) 1887-1891.

[94] V. Aravindan, J. Gnanaraj, S. Madhavi, H.-K. Liu, Lithium-Ion Conducting Electrolyte Salts for Lithium Batteries, Chemistry-A European Journal, 17 (2011) 14326-14346.

[95] M.M. Silva, N. Gonçalves, M.J. Smith, P. Lightfoot, Ionic conduction and thermal properties of poly(ethylene oxide)-Tm(CF_3SO_3)$_3$ electrolyte films, Electrochimica Acta, 43 (1998) 1511-1515.

[96] H.B. Kagan, Introduction: frontiers in lanthanide chemistry, ACS Publications, 2002.

[97] H.B. Silber, V. Maraschin, R. Campbell, Europium (III)-triflate interactions in water and aqueous methanol studied by UV-vis and luminescence, Journal of Solid State Chemistry, 171 (2003) 225-229.

[98] J.-C.G. Bünzli, Lanthanide luminescence for biomedical analyses and imaging, Chemical Reviews, 110 (2010) 2729-2755.

[99] K. Binnemans, Lanthanide-based luminescent hybrid materials, Chemical Reviews, 109 (2009) 4283-4374.

[100] S.V. Eliseeva, J.-C.G. Bünzli, Lanthanide luminescence for functional materials and bio-sciences, Chemical Society Reviews, 39 (2010) 189-227.

[101] J.-C.G. Bünzli, S. Comby, A.-S. Chauvin, C.D.B. Vandevyver, New opportunities for lanthanide luminescence, Journal of Rare Earths, 25 (2007) 257-274.

[102] J.-C.G. Bünzli, C. Piguet, Taking advantage of luminescent lanthanide ions, Chemical Society Reviews, 34 (2005) 1048-1077.

[103] L.D. Carlos, Decay times of Eu (III) and Nd (III) in polymer electrolytes, Solid State Ionics, 85 (1996) 181-185.

[104] M. Morita, M. Ishikawa, Y. Matsuda, Ionic conductivities of polymeric solid electrolyte films containing rare earth ions, Journal of Alloys and Compounds, 250 (1997) 524-527.

[105] T.A. Hamdalla, T.A. Hanafy, A.E. Bekheet, Influence of erbium ions on the optical and structural properties of polyvinyl alcohol, Journal of Spectroscopy, 2015 (2015) (7pp).

[106] D.G. Karraker, Coordination of trivalent lanthanide ions, Journal of Chemical Education, 47 (1970) 424.

[107] T.A. Hanafy, Dielectric relaxation and alternating-current conductivity of gadolinium-doped poly(vinyl alcohol), Journal of Applied Polymer Science, 108 (2008) 2540-2549.

[108] M. Morita, F. Araki, K. Kashiwamura, N. Yoshimoto, M. Ishikawa, Ionic structure and conductance behavior of plasticized polymeric electrolytes containing multivalent cations, Electrochimica Acta, 45 (2000) 1335-1340.

[109] F.K.M. Genova, S. Selvasekarapandian, N. Vijaya, S. Sivadevi, M. Premalatha, S. Karthikeyan, Lithium ion-conducting polymer electrolytes based on PVA-PAN doped with lithium triflate, Ionics, 23 (2017) 2727-2734.

[110] M. Fernandes, V.T. Freitas, S. Pereira, E. Fortunato, R.A.S. Ferreira, L.D. Carlos, R. Rego, V. de Zea Bermudez, Green Li^{+}-and Er^{3+}-doped poly (ε-caprolactone)/siloxane biohybrid electrolytes for smart electrochromic windows, Solar Energy Materials and Solar Cells, 123 (2014) 203-210.

[111] S. Rajendran, O. Mahendran, T. Mahalingam, Thermal and ionic conductivity studies of plasticized PMMA/PVdF blend polymer electrolytes, European Polymer Journal, 38 (2002) 49-55.

[112] R. Ramya, P.N. Sudha, J. Mahalakshmi, Preparation and characterization of chitosan binary blend, International Journal of Scientific and Research Publications, 2 (2012) 1-9.

[113] S.Z. Rogovina, G.A. Vikhoreva, Polysaccharide-based polymer blends: Methods of their production, Glycoconjugate Journal, 23 (2006) 611-618.

[114] O.Gh. Abdullah, R.R. Hanna, Y.A.K. Salman, Structural, optical, and electrical characterization of chitosan: methylcellulose polymer blends based film, Journal of Materials Science: Materials in Electronics, 28 (2017) 10283-10294.

[115] K.M.G. Francis, S. Subramanian, K. Shunmugavel, V. Naranappa, S.S.M. Pandian, S.C. Nadar, Lithium ion-conducting blend polymer electrolyte based on PVA-PAN doped with lithium nitrate, Polymer-Plastics Technology and Engineering, 55 (2016) 25-35.

[116] I. Nicotera, L. Coppola, C. Oliviero, M. Castriota, E. Cazzanelli, Investigation of ionic conduction and mechanical properties of PMMA-PVdF blend-based polymer electrolytes, Solid State Ionics, 177 (2006) 581-588.

[117] G.M. Wu, S.J. Lin, C.C. Yang, Preparation and characterization of PVA/PAA membranes for solid polymer electrolytes, Journal of Membrane Science, 275 (2006) 127-133.

[118] A. Sionkowska, Current research on the blends of natural and synthetic polymers as new biomaterials, Progress in Polymer Science, 36 (2011) 1254-1276.

[119] S. Mathew, M. Brahmakumar, T.E. Abraham, Microstructural imaging and characterization of the mechanical, chemical, thermal, and swelling properties of starch-chitosan blend films, Biopolymers, 82 (2006) 176-187.

[120] E.A. El-Hefian, M.M. Nasef, A.H. Yahaya, Chitosan-Based Polymer Blends: Current Status and Applications, Journal of the Chemical Society of Pakistan, 36 (2014) 11-27.

[121] A. Pawlak, M. Mucha, Thermogravimetric and FTIR studies of chitosan blends, Thermochimica Acta, 396 (2003) 153-166.

[122] Y.X. Xu, K.M. Kim, M.A. Hanna, D. Nag, Chitosan-starch composite film: preparation and characterization, Industrial Crops and Products, 21 (2005) 185-192.

[123] J. Li, S. Zivanovic, P.M. Davidson, K. Kit, Characterization and comparison of chitosan/PVP and chitosan/PEO blend films, Carbohydrate Polymers, 79 (2010) 786-791.

[124] S. Zivanovic, J. Li, P.M. Davidson, K. Kit, Physical, mechanical, and antibacterial properties of chitosan/PEO blend films, Biomacromolecules, 8 (2007) 1505-1510.

[125] V.L. Alexeev, E.A. Kelberg, G.A. Evmenenko, S.V. Bronnikov, Improvement of the mechanical properties of chitosan films by the addition of poly(ethylene oxide), Polymer Engineering & Science, 40 (2000) 1211-1215.

[126] N. Rakkapao, V. Vao-soongnern, Y. Masubuchi, H. Watanabe, Miscibility of chitosan/poly(ethylene oxide) blends and effect of doping alkali and alkali earth metal ions on chitosan/PEO interaction, Polymer, 52 (2011) 2618-2627.

[127] E. Yilmaz, N. Erdenizci, O. Yilmaz, Miscibility of chitosan and poly(ethylene oxide) in dilute solution, International Journal of Polymer Analysis and Characterization, 8 (2003) 327-338.

[128] N. Rakkapao, H. Watanabe, Y. Matsumiya, Y. Masubuchi, Dielectric Relaxation and Ionic Conductivity of a Chitosan/Poly(ethylene oxide) Blend Doped with Potassium and Calcium Cations, Nihon Reoroji Gakkaishi, 44 (2016) 89-97.

[129] M.F. Shukur, R. Ithnin, H.A. Illias, M.F.Z. Kadir, Proton conducting polymer electrolyte based on plasticized chitosan-PEO blend and application in electrochemical devices, Optical Materials, 35 (2013) 1834-1841.

[130] M.H. Buraidah, L.P. Teo, C.M. Au Yong, S. Shah, A.K. Arof, Performance of polymer electrolyte based on chitosan blended with poly(ethylene oxide) for plasmonic dye-sensitized solar cell, Optical Materials, 57 (2016) 202-211.

[131] L.M.N. Assis, L. Ponez, A. Januszko, K. Grudzinski, A. Pawlicka, A green-yellow reflective electrochromic device, Electrochimica Acta, 111 (2013) 299-304.

[132] C.O. Avellaneda, D.F. Vieira, A. Al-Kahlout, S. Heusing, E.R. Leite, A. Pawlicka, M.A. Aegerter, All solid-state electrochromic devices with gelatin-based electrolyte, Solar Energy Materials and Solar Cells, 92 (2008) 228-233.

[133] C.O. Avellaneda, D.F. Vieira, A. Al-Kahlout, E.R. Leite, A. Pawlicka, M.A. Aegerter, Solid-state electrochromic devices with Nb_2O_5: Mo thin film and gelatin-based electrolyte, Electrochimica Acta, 53 (2007) 1648-1654.

[134] G. Cai, J. Wang, P.S. Lee, Next-generation multifunctional electrochromic devices, Accounts of Chemical Research, 49 (2016) 1469-1476.

[135] A. Pawlicka, C.O. Avellaneda, Thin film sol-gel of CeO_2-ZrO_2: the candidate for counter electrode in electrochromic devices, Molecular Crystals and Liquid Crystals, 354 (2000) 463-473.

[136] C. Avellaneda, A. Pawlicka, Lithium Intercalation in CeO_2-TiO_2 Thin Film, Molecular Crystals and Liquid Crystals, 415 (2004) 221-227.

[137] C.O. Avellaneda, A. Pawlicka, Preparation of transparent CeO_2-TiO_2 coatings for electrochromic devices, Thin Solid Films, 335 (1998) 245-248.

[138] P.C. Barbosa, L.C. Rodrigues, M.M. Silva, M.J. Smith, A. Parola, F. Pina, C. Pinheiro, Solid-state electrochromic devices using pTMC/PEO blends as polymer electrolytes, Electrochimica Acta, 55 (2010) 1495-1502.

[139] A. Pawlicka, D. Dragunski, K. Guimarães, C. Avellaneda, Electrochromic devices with solid electrolytes based on natural polymers, Molecular Crystals and Liquid Crystals, 416 (2004) 105-112.

[140] L.M.N. Assis, R. Leones, J. Kanicki, A. Pawlicka, M.M. Silva, Prussian blue for electrochromic devices, Journal of Electroanalytical Chemistry, 777 (2016) 33-39.

[141] R.D. Alves, L.C. Rodrigues, J.R. Andrade, M. Fernandes, J.V. Pinto, L. Pereira, A. Pawlicka, R. Martins, E. Fortunato, V. de Zea Bermudez, $Gelatin_nZn(CF_3SO_3)_2$ polymer electrolytes for electrochromic devices, Electroanalysis, 25 (2013) 1483-1490.

[142] R.D. Alves, L.C. Rodrigues, J.R. Andrade, A. Pawlicka, L. Pereira, R. Martins, E. Fortunato, M.M. Silva, Study and characterization of a novel polymer electrolyte based on agar doped with magnesium triflate, Molecular Crystals and Liquid Crystals, 570 (2013) 1-11.

[143] R. Alves, F. Sentanin, R.C. Sabadini, A. Pawlicka, M.M. Silva, Innovative electrolytes based on chitosan and thulium for solid state applications: synthesis, structural, and thermal characterization, Journal of Electroanalytical Chemistry, 788 (2017) 156-164.

[144] J. Jensen, M. Hösel, A.L. Dyer, F.C. Krebs, Development and Manufacture of Polymer-Based Electrochromic Devices, Advanced Functional Materials, 25 (2015) 2073-2090.

[145] C.O. Avellaneda, L.O.S. Bulhões, A. Pawlicka, The CeO_2-TiO_2-ZrO_2 sol-gel film: a counter-electrode for electrochromic devices, Thin Solid Films, 471 (2005) 100-104.

[146] L.M.N. Assis, J.R. Andrade, L.H.E. Santos, A.J. Motheo, B. Hajduk, M. Łapkowski, A. Pawlicka, Spectroscopic and microscopic study of Prussian blue film for electrochromic device application, Electrochimica Acta, 175 (2015) 176-183.

[147] M.-S. Fan, S.-Y. Kao, T.-H. Chang, R. Vittal, K.-C. Ho, A high contrast solid-state electrochromic device based on nano-structural Prussian blue and poly(butyl viologen) thin films, Solar Energy Materials and Solar Cells, 145 (2016) 35-41.

[148] R.G. Zgârian, G.T. Tihan, F. Kajzar, I. Rău, A. Pawlicka, M.V. Mîndroiu, Chromophore doped DNA based solid polymer electrolyte for electrochromic devices, Arabian Journal of Chemistry, 10 (2017) 232-239.

[149] Q. Li, J. Chen, L. Fan, X. Kong, Y. Lu, Progress in electrolytes for rechargeable Li-based batteries and beyond, Green Energy & Environment, 1 (2016) 18-42.

[150] B. Liang, Q. Jiang, S. Tang, S. Li, X. Chen, Porous polymer electrolytes with high ionic conductivity and good mechanical property for rechargeable batteries, Journal of Power Sources, 307 (2016) 320-328.

[151] W.H. Meyer, Polymer electrolytes for lithium-ion batteries, Advanced materials, 10 (1998) 439-448.

[152] Y. Ma, L.B. Li, G.X. Gao, X.Y. Yang, Y. You, Effect of montmorillonite on the ionic conductivity and electrochemical properties of a composite solid polymer electrolyte based on polyvinylidenedifluoride/polyvinyl alcohol matrix for lithium ion batteries, Electrochimica Acta, 187 (2016) 535-542.

[153] C.M. Costa, R. Leones, M.M. Silva, S. Lanceros-Mendez, Influence of different salts in poly(vinylidene fluoride-co-trifluoroethylene) electrolyte separator membranes for battery applications, Journal of Electroanalytical Chemistry, 727 (2014) 125-134.

[154] D. Roy, J.N. Cambre, B.S. Sumerlin, Future perspectives and recent advances in stimuli-responsive materials, Progress in Polymer Science, 35 (2010) 278-301.

[155] F. Opekar, K. Štulík, Electrochemical sensors with solid polymer electrolytes, Analytica Chimica Acta, 385 (1999) 151-162.

[156] Y. Wang, K.S. Chen, J. Mishler, S.C. Cho, X.C. Adroher, A review of polymer electrolyte membrane fuel cells: technology, applications, and needs on fundamental research, Applied Energy, 88 (2011) 981-1007.

[157] B. Smitha, S. Sridhar, A.A. Khan, Solid polymer electrolyte membranes for fuel cell applications-a review, Journal of Membrane Science, 259 (2005) 10-26.

[158] Y.-S. Ye, J. Rick, B.-J. Hwang, Water soluble polymers as proton exchange membranes for fuel cells, Polymers, 4 (2012) 913-963.
[159] Y. Wang, Recent research progress on polymer electrolytes for dye-sensitized solar cells, Solar Energy Materials and Solar Cells, 93 (2009) 1167-1175.
[160] M. Grätzel, Perspectives for dye-sensitized nanocrystalline solar cells, Progress in Photovoltaics: Research and Applications, 8 (2000) 171-185.
[161] P.K. Singh, B. Bhattacharya, R.K. Nagarale, S.P. Pandey, K.-W. Kim, H.-W. Rhee, Ionic liquid doped poly(N-methyl 4-vinylpyridine iodide) solid polymer electrolyte for dye-sensitized solar cell, Synthetic Metals, 160 (2010) 950-954.
[162] Y. Li, Y. Cao, J. Gao, D. Wang, G. Yu, A.J. Heeger, Electrochemical properties of luminescent polymers and polymer light-emitting electrochemical cells, Synthetic Metals, 99 (1999) 243-248.
[163] R.D. Costa, E. Ortí, H.J. Bolink, F. Monti, G. Accorsi, N. Armaroli, Luminescent Ionic Transition-Metal Complexes for Light-Emitting Electrochemical Cells, Angewandte Chemie International Edition, 51 (2012) 8178-8211.
[164] S.B. Meier, D. Tordera, A. Pertegas, C. Roldan-Carmona, E. Ortí, H.J. Bolink, Light-emitting electrochemical cells: recent progress and future prospects, Materials Today, 17 (2014) 217-223.

Chapter 2

Experimental section

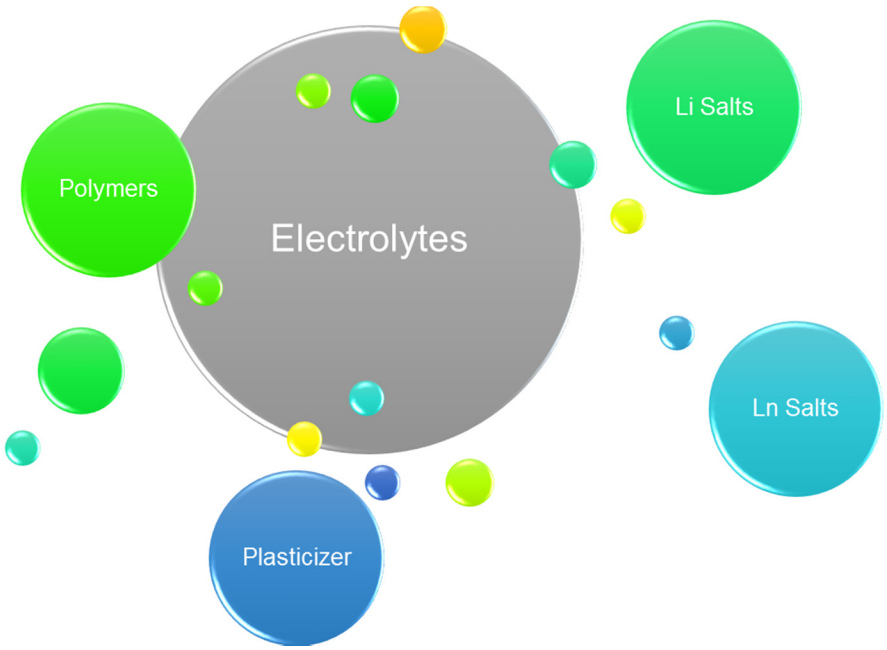

2.1. Objective

The main objective of this chapter is describe the general preparation of the samples, and the techniques used to characterize the electrolytes. In the next chapters, the preparation scheme of each particular system is presented, as well as, the constitution and designation of the samples.

2.2. Experimental section

2.2.1 Materials

The main characteristic of the commercial materials are presented in Table 2.1.

Thulium (III) trifluoromethanesulfonate (thulium triflate (TmTrif, $Tm(CF_3SO_3)_3$)) was prepared by addition of trifluoromethanesulfonic acid (Merck, 98%) to an excess of thulium oxide (Aldrich, 99.9%), and this aqueous suspension was stirred until pH approached neutrality as described by Silva et al. [1].

Acetic acid (Sigma-Aldrich) and Milli-Q water were used in all experiments to prepare 1% acetic acid solution.

2.2.2 Electrolytes preparation

The SPEs were synthesized via solvent casting technique and according to the method reported elsewhere [2]. Samples were prepared by dispersion of 0.20 g of CH in 10 mL of 1% acetic acid solution, under magnetic stirring overnight for complete dissolution. In the next day, salts were added to these solutions, they were left under stirring during few minutes, and then glycerol, as plasticizer, was added, and the solutions continued under magnetic stirring for a more few minutes. The resulting solutions were then poured on Petri plates, and left at room temperature until a film formation. Then, the obtained electrolytes were subjected to a final drying procedure in which the temperature was raised from 30°C to 60°C, over a period of two days, and during this period the oven was periodically evacuated and purged with dry argon. After the drying process, the samples were conditioned in a glovebox under argon atmosphere. Figure 2.1 has a preparation scheme and a physical appearance picture of one of these samples. The thickness of the

electrolytes were determined with a micrometer Mitutoyo, and the results are presented in each of the next six chapters.

Table 2.1 Characteristics of the commercial materials.

Name	Abbreviation	Characteristics
Chitosan	CH	Sigma-Aldrich, Medium Mw, deacetylation degree 75%
Poly(ethylene oxide)	PEO	Sigma-Aldrich, Mw = $5x10^6$
Glycerol	Gly	Himedia, 99.5%
Europium (III) trifluoromethanesulfonate (Europium triflate)	EuTrif, $Eu(CF_3SO_3)_3$	Sigma-Aldrich, 98%
Dysprosium (III) trifluoromethanesulfonate (Dysprosium triflate)	DyTrif, $Dy(CF_3SO_3)_3$	Sigma-Aldrich, 98%
Erbium (III) trifluoromethanesulfonate (Erbium triflate)	ErTrif, $Er(CF_3SO_3)_3$	Sigma-Aldrich, 98%
Samarium (III) trifluoromethanesulfonate (Samarium triflate)	SmTrif, $Sm(CF_3SO_3)_3$	Sigma-Aldrich, 98%
Lithium (I) trifluoromethanesulfonate (Lithium triflate)	LiTrif, $LiCF_3SO_3$	Sigma-Aldrich, 99.995%
Cerium (III) trifluoromethanesulfonate (Cerium triflate)	CeTrif, $Ce(CF_3SO_3)_3$	HuiChem, 98%

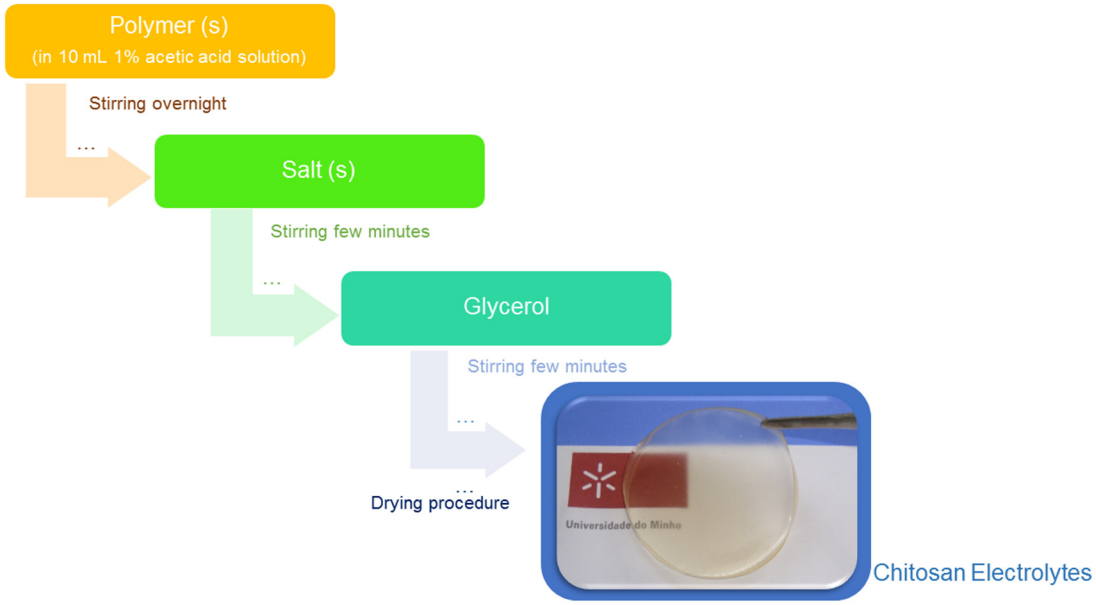

Figure 2.1 Preparation scheme and a physical appearance picture of one of these samples.

2.2.3 Characterization techniques

The Thermogravimetric Analysis (TGA) is a technique where the variations in mass are measured as a function of temperature or time while the sample is subjected to a controlled temperature program in a controlled atmosphere [3]. So, electrolyte sample sections were subjected to thermal analysis in order to verify variations that involve weight loss as a function of temperature. To perform these analyses, an equipment that consist of a combination of a high sensitivity microbalance and an oven with a temperature program and a controlled atmosphere is required. The samples are placed in a platinum can that is suspended by a filament connected to the balance. The obtained results appear as thermogravimetric curves where the weight (%) or the derivative weight (%/ºC) are represented as a function of the temperature. The curves are characteristic of each sample and allow studying processes that lead to the thermal degradation of the material. The TGA and differential thermogravimetric analysis (DTGA) were made using a TGA instrument Shimadzu TGA-Q500 in 30 - 900ºC temperature range, at a heating rate of 10ºC min^{-1}, and under a nitrogen atmosphere with a 60 mL min^{-1} rate flow. Before each analysis and aiming to eliminate the traces of absorbed moisture all samples were subject to a first run from 30 to 105ºC, at a heating rate of 20ºC min^{-1}, followed by a second isothermal run at 105ºC during 10 minutes.

The Differential Scanning Calorimetry (DSC) is the most popular thermal analysis technique [3]. It is a high sensitivity technique that allows measuring numerous properties, such as, glass transition temperature (T_g) and melting point (T_m) of the samples, for example. According to this technique, the sample is subjected to a controlled temperature program, and the heat flow rate difference into a substance and a reference is measured as a function of temperature or time [3]. In a typical DSC thermograms, the flow of heat energy (expressed as the change in enthalpy with time in units of Wg^{-1}, for example) is recorded as a function of temperature or time. For the DSC measurements, the electrolytes were analysed under a flowing argon atmosphere using a Mettler DSC 821e, in a temperature range between -60 to 200ºC and at a heating rate of 5ºC min^{-1}. The samples were placed in 40 μL aluminium cans, which are made up of two parts, a base where the sample is placed, and a top part serving as a cover, with perforated lids to permit the release and removal of decomposition products. All measurements were carried out under a 30 $mLmin^{-1}$ flowing argon atmosphere.

The impedance spectroscopy technique is used to determine the conductivity of an electrolyte and it can be used under continuous current (little used) or alternating current. The use of the alternating current is more advantageous because with a simple cell with two electrodes and an electrolyte, it is possible to study the properties of the electrolyte due to the information about the migration of ions and the polarization phenomena occurring inside the cell [4]. The impedance measurements were used to determine the conductivity of the electrolytes, and one method used to present these measures is the Nyquist diagrams. According to these diagrams, the impedance can be expressed as a complex number, where the resistance is the real component (Z') and the capacitance is the imaginary component ($-Z''$). These analyses were carried out using a frequency response analyser, Autolab PGSTAT-12 between 65 kHz and 500 mHz. The total ionic conductivity of electrolytes was determined using a constant volume support located within a Buchi TO 51 oven. First, the thicknesses of each gold electrodes (Goodfellow, >99.95%) were measured using a digital micrometer Mytutoyo (± 0.001 mm). Then an electrolyte disk was introduced between two 10 mm diameter ion-blocking gold electrodes forming the electrode/CH electrolyte/electrode assembly. The measurements were done during heating cycles, and the samples temperature was evaluated using a K-type thermocouple localized close to electrolyte disk. Before each analysis, the samples were subjected to a heating pre-treatment for two hours at 60ºC to optimize the

electrode/electrolyte contact. All analyses were performed in the day after the preparation, and the measurements were carried out at a temperature range from room temperature to approximately 100°C, and at approximately 7°C temperature intervals. The equivalent circuit was used for analyzing the reaction mechanisms and kinetic parameters present in the SPEs [5], in the present case, a modified Randles circuit [6] (Figure 2.2), that represents the electrolyte between the working and reference electrodes, in parallel with a capacitance, which is an interface between solid polymer membrane, with different salts and electrode, and it describes the behavior of non-ideal capacitors.

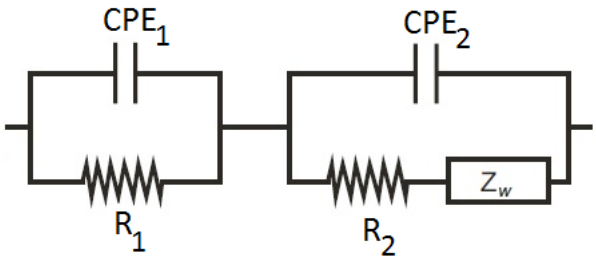

Figure 2.2 Schematic representation of the equivalent circuit model used to fit impedance data of the SPEs.

The charge-transfer resistance (R_2), in parallel with Warburg impedance (Z_w), reflects the influence of the mass transport of electroactive species on the total impedance of the electrochemical cell. The double-layer capacitance (CPE_2) represents the capacitance of the film [7].

X-Ray diffraction (XRD) is a useful technique used to investigate a wide variety of information of the fine scale structure of the material [8]. This is a very useful technique for qualitative and quantitative analyses as well as for fundamental studies of the properties and structures of polymers, such as crystallinity, crystallite size, orientation, phase changes and melting points [9]. In a typical XRD graph, the intensity appear as a function of the diffraction angle, being this intensity the sum of the relative intensities of all the diffracted rays in the same direction versus the Bragg angle. The obtained diffractograms are characteristic of each sample and allow checking on, for example, the crystalline or amorphous nature of the materials. The XRD measurements were made using a Siemens D-5000 instrument with CuK_α radiation (λ = 1.5418Å), at room temperature, and in the angular range (2θ) from 3 to 60º.

The Scanning Electron Microscopy (SEM) is a useful technique used in the characterization of the material's surface. According to the SEM technique, a high-energy electron beam scans across the surface of the material, usually coated with a thin film of gold, used to improve contrast and the signal-to-noise ratio. As the beam scans across the surface, the interactions between the sample and the electron beam result in different types of electron signals emitted at or near the sample's surface, whose signals are collected, processed, and translated to form an image of the sample's surface topography [10]. The SEM micrographs were obtained in a LEO 440 instrument at different magnifications and all samples were coated with a conductive layer of sputtered gold.

Energy Dispersive Spectroscopy (EDS) is an analytical technique very used for the elemental analysis or chemical characterization of the samples. It is used as an attachment to the SEM and the spectra obtained is easily interpreted [11]. The EDS analyses was performed with an EDX Link Analytical with a resolution of 133 eV, and the samples' area analyzed by EDS was the same as of SEM taken pictures.

The Atomic Force Microscopy (AFM) is an amazing technique that allows see and measure surface structure but rather different when compared to other based on typical microscopes. In the other microscopes an image is formed by focusing light or electrons onto a surface while in the AFM technique the microscope physically "feels" the sample and its surface with a sharp probe, resulting in a map of the height sample's surface [12]. The AFM analyses are very used in order to evaluate the homogeneity and changes in the surface topography of developed electrolytes. The AFM images were produced using a Nanosurf easyScan 2 AFM System. There are two principal modes of AFM: contact and tapping mode. The tapping mode was employed by using silicon AFM probes, a force constant of 48 N/m, and a resonance frequency of 190 kHz. The scanning area depending on the sample and the roughness values appear as the roughness mean square (RMS).

The Electron Paramagnetic Resonance (EPR) spectroscopy is related with the detection of unpaired electrons and with characterizing their chemical environments, and so it is a sensitive technique for the study of local coordination environment of paramagnetic centers [13]. Normally, the EPR spectroscopy involves measurement of the magnetic fields at which paramagnetic molecules come into resonance with applied monochromatic microwave radiation. Much rarer, the excitation of electrons is achieved with a pulse of microwave energy in the presence of a constant magnetic field [13]. X-band continuous wave (CW-EPR) and pulsed EPR experiments were carried out on a Bruker Elexsys E580

spectrometer operating at 9.478 GHz. CW-EPR measurements were performed at 50 K and the pulsed experiments at 6 K. Electron spin echo envelope modulation (ESEEM) decay was recorded 4500 G using a three-pulse sequence, $(\pi/2) - \tau - (\pi/2) - T - (\pi/2) -$ (echo), with $(\pi/2)$ pulse with of 12 ns. The ESEEM spectrum was obtained from the Fourier transform of the spin echo decay. The echo-detected field-sweep absorption spectra, EDFS, were recorded using a three-pulse sequence with a $(\pi/2)$ pulse width of 12 ns. The integrated echo intensities were measured as a function of the magnetic field strength over the range of 100 – 12100 G. Hyperfine sublevel correlation experiments (HYSCORE) was performed at 4500 G using the pulse sequence $(\pi/2) - \tau - (\pi/2) - t_1 - (\pi) - t_2 - (\pi/2) - \tau -$ (echo), with $(\pi/2)$ pulse width of 12 ns and τ = 120 ns. Both time intervals t_1 and t_2 were incremented in 20 ns to generate a 128 x 128 matrix which, after apodization, was Fourier-transformed to generate the two dimensional HYSCORE spectrum. Numerical simulation was performed using the function *saffron* from the EasySpin package [14].

The study of the photophysical properties of the samples is important in order to evaluate their luminescent behavior. Room temperature emission and excitation spectra of the polymer films, as well as excited state lifetime decays were measured in a Horiba Jobin Yvon spectrofluorimeter model Fluorolog FL3-221 using continuous wave or pulsed (flash) xenon lamps. Quantum yield measurements of samples were carried out in the integrating sphere model Quanta Phi F3029, from Horiba Jobin Yvon, properly connected to the spectrofluorimeter visible detector by optical fibers. By carefully testing various samples, with different sizes, but from the same batch, quantum yields showed a maximum absolute deviation of 10%, so that the presented values are an average.

The ECDs prepared has five-layer structure, composed by a glass substrate, a transparent conductor, an ion storage coating, an ionic conductor, and an electrochromic coating. ECDs were assembled by placing electrolyte membranes in between glass/ITO/PB or WO_3 and CeO_2-TiO_2/ITO/glass substrates, and pressing these assemblies with clamps for few days (ECDs). Prussian blue was deposited electrochemically on glass/ITO (indium-tin oxide; Delta Technologies; CG-50IN- 1507; 8–12 ohms) as described by Assis *et al* [15]. Glass/ITO/WO_3 and glass/ITO/CeO_2-TiO_2 substrates were synthesized by sol-gel methods and deposited by dip-coating technique as described by Al-Kahlout [16] and Avellaneda *et al* [17], respectively. These thin films were deposited in such a way that a 1 cm of free space was left for the electrical contact on which a 1 cm wide Cu-conducting

tape (3M) was glued to improve this electrical connection. The mounted cells were finally sealed with a protective tape (3M). The ECDs were characterized by cyclic voltammetry using Autolab 302N in a proper applied voltage and at different scan rates. Chronoamperometry was performed by applying square wave of the same potentials and time intervals of 15 s/15 s. One technique commonly used for the optical characterization of ECDs is UV-Vis spectroscopy. This technique allows the determination of optical properties, such as absorbance, and transmittance, as a function of the incident light wavelength. UV-Vis spectroscopy measurements were done with Agilent 8453 and Jasco V670 from 200 to 1100 nm.

2.3. References

[1] M.M. Silva, N. Gonçalves, M.J. Smith, P. Lightfoot, Ionic conduction and thermal properties of poly(ethylene oxide)-Tm(CF_3SO_3)$_3$ electrolyte films, Electrochimica Acta, 43 (1998) 1511-1515.

[2] R. Alves, J.P. Donoso, C.J. Magon, I.D.A. Silva, A. Pawlicka, M.M. Silva, Solid polymer electrolytes based on chitosan and europium triflate, Journal of Non-Crystalline Solids, 432 (2016) 307-312.

[3] J.D. Menczel, R.B. Prime, Thermal analysis of polymers: fundamentals and applications, John Wiley & Sons, 2014.

[4] J.R. MacCallum, C.A. Vincent, Polymer electrolyte reviews, Springer Science & Business Media, 1989.

[5] D.A. Harrington, P. Van Den Driessche, Mechanism and equivalent circuits in electrochemical impedance spectroscopy, Electrochimica Acta, 56 (2011) 8005-8013.

[6] J. Hernández-Ferrer, A. Ansón-Casaos, M.T. Martínez, Electrochemical synthesis and characterization of single-walled carbon nanotubes/polypyrrole films on transparent substrates, Electrochimica Acta, 64 (2012) 1-9.

[7] R. Alves, F. Sentanin, R.C. Sabadini, M. Fernandes, V. de Zea Bermudez, A. Pawlicka, M.M. Silva, Samarium (III) Triflate-doped Chitosan Electrolyte for Solid State Electrochromic Devices, Electrochimica Acta, (2017) *in press*.

[8] B.E. Warren, X-Ray Diffraction Methods, Journal of Applied Physics, 12 (1941) 375-384.

[9] A.L. Ryland, X-ray diffraction, Journal of Chemical Education, 35 (1958) 80-83.

[10] M. Carter, J. Shieh, Chapter 5 - Microscopy, in: M. Carter, J. Shieh (Eds.) Guide to Research Techniques in Neuroscience (Second Edition), Academic Press, San Diego, 2015, pp. 117-144.

[11] P.D. Ngo, Energy Dispersive Spectroscopy, in: L.C. Wagner (Ed.) Failure Analysis of Integrated Circuits: Tools and Techniques, Springer US, Boston, MA, 1999, pp. 205-215.

[12] P. Eaton, P. West, Atomic force microscopy, Oxford University Press, 2010.

[13] B.A. Goodman, P.L. Hall, Electron paramagnetic resonance spectroscopy, in: M.J. Wilson (Ed.) Clay Mineralogy: Spectroscopic and Chemical Determinative Methods, Springer Netherlands, Dordrecht, 1994, pp. 173-225.

[14] S. Stoll, R.D. Britt, General and efficient simulation of pulse EPR spectra, Physical Chemistry Chemical Physics, 11 (2009) 6614-6625.

[15] L. M. N. Assis, R. C. Sabadini, L. P. Santos, J. Kanicki, M. Łapkowski, A. Pawlicka, Electrochromic device with Prussian blue and HPC-based electrolyte, Electrochimica Acta, 182 (2015) 878-883.

[16] A. Al-Kahlout, D. Vieira, C.O. Avellaneda, E.R. Leite, M.A. Aegerter, A. Pawlicka, Gelatin-based protonic electrolyte for electrochromic windows, Ionics, 16 (2010) 13-19.

[17] C. O. Avellaneda, A. Pawlicka, Preparation of transparent CeO_2–TiO_2 coatings for electrochromic devices, Thin Solid Films, 335 (1998) 245-248.

Chapter 3

The influence of different lanthanide salts in chitosan matrix

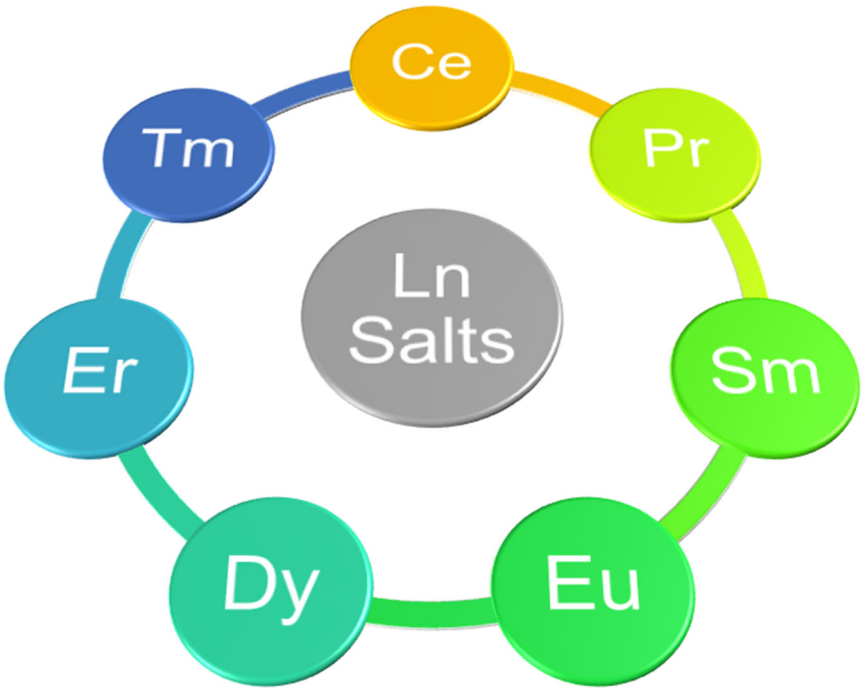

This chapter was adapted from: R. Alves, J. P. Donoso, C. J. Magon, I. D. A. Silva, A. Pawlicka, M. M. Silva, "Solid polymer electrolytes based on chitosan and europium triflate", Journal of Non-Crystalline Solids, 432 (2016) 307-312. doi:10.1016/j.jnoncrysol.2015.10.024. R. Alves, A. S. S. de Camargo, A. Pawlicka, M. M. Silva, "Luminescent polymer electrolytes based on chitosan and containing europium triflate", Journal of Rare Earths 34 (2016) 661-666. DOI: 10.1016/S1002-0721(16)60076-5. R. Alves, F. Sentanin, R. C. Sabadini, A. Pawlicka, M. M. Silva, Influence of cerium triflate and glycerol on electrochemical performance of chitosan electrolytes for electrochromic devices, Electrochimica Acta 217 (2016) 108-116. R. Alves, F. Sentanin, R. C. Sabadini, A. Pawlicka, M. M. Silva, Innovative electrolytes based on chitosan and thulium for solid state applications: Synthesis, structural, and thermal characterization, Journal of Electroanalytical Chemistry 788 (2017) 156-164. R. Alves, F. Sentanin, R. C. Sabadini, A. Pawlicka, M. M. Silva, Solid polymer electrolytes based on chitosan and $Dy(CF_3SO_3)_3$ for electrochromic devices, Solid State Ionics 310 (2017) 112-120. R. Alves, F. Sentanin, R. C. Sabadini, A. Pawlicka, M. M. Silva, Green Polymer Electrolytes of Chitosan Doped with Erbium Triflate, Journal of Non-Crystalline Solids 482 (2018) 183-191. R. Alves, F. Sentanin, R. C. Sabadini, M. Fernandes, V. de Zea Bermudez, A. Pawlicka, M. M. Silva, Samarium (III) Triflate-doped Chitosan Electrolyte for Solid State Electrochromic Devices, Electrochimica Acta (2017) *in press*.

3.1. Objective

The main objective of this chapter is verify the effect different lanthanide salts in CH matrix. The thermal analysis were used to determine the effect of the salts in terms of the thermal stability of the doped samples. The impedance measurements were made in order to evaluate the influence of the lanthanide ions in the conductivity values. Finally, the XRD, SEM, and AFM analysis served to verify which changes in morphology and structure upon salts addition. Another objective is always find the best composition for the different kind of applications.

3.2. Experimental section

Samples were prepared according to the procedure described previously [1-6], and accordingly to the present in chapter 2, and in Figure 3.1 is presented the electrolytes preparation scheme, and their physical appearance. The samples were represented by the notation CHLnTrif$_n$, where Ln = Ce, Pr, Sm, Eu, Dy, Er or Tm, and n is the mass of salt used. The thickness of the samples varied between 0.063 and 0.190 ± 0.001 mm.

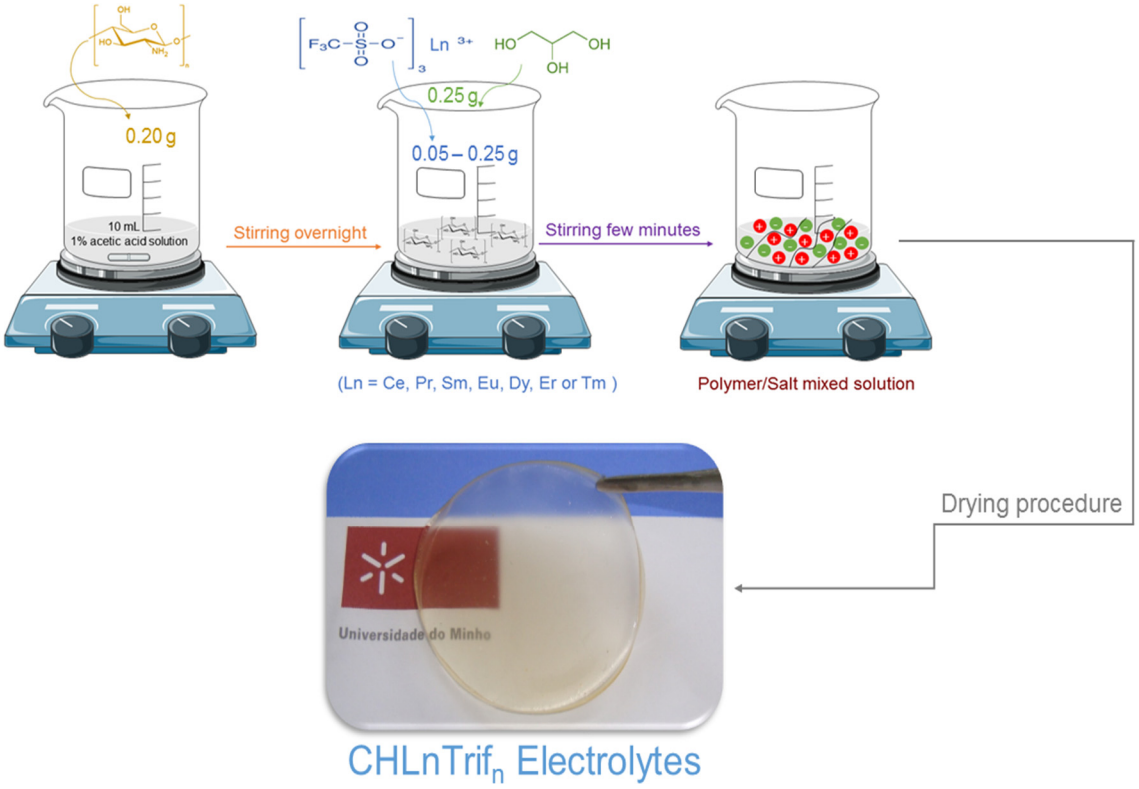

Figure 3.1 Preparation scheme and physical appearance of the samples.

The thermal behavior was evaluated by thermal analysis (TGA and DSC). The total ionic conductivities were determined by impedance spectroscopy. The morphology and structure were evaluated by XRD, SEM, and AFM.

3.3. Results and discussion

3.3.1. Thermal behavior

The thermal stability of the electrolytes based on CH and containing different lanthanide triflates was evaluated by thermogravimetric analysis (TGA and DTGA). The TGA/DTGA technique is an important feature that can been used to study all thermal processes that involve weight loss.

The thermograms present in Figure 3.2 (a) show the relation between weight percentage and temperature for the doped samples. All electrolytes showed a multi-step decomposition behavior, probably due to the different interactions of the salts and the plasticizer with the polysaccharide chain. The onset temperature (T_{onset}) was used to identify the initiation of samples weight loss and it was estimated using extrapolation of the baseline and tangent of the curve of thermal events. In the case of the CH matrix, not shown here, the degradation temperature is about 130ºC and the degradation process occurred in two stages [3]. For the doped samples there are three stages for the degradation process, instead of the two observed in the matrix, as can be observed from Figure 3.2 (a). The 1st degradation starts at between 130 - 180ºC and practically all samples presented higher T_{onset} than the matrix. So, this means that the addition of the salt contributed to an increase in the thermal stability of the electrolytes. In agar-based electrolyte, the addition of magnesium triflate stabilizes the matrix as far as the increase in the degradation temperature was observed in samples containing salt [7]. Also in gelatin electrolytes containing zinc triflate, the degradation temperature of the samples increased with an increase of the salt content, indicating that the addition of salt improved the matrix stabilization [8]. The temperature at the first degradation occurs varies according to the kind and the amount of salt. The same happens in terms of the weight loss that is higher in the less concentrated samples and decreasing with the increase in salt amount. This observation is confirmed by the decrease of the first DTGA peak as can be seen in Figure 3.2 (a). The 1st weight loss of 10 - 40% can be attributed to the degradation of glycerol and/or loss of water. In a starch-CH blend containing 35 wt% of

glycerol and doped with NH_4Cl the weight loss at about 136 - 177ºC is due to the degradation of glycerol in the electrolytes [9]. In cassava-starch films containing glycerol, the stage in 100 - 230ºC is also due to the degradation of glycerol in the polymer membrane [10]. Sometimes, a weight loss in between room temperature and at about 160ºC can been observed. This happened in gellan gum-$LiCF_3SO_3$ polymer electrolytes with a weight loss of 10 - 20%, which can been explained as a water loss in the sample probably due to hydrophilic properties of the salt [11]. The same occurs in salted chitosan acetate (CA-$LiCF_3SO_3$) where in this 1st stage the weight loss is attributed to absorbed water and/or water in the dilute acetic acid used as solvent to dissolve chitosan powder [12]. The relative low value obtained for the T_{onset}, between 130 - 180ºC, is probably due to the presence of acetic acid used as solvent in the films preparation, and also due to the salts added to the matrix, that probably act as a catalyst for the polymeric chain disintegration [2]. However, despite the low values obtained, the T_{onset} for all electrolytes is considered adequate for solid-state electrochemical devices operating under normal conditions.

The second thermal change occur between 200 and 300ºC, it is a weight loss associated to the decomposition of CH, and it explains the second peak in the DTGA curves that appears between 234 - 266ºC, depending on the salt amount, as can be seen in the Figure 3.2 (b). In the DTGA curve, the thermal event at the temperature maximum of ± 270ºC for the matrix, not shown here, is related to the thermal and oxidative decomposition of CH [3]. In a study of gellan gum (HAGG) and CH the DTGA curve of CH hydrogel presents a unique degradation at 302ºC [13]. However, in a hydrogel HAGG-CH the peak related to the CH degradation is shifted to lower temperature (245ºC) due to the interaction of the polymer chains. The values obtained for the doped samples are lower when compared to the obtained for CH matrix (270ºC) and CH hydrogel (302ºC). These differences are also observed in the doped samples, where the less concentrated electrolytes present higher temperatures while the samples with higher salt amount show lower values. The differences in the temperature may be related to the salts added to the CH matrix, which probably acted as catalyst for polymeric chain disintegration.

The third and last stage is more evident for the samples with higher salt levels, as evidenced by the 3rd peak in the DTGA curves, Figure 3.2 (b), whose intensity, in practically all cases, increases with the increase in salt amount. This peak could be due to the different interactions of salt with polysaccharide chain [1].

The degradation process ended at about 500ºC and the weight loss continued slowly as the temperature increase up to 900ºC. The remaining residues represent 10 - 33% in mass of the start materials.

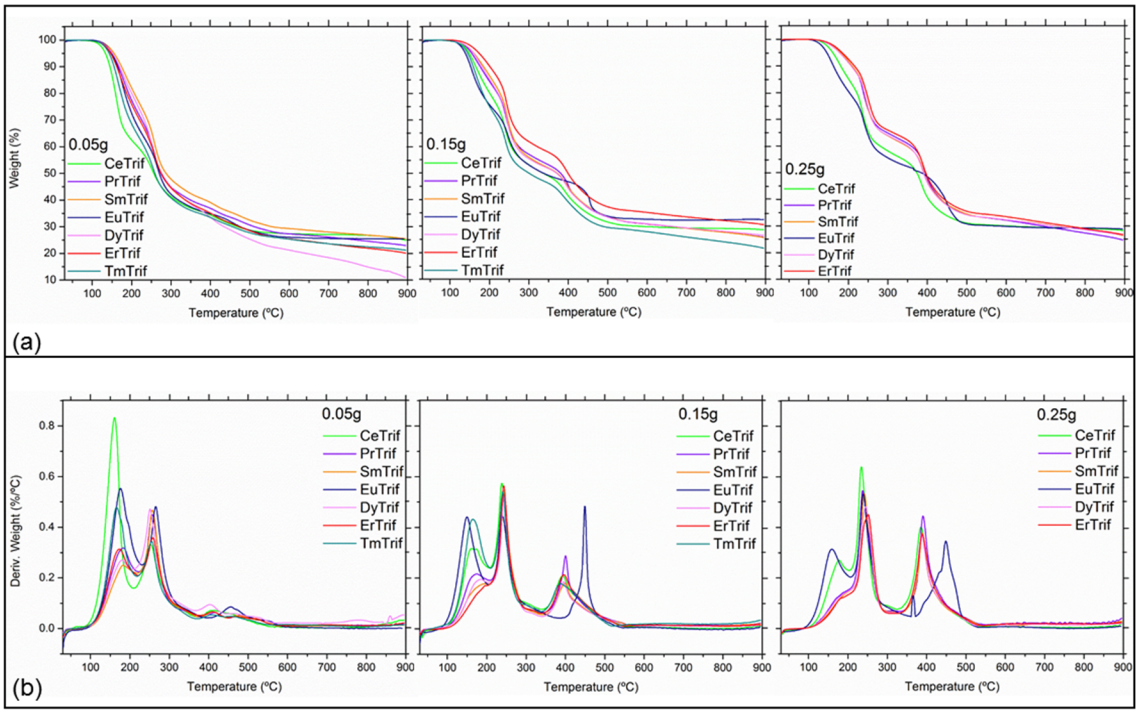

Figure 3.2 (a) TGA and (b) DTGA curves of the electrolytes with different lanthanide salts.

The knowledge of the thermal behavior of the materials is very important in order to obtain more details about their possible practical applications. The DSC, reveals important insights about the degree of crystallinity/amorphosity, melting point (T_m) and glass transition temperature (T_g) [14]. The T_g of the electrolytes is a parameter which provides useful information for understanding their behavior in so far as it can influence the ionic conduction mechanism and the conductivity values [15]. With the decreases in T_g, the amorphous phase becomes more flexible and the conductivity should be enhanced [16]. For electrolytes based on gelatin and $LiClO_4$ salt, the decrease in conductivity is consistent with increasing glass transition temperatures, observed in DSC results [17]. In natural polymers, different T_g values can be obtained because their properties, such as, crystallinity, degree of deacetylation and molecular weight can present in wide variation according to the source and method of extraction [18].

The DSC measurements of the electrolytes were performed in -60 to 200ºC temperature interval and the maximum temperature used was selected to limit CH degradation. The curves obtained for the materials are illustrated in Figure 3.3, and in all cases no baseline changes were observed and so no glass transition temperature was detected. As no T_g was shown, this is an indication that the samples are predominantly amorphous.

Some electrolytes show a large endothermic peak at about 100ºC. In samples were glycerol co-exists with water the boiling point depends of the relative portion of both components. In this case, the boiling point of the mixture would be about 100ºC, which may explain the large endothermic peak at this temperature [2, 19].

Other samples present a large endothermic peak at higher temperature, around 120ºC. This peak may be related to more internal solvent release and/or acetal crosslinking break. The crosslink is formed due to the catalytic properties of acetic acid residues present in the samples. Also in agar-based samples with acetic acid a large endothermic peak is observed, which can be attributed to the disruption of acetal crosslinking [20]. On the other hand, this endothermic event can also been assigned to the sol-gel transition [21].

The remaining samples presented endothermic peaks above 175ºC. The presence of salt and the formation of complexes between the salt and the polymeric matrix and/or the beginning of sample's decomposition are possible explanations for these peaks, accordingly to TGA results.

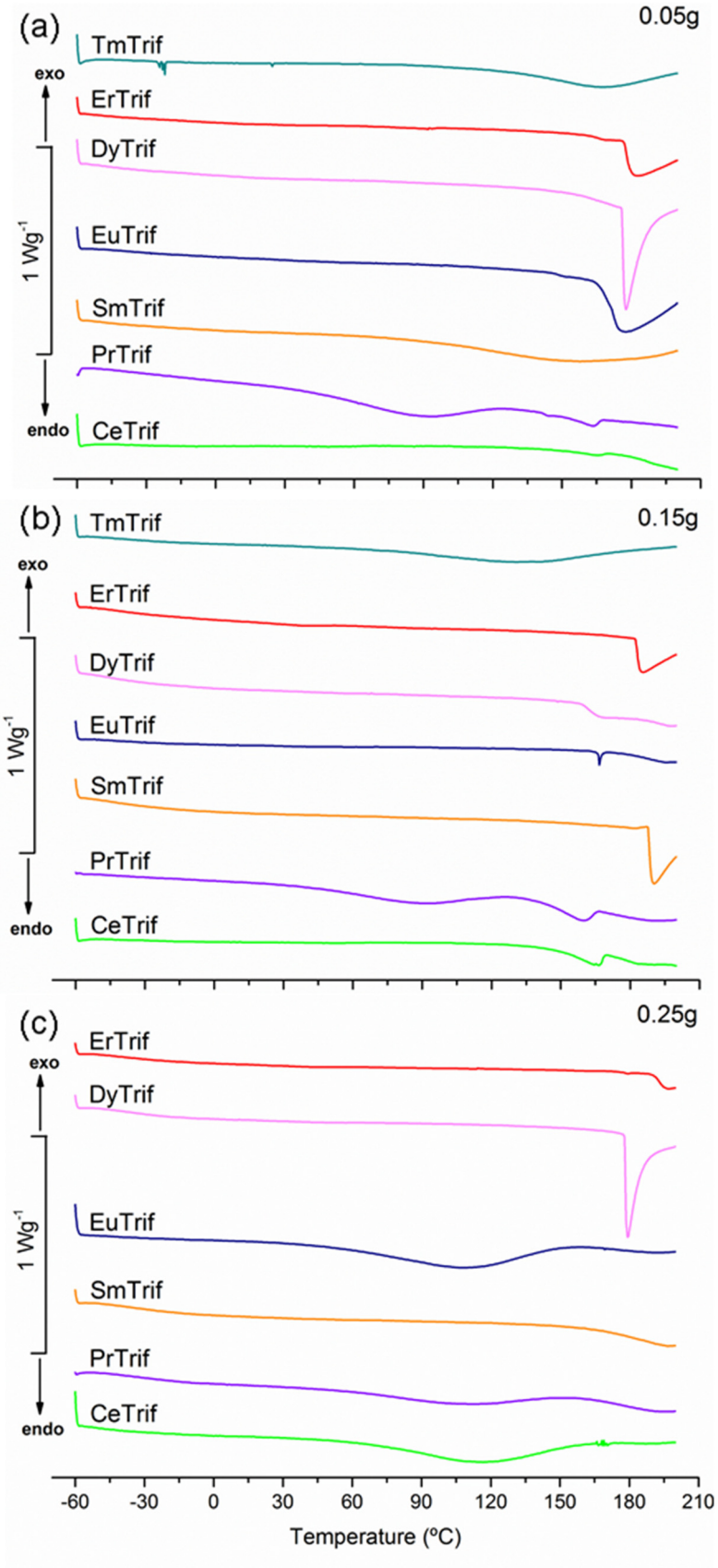

Figure 3.3 DSC curves of the electrolytes with different lanthanide salts.

3.3.2. Impedance spectroscopy

The ionic conductivity of doped samples was determined using the complex impedance method.

Typical plots of imaginary impedance (*-Z''*) versus real impedance (*Z'*) for the electrolytes with different salts at the same temperature (~ 30ºC) and for the electrolytes with different europium amounts at different temperatures are shown in Figure 3.4 and Figure 3.5, respectively. The spectra comprise two well-defined regions in the complex impedance plane: a typical partial arc (semicircle) and a linear region (spike). The semicircle appear in the high frequency zone and corresponds to the bulk response of the films [22]. The linear region is observed in low frequency zone and it is characteristic of capacitive nature of electrode-electrolyte interface [23]. The electrode/electrolyte interface is a capacitance and when it is ideal, a vertical spike parallel to the real axis is found [24]. Normally, an inclined spike at an angle less than 90º is observed instead of the vertical spike probably due to inhomogeneous distribution of salt in polymer matrix or roughness of the electrode/electrolyte interface [25]. From Figure 3.4 it can also be observed that at high frequencies the real part of impedance (*Z'*) tend to zero. The same occurs in DNA-based membranes, which indicates a good contact between the electrode and the electrolyte [26].

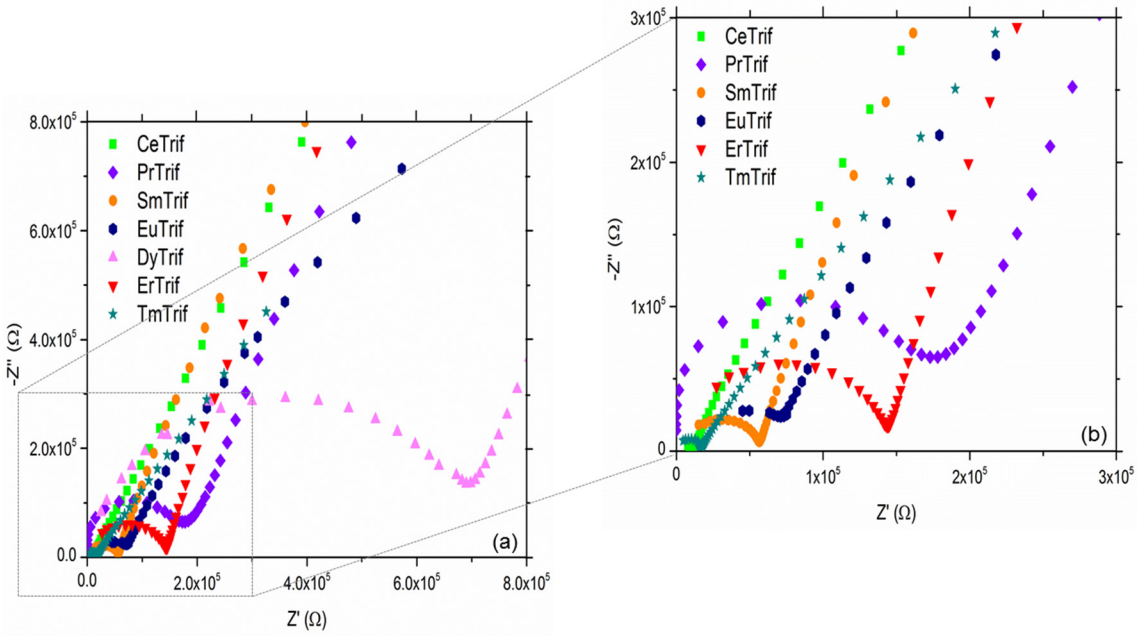

Figure 3.4 Nyquist diagram of the electrolytes with 0.05 g of different lanthanide salts measured at ~ 30ºC.

The intercept of the semicircle with the real axis gives the bulk resistance (R_b) of the material. Figure 3.4 show that the R_b values, for the same temperature, varies according to the salt, which are in very good agreement with the conductivity values discussed in the section below. On another hand, as can observe in the Figure 3.5 (a) and (b), the resistance of the films decrease with increase in temperature. When the temperature increases, the polymer chain acquires segmental motion which favoring hopping inter and intra-chain ion movements leading to the increase in the conductivity [27]. In PE based on CH blended with PEO the semicircle in the high frequency region is also diminished, and disappeared as temperature increases, which implies that the total conductivity is due to ionic conduction [28]. In a conductivity study of a gelatin-based PE the disappearance of a depressed semicircle at high frequency with the temperature reveals just diffusion process and the absence of capacitive nature, and the decrease of the R_b values with the increasing sample temperature is also observed [29]. When compared the two images of Figure 3.5 it can observed that the increase in salt concentration leads to the disappearance of the semicircle, which suggest that only resistive component of PE exist [25]. With the increase in salt concentration, the number of mobile charge carriers also increases, and a decrease of R_b values is observed, leading to an increase in conductivity values. On another hand, the conductivity values are lower when higher R_b values are found, probably due to the recombination of ions, which are responsible for the decrease in the amorphousness of the materials [25].

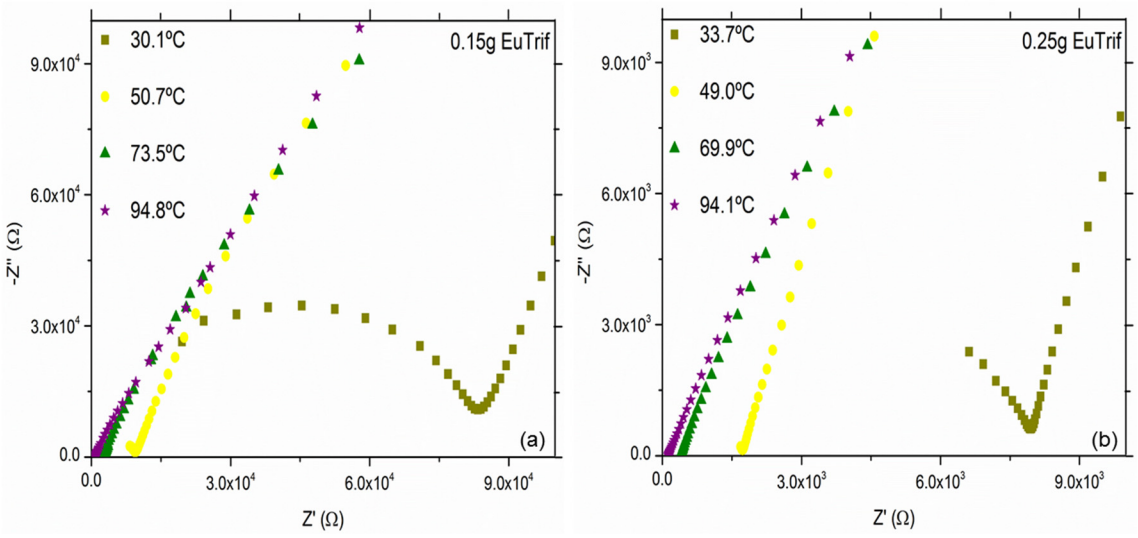

Figure 3.5 Nyquist diagram of the electrolytes with (a) 0.15 and (b) 0.25g of EuTrif, measured at different temperatures.

The R_b values were converted into the ionic conductivity (σ) of the electrolytes according to the equation 3.1:

$$\sigma = \frac{t}{A \times R_b} \tag{3.1}$$

where t is the thickness of sample, and A is the contact area between the electrolyte and the electrode. The experimental values of R_b are dependent on the composition of the PEs and the temperature, as can been observed in Figure 3.6.

The ionic transport in polymer electrolytes is a complex process poorly understood that depends on several factors such as, dielectric constant of host polymer, mobility of polymer chains, degree of salt dissociation and ion aggregation, and the salt concentration, which remains an obstacle in attaining the required room temperature conductivity [30].

Usually, acetic acid at a concentration of 1% is used to solubilize CH and, when CH is dissolved in acidic media, the NH_2 groups are protonated and it becomes a polyelectrolyte [31]. According to the literature, there are two possible proton-conductivity mechanism, namely, vehicle-type and Grotthus-type [32]. In the case of the vehicle mechanism, protons migrate through the medium along with a "vehicle", and in Grotthus mechanism, there are proton hopping and so protons are transferred from one site to another, through the formation and breaking of hydrogen bonds, followed by a local molecular rearrangement [32, 33]. In polymer containing acid, the Grotthus-type hopping mechanism, as called as "packed-acid" mechanism, can occur [34]. This mechanism is supported by transport of H^+ ions to neighboring acid groups, and it can be responsible for the conductivity of dry CH-acetate films [35]. In dry films, the distance between the protonated amino groups of CH-acetate exceeds the one necessary for direct proton hopping and so the acetate ions supported transport of H^+ to neighboring acid groups. In this mechanism, acetate ions interact with amino groups of CH, which results in proton transferred through neighboring acid groups with their reorientation.

The ionic conductivity as a function of temperature measurements of CHLnTrif$_n$-based electrolytes in the temperature range between room temperature and at about 100ºC are

included in Figure 3.6 (a). As can be seen from this figure, the conductivity values are dependent on the temperature, and the kind and the amount of salt used.

The ionic conductivity has been increased with the increment of temperatures and depending on the salt, the concentration and how the ions move within the matrix, the model governing for the ionic transport can be either Arrhenius (equation 3.2) or VTF (equation 3.3) type.

In the case of the samples whose relationship of log σ vs 1000/T is almost linear ($r^2 \sim 1$) this confirms that the dependence of ionic conductivity with temperature obeys to Arrhenius rule. So, the ionic conductivity is thermally activated and the activation energy (E_a) may be calculated according to the equation 3.2:

$$\sigma = \sigma_0 exp\left(\frac{-E_a}{RT}\right) \tag{3.2}$$

where σ_0 is the pre-exponential factor, E_a is the apparent activation energy, R is the gas constant (8.314 J $mol^{-1}K^{-1}$) and T is the temperature. For example, the samples $CHErTrif_{0.05}$ and $CHDyTrif_{0.15}$ had conductivity values of 1.15×10^{-7} and 1.85×10^{-7} S cm^{-1} at 30ºC, and their E_a are respectively 64.91 and 60.14 kJ mol^{-1}. So, the sample with higher conductivity possess lowest activation energy, which is usually expected because the lower energy barrier results in easier ionic movement [36]. The same occurred in the electrolytes $CHDyTrif_{0.15}$ and $CHTmTrif_{0.15}$ where the conductivity increased from 1.85×10^{-7} to 3.14×10^{-7} S cm^{-1} and a decrease in the E_a was observed from 60.14 to 38.19 kJ mol^{-1}.

In other cases, it seems that the mechanism of ionic conduction changes to VTF model (equation 3.3), where the ionic transport is promoted by the viscous medium:

$$\sigma = AT^{-1/2} exp\left[\frac{B}{(T - T_0)}\right] \tag{3.3}$$

where *A* is the constant proportional to the number of carriers ions and *B* is the pseudo-energy of activation. T_0 is the temperature at which the configurational entropy of polymer becomes zero, it represents ideal vitreous transition temperature and so it is suggested to be 50K below the glass transition temperature [37, 38]. However, from the DSC measurements, in the temperature range from -60 to 200ºC, no T_g was observed and so it was impossible to calculate E_a for the samples that showed the VTF behavior of the ionic conductivity as a function of temperature. The VTF fittings match slightly better the experimental results than Arrhenius; however, both fittings are not perfect and it was presume that the activation energy values can been estimated from Arrhenius model. In the case of the samples containing samarium triflate, the experimental points of each sample were fitted with two straight lines (not shown here), that cross at about 53ºC [2]. Probably at this temperature occurs a melting of crystalline phase, as already seen in other samples based on CH [39]. According to the results extracted from these fittings, the E_a values vary between 0.88 - 0.80 eV for low temperature interval, and 0.54 eV above 53ºC for the more conductive samples, and 0.94 - 1.09 eV for low temperature interval and 0.42 - 0.64 eV above 53ºC for the less conductive samples [2].

The ionic conductivity also depends on the cationic and anionic type of charge carriers. In PVdF electrolyte, for the samples with the $CF_3SO_3^-$ anion, the ionic conductivity depends on the cation type and the increase in ion radius promotes an increase in conductivity [40]. Also in lanthanoid silicates, $Ln_{10}(SiO_4)_6O_3$ (Ln = La, Nd, Sm, Gd, Dy, Y, Ho, Er and Yb) the conductivity decreased when Ln^{3+} ions with smaller ionic radii were used [41]. In the case of the present work, for samples with the same $CF_3SO_3^-$ anion, the ionic conductivity depends on the cation type, namely, lanthanide ions. The Ln^{3+} ions have large ionic radii that decrease with the increase in the atomic number, from 1.061 Å (for La^{3+}) to 0.848 Å (to Lu^{3+}), accordingly to the Figure 1.4, but no large variations between them are observed [42]. From Figure 3.6, it can be observed that the salts are ordered according to their atomic number (from 58 (Ce) to 60 (Tm)) and in practically all cases the samples with cerium triflate, that have the highest ionic radii, show the best conductivity values. In other cases, it was expected a decrease in conductivity with the decrease in the radius of the ions, which is not always verified, probably due to the fact that there is a little variation of the radii in the lanthanide series, and therefore this parameter does not have a lot of influence on the observed conductivity differences. The reduction observed in ionic conductivity are probably due to the formation of aggregates

or ionic complexes, and the formation of a hydrogen bond network, that cause a decrease in the number of available diffusible ions [21].

Also the salt concentration influences the ionic conductivity and the optimum salt amount varies depending on the lanthanide used. In the samples containing Pr, Sm, Er and Tm the addition of more than 0.05 g of salt leads to a decrease in the conductivity values. Probably, for these electrolytes this is the optimal amount, and further addition results in the formation of aggregates which leads to a decrease in the mobile ions, and a drop in conductivity. In the case of the samples with Ce and Dy, the conductivity increase when up to 0.15 g was added because more salt is available to dissociate and provide more mobile ions. On another hand, the addition of 0.25 g leads to a decrease in the conductivity values probably because at higher salt levels the ions are able to form neutral ion-pair. For the electrolytes containing europium triflate, the increase in salt amount always promotes an increase in the ionic conductivity, as it can be seen in the Figure 3.6. In this case, the increase in salt amount promotes an increase in the number of the mobile ions, leading to the increase in the ionic conductivity.

In SPEs based on carboxymethyl cellulose doped with ammonium chloride, the increase in ionic conductivity with the salt addition is due to the increment in the number of mobile ions [43]. However, for higher salt amount the ionic conductivity starts to decrease probably due to the association of ions at higher salt level, leading to the formation of ion clusters and a decrease in number of charge carriers and their mobility. In CH-PVA blend film the ionic conductivity increase gradually when 40 wt% salt was added because with the increase in salt content, more salt is available to dissociate and provide more mobile ions [44]. Above 40 wt% the distance between dissociated ions become closer and they are able to recombine and form neutral ion-pairs. So, at higher salt levels, the rate of ions association has to be greater than the rate of ion dissociation, which leads to a decrease in the number density of mobile ions and a drop in ionic conductivity. In PVA-CH-$LiCF_3SO_3$ system, the conductivity increases and a maximum was achieved with 45 wt% of salt, and it can be notified that the increase in the salt leads to the increase of the charge carriers [45]. Further addition of the salt leads to a lower conductivity probably due to the aggregation phenomena where the charge carriers are replaced by clusters resulting in a decrease of the density of mobile ions.

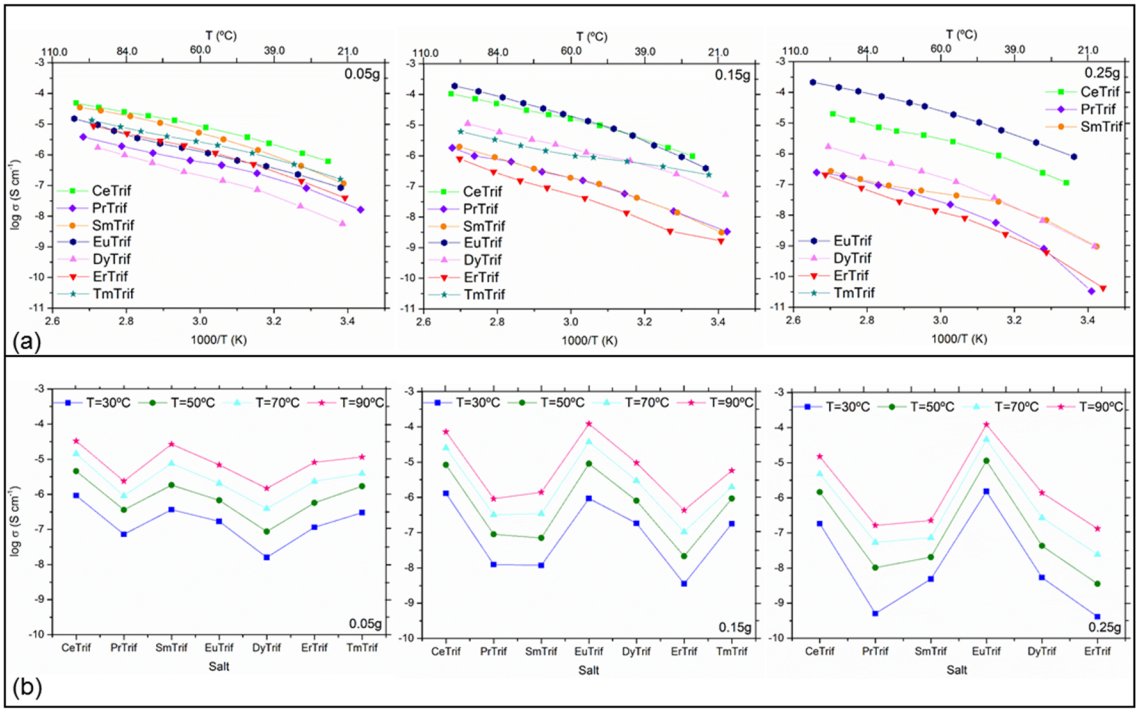

Figure 3.6 (a) Ionic conductivity as function of temperature of CHLnTrif$_n$-based electrolytes; (b) Isothermal curves of log σ vs Salt, obtained at temperatures of 30, 50, 70 and 90ºC.

The CH-based samples with different lanthanide salts and with different salt amounts were subjected to ionic conductivity measurements at 30, 50, 70 and 90ºC. As shown in Figure 3.6 (b) four, five and three ionic conductivity stages can be observed, depending on the salt and the amount used to prepare the electrolytes.

For the samples with 0.05 g of salt four ionic conductivity stages can be observed. The first one is characterized by a decrease in conductivity values from 9.25×10^{-7} S cm^{-1} for the sample with cerium to 7.29×10^{-8} S cm^{-1} for the sample with praseodymium at 30ºC. Next, the ionic conductivity increases and reaches 3.66×10^{-7} S cm^{-1} for the sample containing samarium triflate at 30ºC. In the third stage, the conductivity back to decrease and reaches minimum values of 1.59×10^{-8} S cm^{-1} for the sample with dysprosium salt at 30ºC. In the fourth and last stage the ionic conductivity increases again and 3.02×10^{-7} S cm^{-1} was the maximum obtained for the thulium's sample at 30ºC.

In the case of the samples with 0.15 g of lanthanide salts five ionic conductivity stages can be observed. Once again, in the 1st stage a decrease in conductivity values was obtained from Ce to Pr samples. There are no major changes at the next stage and the

conductivity is very similar for the samples with praseodymium and samarium, namely, 1.25×10^{-8} and 1.19×10^{-8} S cm^{-1} at 30ºC, respectively. Then, the ionic conductivity increases and reaches maximum values of 9.18×10^{-7} S cm^{-1} at 30ºC, for the sample with europium triflate. This value is very similar to those of 1.30×10^{-6} S cm^{-1} at 30ºC obtained for cerium's sample and it is also proven by the identical results as can be seen from the Figure 3.6. In the 4th stage, the ionic conductivity decrease and a minimum value of 3.56×10^{-9} S cm^{-1} at 30ºC was obtained for the electrolyte containing erbium salt. Finally, the conductivity increase again and the sample with thulium triflate show the 3.29×10^{-7} S cm^{-1} value at 30ºC.

In the samples with 0.25 g of salt, three ionic conductivity stages can be observed. Over again, from Ce to Pr samples a decrease in ionic conductivity values was obtained. In the second stage, an increase in conductivity was observed. Initially, the ionic conductivity remains very similar for the samples with Pr and Sm and then increase fastly, and reaches maximum values of 1.52×10^{-6} S cm^{-1} at 30ºC for the sample with europium triflate. In the last stage, a sharp decrease was observed and the minimum of 4.09×10^{-10} S cm^{-1} was obtained for the sample with ErTrif.

3.3.3. X-ray diffraction

X-ray diffraction is a powerful method used to evaluate structural changes in a polymer electrolyte and to determine the crystallinity, where the sharp and broad peaks represent the crystalline and amorphous region, respectively [46]. In PEs the ionic conductivity can be attributed to the amorphous phases, which can be achieved for example by dissolving inorganic acids or salts in a suitable polymer matrix [47]. The high degree of the amorphous nature of the samples weaken the polymer chain backbone, makes the ions conduct faster, and leads to the increase in the ionic conductivity values of the polymer electrolytes [48].

The XRD patterns of the samples are organized according to the conductivity results and, as can be observed in Figure 3.7, the crystallinity/amorphicity of the electrolytes changed due to change in intensity and broadening of peaks, with the addition of salt.

In the electrolytes containing Pr, Sm, Er, and Tm the addition of more than 0.05 g of salt leads to a decrease in the conductivity values, and this decrease may been related to the

decrease in the amorphous phase of the samples. As can observed in Figure 3.7 (a), in the samples with 0.05 g of Pr, Sm and Er the broad nature of the peak at 2θ ~ 20º is higher indicating an increase in the amorphousness. On another hand, the appearance of small sharp peaks in the more concentrated samples are related to the crystalline domains, probably due to the formation of aggregates, responsible to the decrease in the mobile ions, and leading to a drop in conductivity. In the less concentrated thulium's sample, no peaks were observed, which indicates a complete dissolution of the salt in the polymer matrix. Also in PAN (polyacrylonitrile) samples with $LiCF_3SO_3$ the absence of the most peaks pertaining to plasticizer and pure lithium salt indicate a complete dissolution of the plasticizer and salt in the polymer matrix [49].

For the samples containing Ce and Dy the conductivity increases up to 0.15 g of salt amount and further addition results in a decrease in the conductivity. In these cases, the decrease in intensity of the sharp peaks indicate an increase in the amorphous nature and so an increase in conductivity values. Over again, in the more concentrated samples, an increase in the sharp peaks intensity is observed, as can be seen in Figure 3.7 (b), leading to an increase in the crystalline phase of the electrolytes and resulting in a less conductive samples. In a blend starch-CH the crystalline phase decrease when the amount of NH_4Br increased up to 35 wt% [50]. With more than 35 wt% the room temperature conductivity decreases and with 45 wt% crystalline peaks are observed. These crystalline peaks are characteristic peaks of salt, and may be due to recrystallized ions, which are responsible for the decrease in the conductivity.

For the electrolytes containing Eu, the increase in salt amount always promotes an increase in the ionic conductivity. As can been observed in Figure 3.7 (c), the absence of sharp peaks related to the complexes, and the broad peak at 2θ ~ 20º makes the samples more amorphous. In this case, the addition of salt to the host polymer leads to an increase in the charge carriers and the amorphous phase increase due to broadening of the peak, which contributes to conductivity improvement. In the XRD patterns of gelatin-$LiBF_4$ electrolytes no crystalline peaks are observed and only a broad band is seen at 2θ = 20º [51]. Also in this case the absence of any salt crystalline peaks indicates the complete dissolution of the salt in the matrix and the salt complexation.

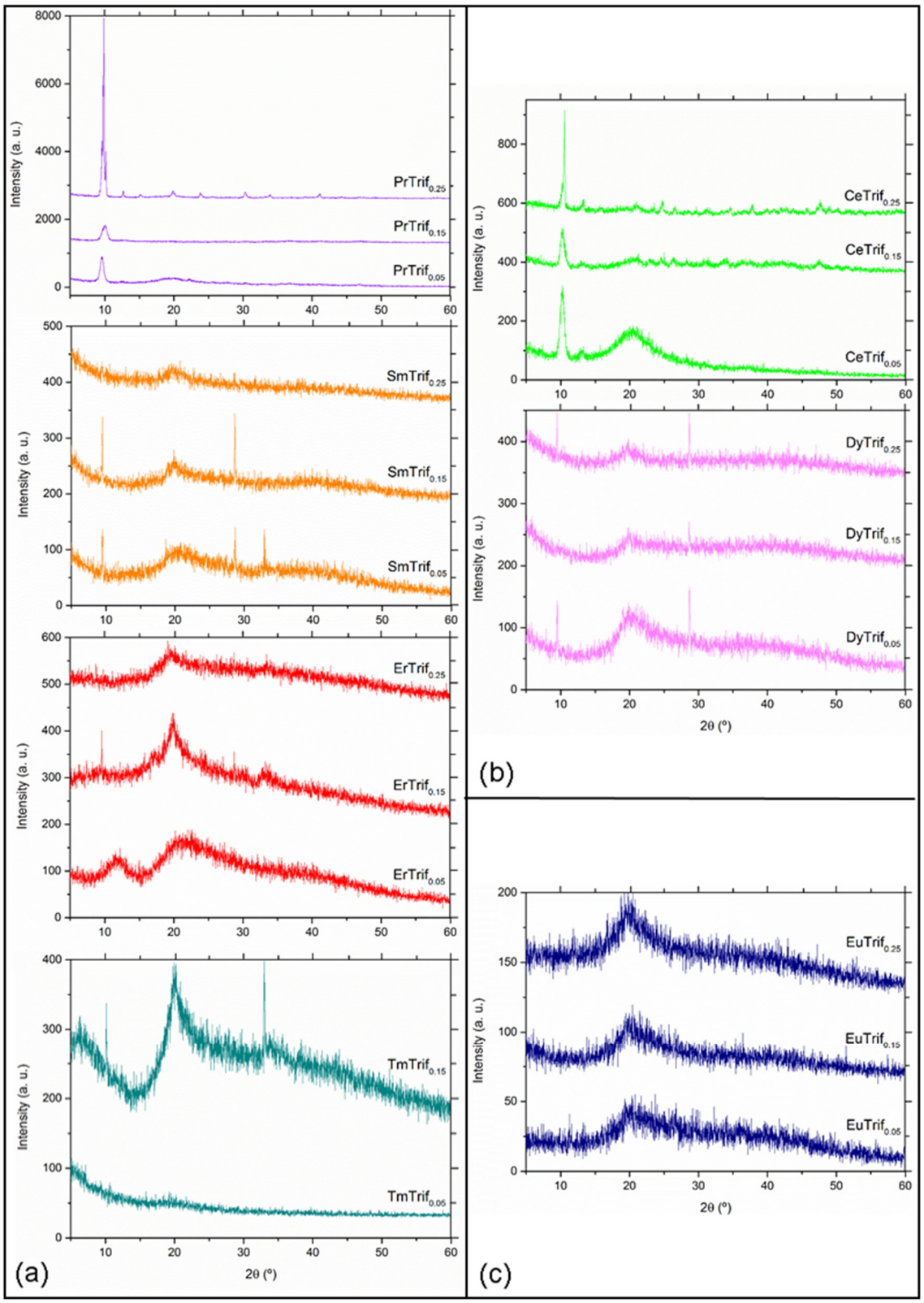

Figure 3.7 XRD patterns of CHLnTrif$_n$-based electrolytes for (a) Ln = Pr, Sm, Er and Tm; (b) Ln = Ce and Dy and (c) Ln = Eu.

3.3.4. Scanning Electron Microscopy and Energy-Dispersive Spectroscopy

SEM micrographs were obtained with the magnification of 500 x and 1.00 kx and practically all less concentrated samples exhibited good homogeneity with no phase separation and good surface uniformity, Figure 3.8. In $SmTrif_{0.05}$ and $ErTrif_{0.05}$ electrolytes some irregularities were observed, which are related with some salt located outside the sample, and can explain the occurrence of small crystalline domains, as suggested by the XRD results. Also in gellan gum electrolytes the presence of crystalline regions is related to ionic liquid not incorporated in the polymer matrix that appeared decorating the polymer [52]. In $DyTrif_{0.05}$ electrolytes some clusters of dysprosium triflate were observed at the sample's surface indicating the occurrence of small crystalline regions, as already observed in XRD.

In some more concentrated samples, $PrTrif_{0.25}$, $CeTrif_{0.25}$ and $DyTrif_{0.25}$, an irregular texture is observed related to the presence of crystalline domains, and these regions corroborate with the sharp peaks observed in XRD results. The SEM micrograph of the most concentrated Pr sample show spherulites that may be related to the crystalline fraction of the material which are in very good agreement with the XRD data. Also in electrolytes based on PEO+$NaClO_4$ with dodecyl amine modified montmorillonite and PEG the SEM micrographs gives the presence of spherulites related to the surface roughness and the crystalline phase of the materials [53].

On another hand, some light lines and very small cracks are observed which are probably due to the dish surface irregularities, where the samples solutions were poured, and also due to the drying process, respectively [54, 55].

Figure 3.9 shows the EDS results of some samples. In electrolytes containing SmTrif, from the EDS spectra, Figure 3.9 (a), it can been concluded that some salt is located outside the sample, which may explain the occurrence of small crystalline regions, as suggested by the XRD results. Figure 3.9 (b) confirm the presence of Dy clusters close to the surface, which also suggest the occurrence of small crystalline regions, accordingly to XRD results. Figure 3.9 (c) shows the EDS results of the samples with 0.05 and 0.25 g of Er salt, and these spectra also suggest that some ErTrif are located outside the sample.

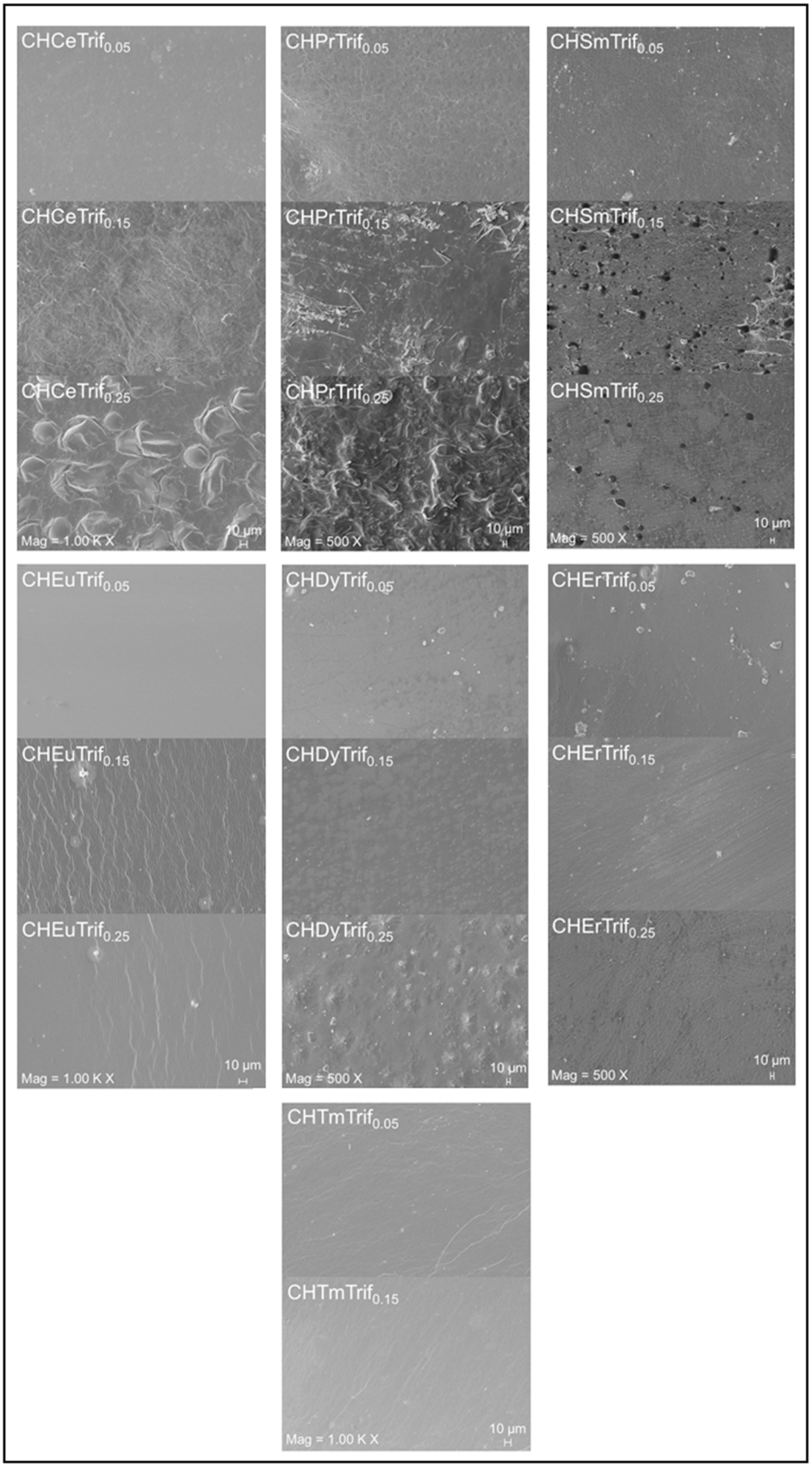

Figure 3.8 SEM micrographs of CHLnTrif$_n$-based electrolytes, for Ln = Ce, Pr, Sm, Eu, Dy, Er and Tm.

On the other hand, the increase in salt amount results in more salt located outside the sample (Figure 3.9 (c2)), and this may explain the lower conductivity values obtained for the sample with 0.25 g, probably due to the decrease in the number of mobile charge carriers.

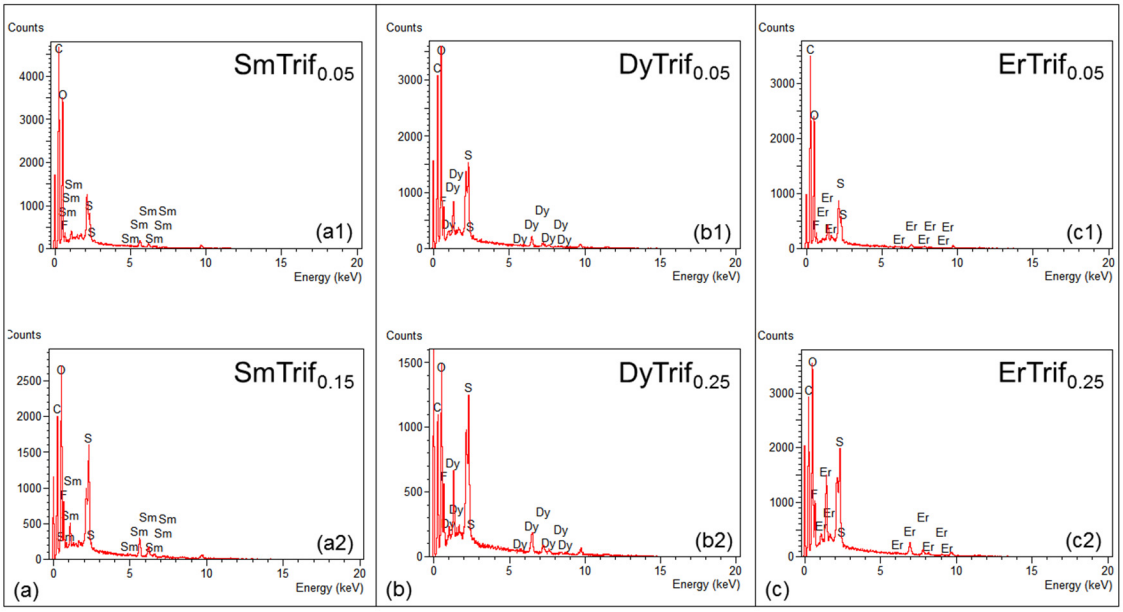

Figure 3.9 EDS results of CHLnTrif$_n$-based electrolytes, for Ln = Sm, Dy, and Er

3.3.5. Atomic Force Microscopy

The changes on the surface topography were evaluated by AFM analysis and Figure 3.10 displays the morphological characteristics of the samples.

In the ErTrif samples, with scanning area of 2.0 µm x 2.0 µm, the higher value of 16.9 nm was obtained for the more conductive electrolyte and this value decrease until reach a minimum of 2.82 nm for the less conductive sample, as can be seen in Figure 3.10 (a). In DyTrif electrolytes, Figure 3.10 (b), the scanning area was 5.0 µm x 5.0 µm and similar behavior was observed. The sample with highest roughness (23.6 nm) also presented highest conductivity value, while the smoothest one (5.65 nm) presented the lowest conductivity value. In carbon nanotubes-polyethylene oxide (CN-PEO) composite the increase in conductivity was observed in samples with higher roughness which may be attributed to the decrease in the sample's crystallinity [56]. Probably, the highest roughness might create a large number of voids and free spaces for easy transportation of charge carriers and so the ions could easily migrate, leading to a high ionic conductivity.

The opposite occurred in the CeTrif and SmTrif samples. In Ce-based electrolytes, with scanning area of 2.0 µm x 2.0 µm, the sample with highest salt amount is one of the less conductive, and is presents highest roughness (8.43 nm) while the lower roughness (3.72 nm) was obtained for the more conductive electrolyte, Figure 3.10 (c). Also in SmTrif electrolytes, with scanning area was 5.0 µm x 5.0 µm, the less conductive sample show high roughness value (35.0 nm) while the sample with low roughness (9.81 nm) is the more conducting, Figure 3.10 (d). In thin films, the roughness of the samples promotes an incomplete contact between the electrode and the electrolyte [57]. Therefore, the contact area is not continuous and consists of many discrete points contacts, and then the current not pass the whole cross-section, which leads to the conductivity decrement.

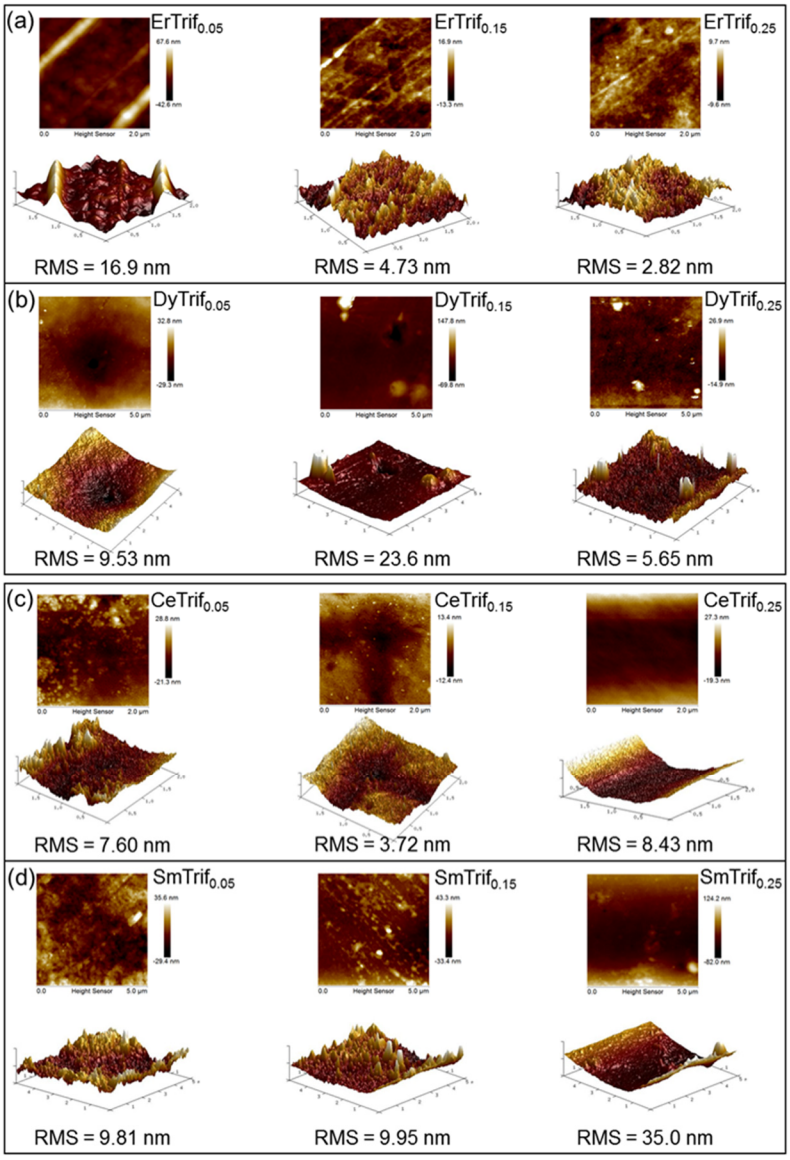

Figure 3.10 AFM images of CHLnTrif$_n$-based electrolytes, for Ln = Er (a), Dy (b), Ce (c) and Sm (d).

3.4. Conclusion

The samples were obtained by solvent cast method and the influence of the different lanthanide salts in the CH matrix was evaluated. In relation to the thermal behavior, all electrolytes showed a multi-step decomposition behavior probably due to the different interactions of the salts and the plasticizer with the polysaccharide chain. The 1st degradation starts at between 130 - 180ºC and practically all samples presented higher T_{onset} than the matrix. Therefore, this means that the addition of the salt contributed to an increase in the thermal stability of the electrolytes. The temperature at the first degradation occurs varies according to the kind and the amount of salt, and the same happens in terms of the weight loss that is higher in the less concentrated samples and decreasing with the increase in salt amount. In DSC results, as no T_g was shown, this is an indication that the samples are predominantly amorphous. The ionic conductivity has been increased with the increment of temperature and depending on the salt, the concentration and how the ions move within the matrix, the model governing for the ionic transport can be either Arrhenius or VTF type. In the case of the samples whose relationship is almost linear, the dependence of ionic conductivity with temperature obeys to Arrhenius rule. In other cases, it seems that the mechanism of ionic conduction changes to VTF model, where the ionic transport is promoted by the viscous medium. The ionic conductivity also depends on the cationic and anionic type of charge carriers. The samples present the same $CF_3SO_3^-$ anion, and so the ionic conductivity depends on the cation type, namely, lanthanide ions. In practically all cases the samples with cerium triflate, that have the highest ionic radii, they show the best conductivity values. In other cases, it was expected a decrease in conductivity with the decrease in the radius of the ions, which is not always verified, probably due to the fact that there is a little variation of the radii in the lanthanide series, and therefore this parameter does not have a lot of influence on the observed conductivity differences. Also the salt concentration influences the ionic conductivity and the optimum salt amount varies depending on the lanthanide used. The XRD patterns of the samples revealed that the crystallinity/amorphicity of the electrolytes changed due to change in intensity and broadening of peaks, with the addition of salt. In the samples with 0.05 g of Pr, Sm and Er the broad nature of the peak at $2\theta \sim 20º$ is higher indicating an increase in the amorphousness. On another hand, the appearance of small sharp peaks in the more concentrated samples are related to the crystalline domains, probably due to the formation of aggregates responsible to the decrease in the mobile ions

and leading to a drop in conductivity. SEM micrographs showed that practically all less concentrated samples exhibited good homogeneity with no phase separation and good surface uniformity. However, some irregularities were observed which are related with some salt located outside the sample, as observed in EDS spectra, and can explain the occurrence of small crystalline domains, as suggested by the XRD results. In relation to the AFM results, the highest roughness obtained in some cases, might create a large number of voids and free spaces for easy transportation of charge carriers, and so the ions could easily migrate, leading to a high ionic conductivity. In other cases, due to the higher roughness, the contact area is not continuous and consists of many discrete points contacts, and then the current not pass the whole cross-section, which leads to the conductivity decrement.

3.5. References

[1] R. Alves, F. Sentanin, R.C. Sabadini, A. Pawlicka, M.M. Silva, Influence of cerium triflate and glycerol on electrochemical performance of chitosan electrolytes for electrochromic devices, Electrochimica Acta, 217 (2016) 108-116.

[2] R. Alves, F. Sentanin, R.C. Sabadini, M. Fernandes, V. de Zea Bermudez, A. Pawlicka, M.M. Silva, Samarium (III) Triflate-doped Chitosan Electrolyte for Solid State Electrochromic Devices, Electrochimica Acta, (2017) *in press*.

[3] R. Alves, J.P. Donoso, C.J. Magon, I.D.A. Silva, A. Pawlicka, M.M. Silva, Solid polymer electrolytes based on chitosan and europium triflate, Journal of Non-Crystalline Solids, 432 (2016) 307-312.

[4] R. Alves, F. Sentanin, R.C. Sabadini, A. Pawlicka, M.M. Silva, Solid polymer electrolytes based on chitosan and $Dy(CF_3SO_3)_3$ for electrochromic devices, Solid State Ionics, 310 (2017) 112-120.

[5] R. Alves, F. Sentanin, R.C. Sabadini, A. Pawlicka, M.M. Silva, Green polymer electrolytes of chitosan doped with erbium triflate, Journal of Non-Crystalline Solids, 482 (2018) 183-191.

[6] R. Alves, F. Sentanin, R.C. Sabadini, A. Pawlicka, M.M. Silva, Innovative electrolytes based on chitosan and thulium for solid state applications: synthesis, structural, and thermal characterization, Journal of Electroanalytical Chemistry, 788 (2017) 156-164.

[7] R.D. Alves, L.C. Rodrigues, J.R. Andrade, A. Pawlicka, L. Pereira, R. Martins, E. Fortunato, M.M. Silva, Study and Characterization of a Novel Polymer Electrolyte Based

on Agar Doped with Magnesium Triflate, Molecular Crystals and Liquid Crystals, 570 (2013) 1-11.

[8] R.D. Alves, L.C. Rodrigues, J.R. Andrade, M. Fernandes, J.V. Pinto, L. Pereira, A. Pawlicka, R. Martins, E. Fortunato, V. de Zea Bermudez, $Gelatin_nZn(CF_3SO_3)_2$ polymer electrolytes for electrochromic devices, Electroanalysis, 25 (2013) 1483-1490.

[9] M.F. Shukur, R. Ithnin, M.F.Z. Kadir, Electrical properties of proton conducting solid biopolymer electrolytes based on starch-chitosan blend, Ionics, 20 (2014) 977-999.

[10] G. Ayala Valencia, A. Agudelo, R. Zapata, Effect of glycerol on the electrical properties and phase behavior of cassava starch biopolymers, DYNA, 171 (2012) 138-147.

[11] I.S.M. Noor, S.R. Majid, A.K. Arof, D. Djurado, S. Claro Neto, A. Pawlicka, Characteristics of gellan gum-$LiCF_3SO_3$ polymer electrolytes, Solid State Ionics, 225 (2012) 649-653.

[12] Z. Osman, Thermal and conductivity studies of chitosan acetate-based polymer electrolytes, Ionics, 11 (2005) 397-401.

[13] R.C. Sabadini, V.C.A. Martins, A. Pawlicka, Synthesis and characterization of gellan gum: chitosan biohydrogels for soil humidity control and fertilizer release, Cellulose, 22 (2015) 2045-2054.

[14] R.C. Agrawal, G.P. Pandey, Solid polymer electrolytes: materials designing and all-solid-state battery applications: an overview, Journal of Physics D: Applied Physics, 41 (2008) 223001 (18pp).

[15] M.M. Silva, S.C. Barros, M.J. Smith, J.R. MacCallum, Characterization of solid polymer electrolytes based on poly(trimethylenecarbonate) and lithium tetrafluoroborate, Electrochimica Acta, 49 (2004) 1887-1891.

[16] L. Fan, C.-W. Nan, S. Zhao, Effect of modified SiO_2 on the properties of PEO-based polymer electrolytes, Solid State Ionics, 164 (2003) 81-86.

[17] D.F. Viera, C.O. Avellaneda, A. Pawlicka, A.C Impedance, X-ray Diffraction and DSC Investigation on Gelatin Based-Electrolyte with $LiClO_4$, Molecular Crystals and Liquid Crystals, 485 (2008) 843-852.

[18] Y.M. Yusof, H.A. Illias, M.F. Shukur, M.F.Z. Kadir, Characterization of starch-chitosan blend-based electrolyte doped with ammonium iodide for application in proton batteries, Ionics, 23 (2017) 681-697.

[19] H.M. Trimble, W. Potts, Glycol-water mixtures vapor pressure-boiling point-composition relations, Industrial & Engineering Chemistry, 27 (1935) 66-68.

[20] E. Lima, E. Raphael, F. Sentanin, L.C. Rodrigues, R.A.S. Ferreira, L.D. Carlos, M.M. Silva, A. Pawlicka, Photoluminescent polymer electrolyte based on agar and containing europium picrate for electrochemical devices, Materials Science and Engineering: B, 177 (2012) 488-493.

[21] S.C. Nunes, R.F.P. Pereira, N. Sousa, M.M. Silva, P. Almeida, F.M.L. Figueiredo, V. de Zea Bermudez, Eco-Friendly Red Seaweed-Derived Electrolytes for Electrochemical Devices, Advanced Sustainable Systems, 1 (2017) (17pp).

[22] Y. Wan, K.A.M. Creber, B. Peppley, V.T. Bui, Ionic conductivity of chitosan membranes, Polymer, 44 (2003) 1057-1065.

[23] K. Mishra, S.S. Pundir, D.K. Rai, Effect of polysorbate plasticizer on the structural and ion conduction properties of PEO-NH_4PF_6 solid polymer electrolyte, Ionics, 23 (2017) 105-112.

[24] G.M. Wu, S.J. Lin, C.C. Yang, Preparation and characterization of PVA/PAA membranes for solid polymer electrolytes, Journal of Membrane Science, 275 (2006) 127-133.

[25] Y.M. Yusof, H.A. Illias, M.F.Z. Kadir, Incorporation of NH_4Br in PVA-chitosan blend-based polymer electrolyte and its effect on the conductivity and other electrical properties, Ionics, 20 (2014) 1235-1245.

[26] A. Pawlicka, F. Sentanin, A. Firmino, J.G. Grote, F. Kajzar, I. Rau, Ionically conducting DNA-based membranes for eletrochromic devices, Synthetic Metals, 161 (2011) 2329-2334.

[27] Y.N. Sudhakar, M. Selvakumar, Lithium perchlorate doped plasticized chitosan and starch blend as biodegradable polymer electrolyte for supercapacitors, Electrochimica Acta, 78 (2012) 398-405.

[28] M.H. Buraidah, L.P. Teo, C.M. Au Yong, S. Shah, A.K. Arof, Performance of polymer electrolyte based on chitosan blended with poly(ethylene oxide) for plasmonic dye-sensitized solar cell, Optical Materials, 57 (2016) 202-211.

[29] D.F. Vieira, C.O. Avellaneda, A. Pawlicka, Conductivity study of a gelatin-based polymer electrolyte, Electrochimica Acta, 53 (2007) 1404-1408.

[30] S.B. Aziz, Z.H.Z. Abidin, Electrical Conduction Mechanism in Solid Polymer Electrolytes: New Concepts to Arrhenius Equation, Journal of Soft Matter, 2013 (2013) (8pp).

[31] M. Rinaudo, G. Pavlov, J. Desbrières, Influence of acetic acid concentration on the solubilization of chitosan, Polymer, 40 (1999) 7029-7032.

[32] Z. Zuo, Y. Fu, A. Manthiram, Novel Blend Membranes Based on Acid-Base Interactions for Fuel Cells, Polymers, 4 (2012) 1627-1644.

[33] G.A. Ludueña, T.D. Kühne, D. Sebastiani, Mixed Grotthuss and Vehicle Transport Mechanism in Proton Conducting Polymers from Ab initio Molecular Dynamics Simulations, Chemistry of Materials, 23 (2011) 1424-1429.

[34] T. Ogawa, K. Kamiguchi, T. Tamaki, H. Imai, T. Yamaguchi, Differentiating Grotthuss Proton Conduction Mechanisms by Nuclear Magnetic Resonance Spectroscopic Analysis of Frozen Samples, Analytical Chemistry, 86 (2014) 9362-9366.

[35] E. Prokhorov, G. Luna-Bárcenas, J.B. González-Campos, Y. Kovalenko, Z.Y. García-Carvajal, J. Mota-Morales, Proton conductivity and relaxation properties of chitosan-acetate films, Electrochimica Acta, 215 (2016) 600-608.

[36] R. Alves, L.P. Ravaro, A. Pawlicka, M.M. Silva, A.S.S. de Camargo, Eco-Friendly Luminescent Hybrid Materials Based on Eu^{III} and Li^{I} Co-Doped Chitosan, Journal of the Brazilian Chemical Society, 26 (2015) 2590-2597.

[37] P.V. Wright, Polymer electrolytes-the early days, Electrochimica Acta, 43 (1998) 1137-1143.

[38] J.J. Fontanella, Pressure and Temperature Variation of the Electrical Conductivity of Poly(propylene glycol) containing $LiCF_3SO_3$, The Journal of Chemical Physics, 111 (1999) 7103-7109.

[39] A. Pawlicka, M. Danczuk, W. Wieczorek, E. Zygadło-Monikowska, Influence of plasticizer type on the properties of polymer electrolytes based on chitosan, The Journal of Physical Chemistry A, 112 (2008) 8888-8895.

[40] C.M. Costa, R. Leones, M.M. Silva, S. Lanceros-Mendez, Influence of different salts in poly(vinylidene fluoride-co-trifluoroethylene) electrolyte separator membranes for battery applications, Journal of Electroanalytical Chemistry, 727 (2014) 125-134.

[41] S. Nakayama, T. Kageyama, H. Aono, Y. Sadaoka, Ionic conductivity of lanthanoid silicates, $Ln_{10}(SiO_4)_6O_3$ (Ln= La, Nd, Sm, Gd, Dy, Y, Ho, Er and Yb), Journal of Materials Chemistry, 5 (1995) 1801-1805.

[42] D.G. Karraker, Coordination of trivalent lanthanide ions, Journal of Chemical Education, 47 (1970) 424-430.

[43] N.H.B. Ahmad, M.I.N.B.M. Isa, Proton conducting solid polymer electrolytes based carboxymethyl cellulose doped ammonium chloride: ionic conductivity and transport studies, International Journal of Plastics Technology, 19 (2015) 47-55.

[44] M.F.Z. Kadir, S.R. Majid, A.K. Arof, Plasticized chitosan-PVA blend polymer electrolyte based proton battery, Electrochimica Acta, 55 (2010) 1475-1482.

[45] N.A.A. Razak, T. Winie, F.S.A. Ghani, A.H. Ahmad, Conductivity and Ftir Studies on Pva/Chitosan-$LiCF_3SO_3$, Solid State Science and Technology, 16 (2008) 1-7.

[46] N.A.A. Amran, N.S.A. Manan, M.F.Z. Kadir, The effect of $LiCF_3SO_3$ on the complexation with potato starch-chitosan blend polymer electrolytes, Ionics, 22 (2016) 1647-1658.

[47] M.V.L. Chandra, S. Karthikeyan, S. Selvasekarapandian, D.V. Pandi, S. Monisha, S.A. Packiaseeli, Characterization of high ionic conducting PVAc-PMMA blend-based polymer electrolyte for electrochemical applications, Ionics, 22 (2016) 2409-2420.

[48] N.A.A. Latip, H.M. Ng, N. Farah, K. Ramesh, S. Ramesh, S. Ramesh, Novel development towards preparation of highly efficient ionic liquid based co-polymer electrolytes and its application in dye-sensitized solar cells, Organic Electronics, 41 (2017) 33-41.

[49] A. Ahmad, K.B.M. Isa, Z. Osman, Conductivity and structural studies of plasticized polyacrylonitrile (PAN)-lithium triflate polymer electrolyte films, Sains Malaysiana, 40 (2011) 691-694.

[50] M.F. Shukur, R. Ithnin, M.F.Z. Kadir, Protonic transport analysis of starch-chitosan blend based electrolytes and application in electrochemical device, Molecular Crystals and Liquid Crystals, 603 (2014) 52-65.

[51] D.F. Vieira, A. Pawlicka, Optimization of performances of gelatin/$LiBF_4$-based polymer electrolytes by plasticizing effects, Electrochimica Acta, 55 (2010) 1489-1494.

[52] M.J. Neto, F. Sentanin, J.M.S.S. Esperança, M.J. Medeiros, A. Pawlicka, V. de Zea Bermudez, M.M. Silva, Gellan gum-Ionic liquid membranes for electrochromic device application, Solid State Ionics, 274 (2015) 64-70.

[53] D.K. Pradhan, R.N.P. Choudhary, B. Samantaray, Studies of dielectric relaxation and AC conductivity behavior of plasticized polymer nanocomposite electrolytes, International Journal of Electrochemical Science, 3 (2008) 597-608.

[54] R. Leones, R.C. Sabadini, F.C. Sentanin, J.M.S.S. Esperança, A. Pawlicka, M.M. Silva, Polymer electrolytes for electrochromic devices through solvent casting and sol-gel routes, Solar Energy Materials and Solar Cells, 169 (2017) 98-106.

[55] R. Leones, M.B.S. Botelho, F. Sentanin, I. Cesarino, A. Pawlicka, A.S.S. de Camargo, M. Silva, Pectin-based polymer electrolytes with Ir (III) complexes, Molecular Crystals and Liquid Crystals, 604 (2014) 117-125.

[56] M.S. Akhtar, J.-G. Park, H.-C. Lee, S.-K. Lee, O.-B. Yang, Carbon nanotubes-polyethylene oxide composite electrolyte for solid-state dye-sensitized solar cells, Electrochimica Acta, 55 (2010) 2418-2423.

[57] E. Wanzenberg, F. Tietz, D. Kek, P. Panjan, D. Stöver, Influence of electrode contacts on conductivity measurements of thin YSZ electrolyte films and the impact on solid oxide fuel cells, Solid State Ionics, 164 (2003) 121-129.

Chapter 4

Luminescent polymer electrolytes based on chitosan and containing europium triflate

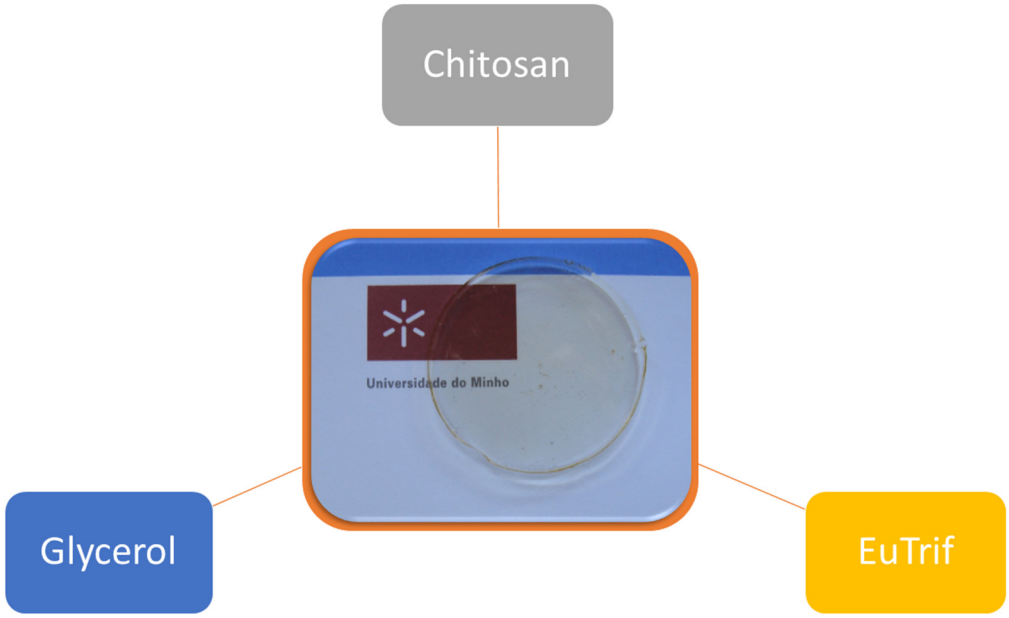

This chapter was adapted from: R. Alves, A. S. S. de Camargo, A. Pawlicka, M. M. Silva, Luminescent polymer electrolytes based on chitosan and containing europium triflate, Journal of Rare Earths 34 (2016) 661-666.

4.1. Objective

The main objective of this chapter is verify the luminescent properties of CH-based electrolytes doped with europium triflate. The luminescent behavior of europium ions in suitable polymer hosts has suggested that future developments may lead to the multicomponent solid-state displays, but with the added attraction of processing, which polymer host can provide.

4.2. Experimental section

Samples were prepared according to the procedure described previous in chapter 2, and in Figure 4.1 is presented the electrolytes physical appearance. The notation CHEuTrif$_n$ represents the samples, where *n* corresponds to the mass of the europium triflate salt. The thickness of the samples varied between 0.070 and 0.145 ± 0.001 mm.

Figure 4.1 Photograph of a representative electrolyte film.

The samples were characterized by XRD, SEM, AFM, and photoluminescence spectroscopy.

4.3. Results and discussion

4.3.1 Morphology and structure

Figure 4.2 shows the characteristic room temperature X-ray diffraction profile obtained for pure CH and samples plasticized with glycerol, containing different quantities of

$Eu(CF_3SO_3)_3$. For pure CH one can observe a broad band centered at 2θ ≈ 20.6º, but the XRD patterns change with the addition of the europium salt. The Gaussian-shaped broad non-resolved band, centered at about 2θ = 20.6º in the diffractograms depicted in Figure 4.2, confirms the predominantly amorphous structure of the polymer electrolytes studied here. This result may be interpreted as an indication that the polymer chains are essentially in a disordered regime. Also, the XRD diffractograms reveal that the profile of this band changes slightly depending on the sample. In a study of CH and NH_4Cl, a peak at 2θ ≈ 20º suggests the amorphous nature of the PEs, and it is weakened and broadened with increase of salt concentration. When the salt concentration is lower than 30 wt%, there is a destruction of the crystalline part of the polymer chain, which promotes the amorphous nature [1]. This behavior is similar to that of other ionic conducting membranes based on natural macromolecules as for example electrolytes based on DNA [2]. In a work describing a series of luminescent and ion-conducting ormosils with europium triflate, the undoped ureasils presented semi-crystalline nature with characteristic peaks of crystalline PEO (2θ = 23.1º, 19.0º, and 35.7º). For compositions n = 37 wt%, 52 wt%, and 92 wt%, the peaks disappear completely, which indicates that the salt induces long-range disorder [3].

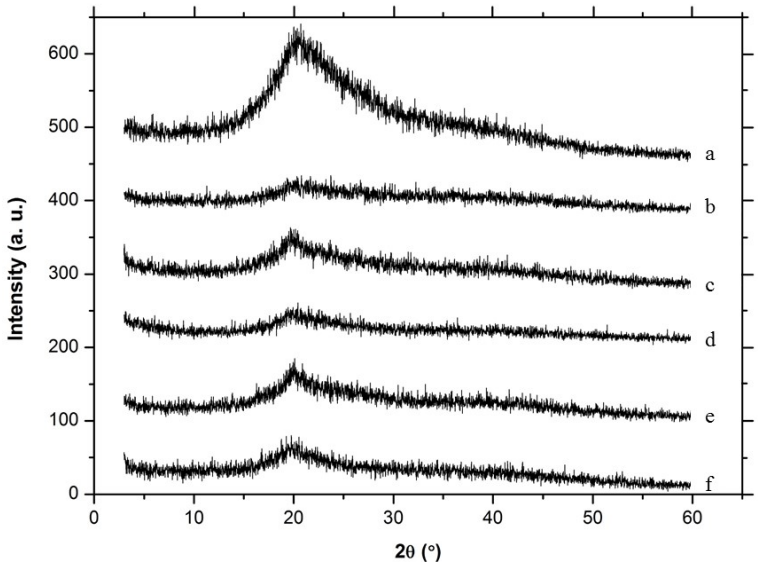

Figure 4.2 XRD of plasticized CHEuTrif$_n$, for *n* = 0.00 (a), 0.05 (b), 0.10 (c), 0.15 (d), 0.20 (e), and 0.25 g (f).

The morphological characteristics of CH doped with europium triflate were also examined by AFM. Figure 4.3 displays characteristic images of the CHEuTrif*n* samples. There are two principal modes of AFM: contact and tapping mode [4], and tapping mode was used in this case. AFM analyses were carried out in order to evaluate the homogeneity and changes in the surface topography of developed electrolytes. The scanning area was 10 μm × 10 μm. The roughness of CH electrolytes are presented in Table 4.1.

Table 4.1 Roughness average (RMS) of CH electrolytes.

Sample	RMS (nm)
$CHEuTrif_{0.00}$	11.9
$CHEuTrif_{0.05}$	12.6
$CHEuTrif_{0.10}$	17.5
$CHEuTrif_{0.15}$	14.2
$CHEuTrif_{0.20}$	19.4
$CHEuTrif_{0.25}$	4.39

In addition, the surface scanning by AFM was conducted in different areas to obtain average values. Figure 4.3 displays typical AFM images of the membranes where one can observe that the samples with higher quantity of the europium salt (Figure 4.3 (f)) promoted a formation of the membrane with smoother surface when compared with the sample with lower quantity of $Eu(CF_3SO_3)_3$ (Figure 4.3 (b, c, and e)). Therefore, the roughness mean square (RMS) of the $CHEuTrif_{0.05}$ was 12.6 nm and that of the $CHEuTrif_{0.25}$ was 4.39 nm.

$CHEuTrif_{0.25}$ was the most conductive sample (1.52×10^{-6} S cm^{-1}, at 25ºC) [5] and presented smaller roughness (4.39 nm). The less conductive sample, $CHEuTrif_{0.20}$ (7.53×10^{-8} S cm^{-1}, at 25ºC), shows higher roughness (19.4 nm). From the obtained results it was stated that the most conductive sample exhibited a lower surface roughness value. This behavior is opposite to those referred in literature [6] with the same salt.

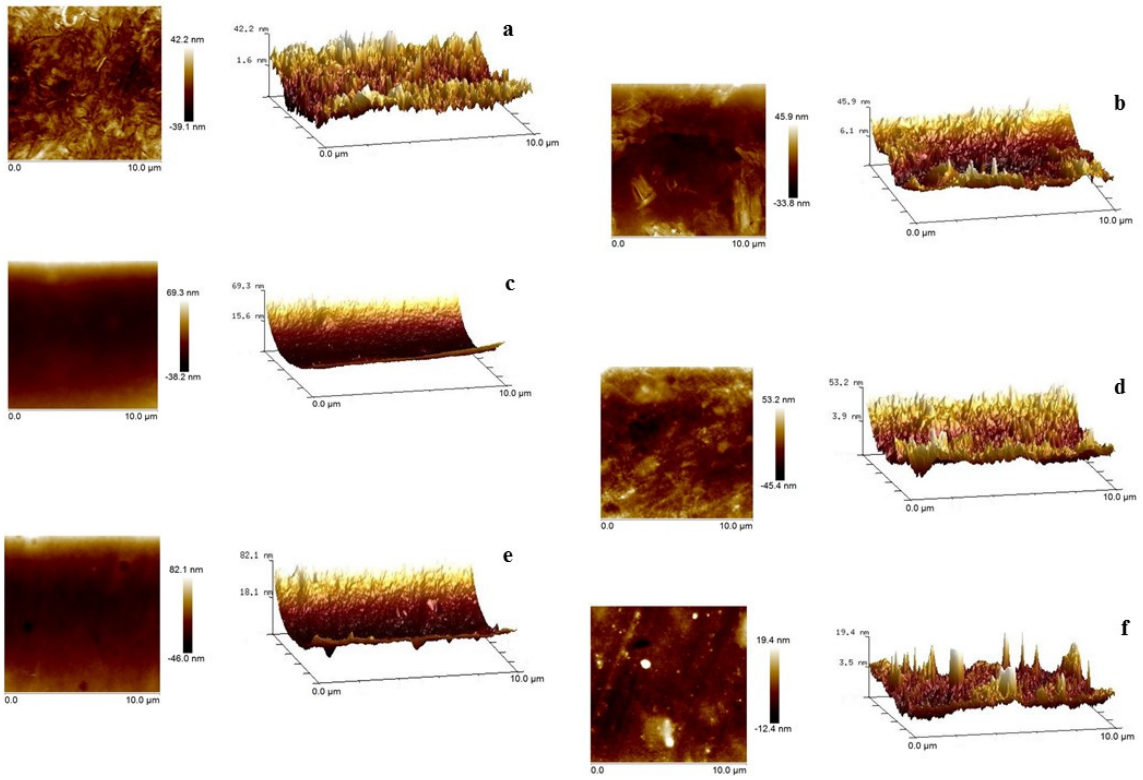

Figure 4.3 AFM images of plasticized CHEuTrif$_n$, for n = 0.00 (a), 0.05 (b), 0.10 (c), 0.15 (d), 0.20 (e), and 0.25 g (f).

The good homogeneity without any phase separation and very good surface uniformity of samples containing 0.00, 0.05, 0.10, and 0.25 g of Eu^{3+}-triflate can be observed in the SEM micrographs in Figure 4.4 (a, b, c, and e). Similar results were obtained for agar-based films [7]. The other samples, namely 0.15 and 0.20 g do not exhibit good surface uniformity and showed some imperfections on the surface, which can be related to incomplete dissociation of salt or clusters formation. The morphology is related to the influence of salt content on the ionic conductivity. The samples that presented good surface uniformity and homogeneity show best ionic conductivity values. These results may explain the conductivity decrease in the samples of CH and europium triflate obtained in another study [5].

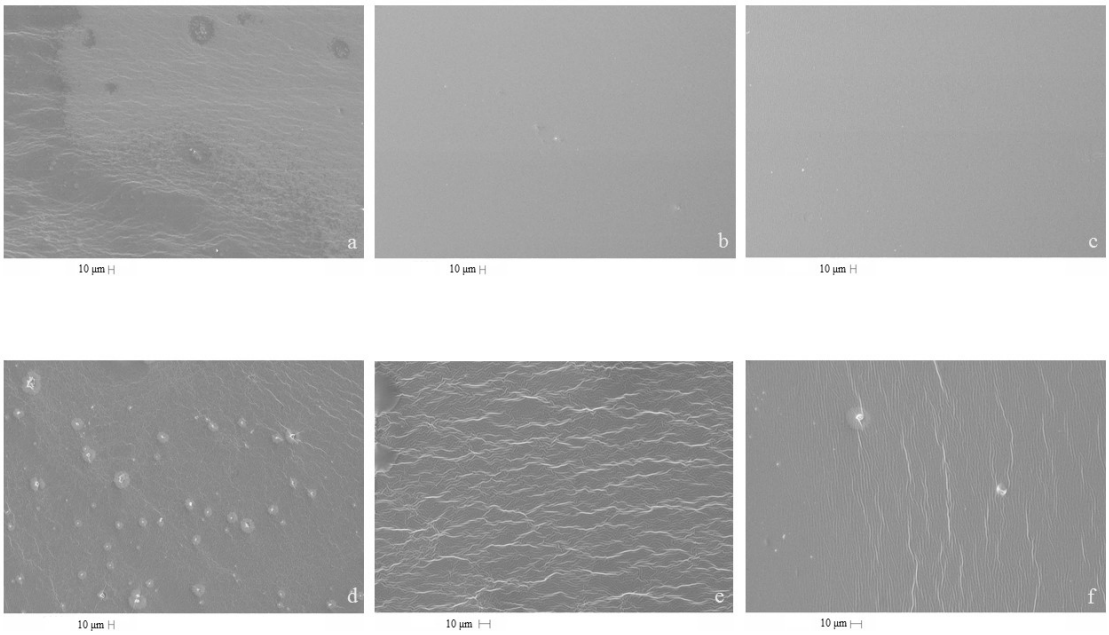

Figure 4.4 SEM micrographs of plasticized CHEuTrif$_n$, for n =0.00 (a), 0.05 (b), 0.10 (c), 0.15 (d), 0.20 (e) and 0.25 g (f).

4.3.2 Photoluminescent spectroscopy

Figures 4.5 and 4.6 present the emission and excitation spectra of the film samples with different quantities of $Eu(CF_3SO_3)_3$. In both set of spectra, the characteristic bands of Eu^{3+} are observed, with relatively high intensity, considering the small thickness of the films.

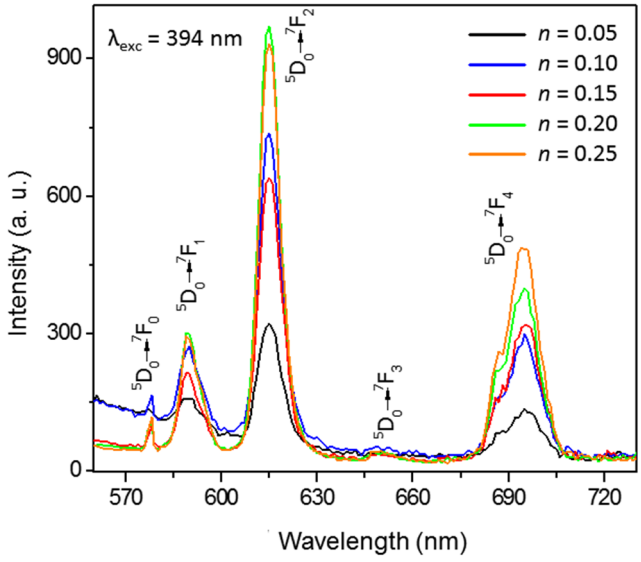

Figure 4.5 Emission spectra of CHEuTrif$_n$ film samples, obtained at room temperature, with excitation at 394 nm.

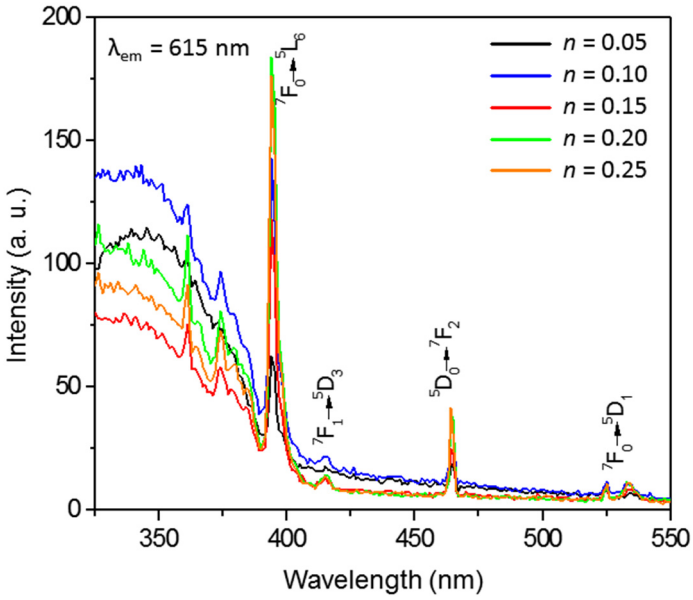

Figure 4.6 Excitation spectra of CHEuTrif$_n$ film samples, obtained at room temperature, monitoring the emission at 615 nm.

In the emission spectra, a broad emission, perceived for wavelengths shorter than 630 nm, in addition to the transitions from excited state $^5D_0$ to $^7F_{0-4}$, is attributed to the CH host polymer and, accordingly, it is more pronounced for the samples with lower concentration of Eu-triflate. A similar broad band was observed by Fernandes et al. [8] for poly(ε-caprolactone)/siloxane biohybrids containing Eu-triflate and likely attributed to the host. The fact that the $^5D_0 \rightarrow {}^7F_0$ emission transition is represented by only one peak evidences that Eu ions occupy a single site in the PE host. Moreover, the high intensity of the hypersensitive transition $^5D_0 \rightarrow {}^7F_2$, with respect to the magnetic dipole $^5D_0 \rightarrow {}^7F_2$ transition, indicates that such site is of low symmetry, without inversion center. When monitoring the emission at 615 nm, the excitation spectra display not only the lines corresponding to europium transitions, but also the host´s broadband excitation around 350 nm. Although this was to be expected, due to the overlap of ion and host emissions at 615 nm, the energy transfer from the host to the ion could as well be possible.

The assumptions are corroborated by examining the emission and excitation spectra of the CH sample with n = 0.00, that is, without the addition of Eu-triflate, Figure 4.7 (a) and (b), respectively. It is clearly noticed that both the emission and excitation bands are wavelength dependent, but the emission of the host does not extend to wavelengths longer than 650 nm.

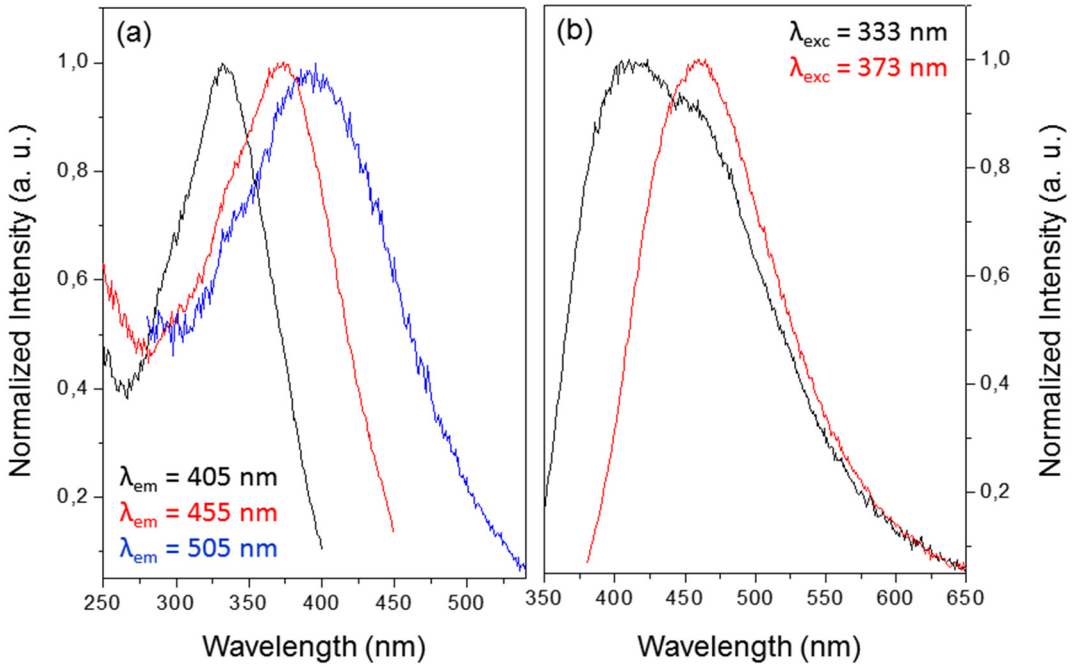

Figure 4.7 Excitation and emission spectra of the pure CH film, obtained at room temperature, with different emission and excitation wavelengths.

In luminescence decay curves of the CHEuTrif$_n$ film samples, obtained by monitoring the $^5D_0 \rightarrow {}^7F_2$ transition at 615 nm, are shown in Figure 4.8, along with the excited state $^5D_0$ average lifetime values τ. The latter were determined by fitting the decay curves with single exponential functions. The lifetime values range from 0.37 to 0.29 ms as a function of Eu-triflate amount. These values are higher than those observed for the poly(ε-caprolactone)/siloxane biohybrid films (maximum of 0.26 ms) [8], indicating that in the CH there is probably better dispersion of the ions. The small decrease of about 20% in τ values as the Eu-triflate amount increases almost by a factor 3 is attributed to some extent of energy transfer between the ions, followed by non-radiative decay, but the results are still considered to be very good.

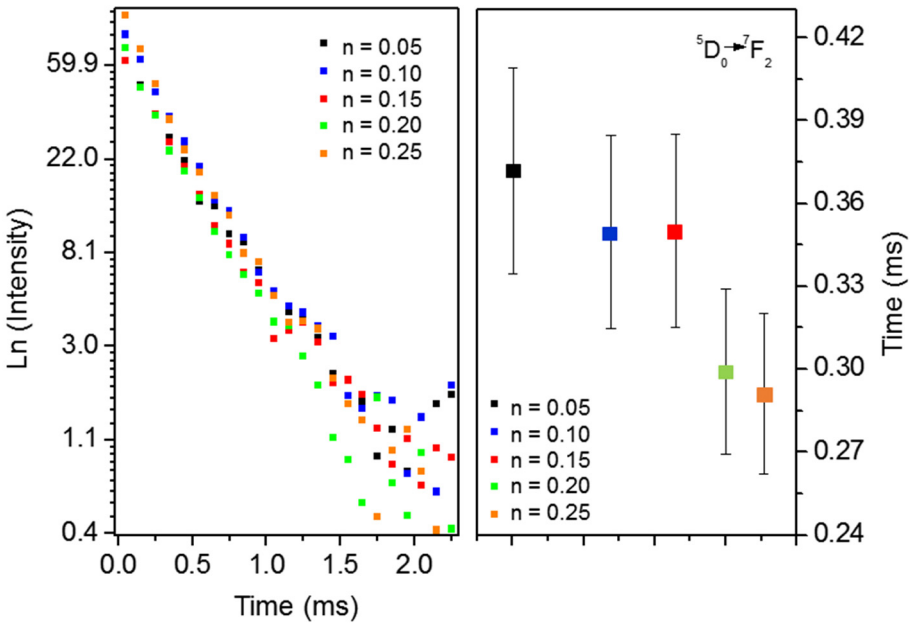

Figure 4.8 (a) Luminescence decay curves in time obtained by exciting the CHEu$_n$ film samples at 394 nm and monitoring the emission at 615 nm ($^5D_0 \rightarrow ^7F_2$ transition); (b) Excited state $^5D_0$ lifetime value determined by fitting the decay curves with single exponential functions.

4.4. Conclusion

The SPEs based on CH and $Eu(CF_3SO_3)_3$ were prepared by solvent casting technique. The X-ray analysis revealed a semi-crystalline structure with predominance of amorphous phase. With the results obtained by AFM and SEM analyses it was noted that the most conductive sample showed lower roughness and presented good surface uniformity. Photoluminescence studies indicated the characteristic emission and excitation transitions of Eu^{3+}. Based on the presence of a single peak for the $^5D_0 \rightarrow ^7F_0$ transition it was assumed that europium ions occupied a single, low symmetry site in the polymeric host, which was also corroborated by the intense emission at 615 nm ($^5D_0 \rightarrow ^7F_2$ transition). The excited state lifetime value $\tau \approx 0.3$ ms was similar to previously reported values for Eu^{3+} in polymer hybrid hosts.

4.5. References

[1] J.F. Du, Y. Bai, W.Y. Chu, L.J. Qiao, Synthesis and performance of proton conducting chitosan/NH_4Cl electrolyte, Journal of Polymer Science Part B: Polymer Physics, 48 (2010) 260-266.

[2] A. Pawlicka, F. Sentanin, A. Firmino, J.G. Grote, F. Kajzar, I. Rau, Ionically conducting DNA-based membranes for eletrochromic devices, Synthetic Metals, 161 (2011) 2329-2334.

[3] V. de Zea Bermudez, L.D. Carlos, M.C. Duarte, M.M. Silva, C.J.R. Silva, M.J. Smith, M. Assunção, L. Alcácer, A novel class of luminescent polymers obtained by the sol-gel approach, Journal of Alloys and Compounds, 275 (1998) 21-26.

[4] G. Binnig, C.F. Quate, Ch. Gerber, Atomic force microscope, Physical Review Letters, 56 (1986) 930.

[5] R. Alves, J.P. Donoso, C.J. Magon, I.D.A. Silva, A. Pawlicka, M.M. Silva, Solid polymer electrolytes based on chitosan and europium triflate, Journal of Non-Crystalline Solids, 432 (2016) 307-312.

[6] R. Leones, L.C. Rodrigues, M. Fernandes, R.A.S. Ferreira, I. Cesarino, A. Pawlicka, L.D. Carlos, V. de Zea Bermudez, M. Silva, Electro-optical properties of the DNA-Eu^{3+} bio-membranes, Journal of Electroanalytical Chemistry, 708 (2013) 116-123.

[7] E. Raphael, C.O. Avellaneda, B. Manzolli, A. Pawlicka, Agar-based films for application as polymer electrolytes, Electrochimica Acta, 55 (2010) 1455-1459.

[8] M. Fernandes, S.S. Nobre, L.C. Rodrigues, A. Gonçalves, R. Rego, M.C. Oliveira, R.A.S. Ferreira, E. Fortunato, M.M. Silva, L.D. Carlos, Li^{+}-and Eu^{3+}-doped poly(ε-caprolactone)/siloxane biohybrid electrolytes for electrochromic devices, ACS Applied Materials & Interfaces, 3 (2011) 2953-2965.

Chapter 5

Eco-friendly luminescent hybrid materials based on Eu^{III} and Li^{I} co-doped chitosan

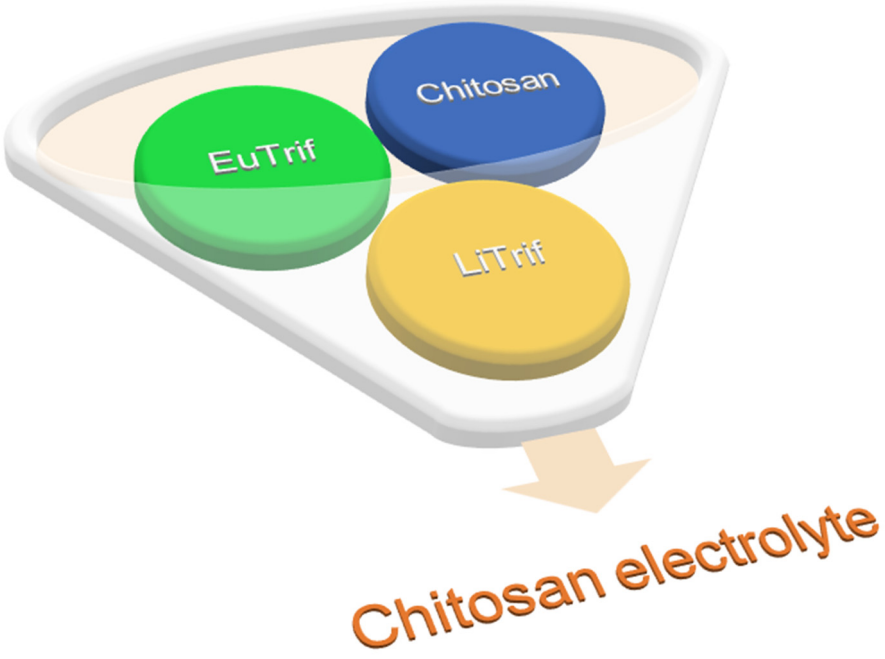

This chapter was adapted from: R. Alves, L. P. Ravaro, A. Pawlicka, M. M. Silva, A. S. S. de Camargo, Eco-Friendly Luminescent Hybrid Materials Based on Eu^{III} and Li^{I} Co-Doped Chitosan, Journal of the Brazilian Chemical Society 26 (2015) 2590-2597. (Invited paper)

5.1. Objective

The main objective of this chapter is perform a fundamental investigation of CH based luminescent materials doped with Eu^{III} and Li^{I} triflate salts, from the structural, photophysical and conducting points of view.

5.2. Experimental section

The electrolytes were prepared according to the procedure described in the chapter 2, and a photograph of a representative electrolyte film is presented in Figure 5.1. Samples have been represented by the notation $CHEu_nLi_m$, where *n* is the lanthanide salt mass and *m* is the lithium salt mass in the electrolytes and the thickness varied between 0.077 and 0.172 ± 0.001 mm (Table 5.1).

Figure 5.1 Photograph of a representative electrolyte film.

The morphology and structure were evaluated by XRD, and SEM. The total ionic conductivities were determined by impedance spectroscopy. The photoluminescence spectroscopy was used to evaluate the photophysical properties.

Table 5.1 Relevant details of the synthetic procedure of the $CHEu_nLi_m$ samples.

Sample	m $Eu(CF_3SO_3)_3$ (g) (±0.00001)	m $LiCF_3SO_3$ (g) (±0.00001)	Thickness (mm) (±0.001)
CH	-	-	0.145
$CHEu_{0.05}$	0.05037	-	0.130
$CHEu_{0.05}Li_{0.09}$	0.05090	0.09476	0.069
$CHEu_{0.05}Li_{0.2}$	0.05605	0.23535	0.159
$CHEu_{0.1}$	0.10270	-	0.109
$CHEu_{0.1}Li_{0.04}$	0.10197	0.04412	0.141
$CHEu_{0.1}Li_{0.05}$	0.10140	0.05237	0.107
$CHEu_{0.1}Li_{0.1}$	0.10546	0.10711	0.077
$CHEu_{0.25}$	0.25068	-	0.144
$CHEu_{0.25}Li_{0.05}$	0.25120	0.04707	0.170
$CHEu_{0.3}$	0.30040	-	0.172

5.3. Results and discussion

5.3.1 Structural and morphological characterization

Figure 5.2 depicts the X-ray diffraction patterns of film samples of $CHEu_nLi_m$, i.e., non-doped CH and its mixture with either $Eu(CF_3SO_3)_3$ or both $Eu(CF_3SO_3)_3$ and $LiCF_3SO_3$. The diffractograms of all samples, similarly to other ionic conducting membranes based on natural macromolecules, display a broad Gaussian band, centered at ca. 21º that can be assigned to CH crystal form type II [1-6]. For samples of $CHEu_{0.1}$ and $CHEu_{0.1}Li_{0.05}$ the same broad band is observed at 21º, similarly to DNA-Eu^{III} samples [7]. However, as observed in other studies, the doping of polymer matrices with inorganic salts can induce long range disorder in the diffraction patterns [8]. This observation strongly suggests that an increase of the amorphous content was promoted by the presence of salts. As a consequence of the increase of the amorphous content some regions of matrix become more crystalline. Although it seems contradictory, it might be explained as the increased disorder created by the salt among the neighboring CH chains forces chain segments, which are not located within the amorphous domain, to gather in well-defined regions and organize in a more regular manner. Similar behavior was also previously observed for PEs based on europium salt and PEO [9]. The PEs $CHEu_{0.1}Li_{0.04}$ and $CHEu_{0.1}Li_{0.1}$

exhibit Bragg peaks at 21º, similar to $CHEu_{0.1}$, $CHEu_{0.1}Li_{0.05}$ and non-doped CH matrix, and a very sharp lonely peak at 10º. CH powder presents two peaks at 2θ = 10.9 and 20.1º [10, 11]. The peak at about 10-11º of the $CHEu_{0.1}Li_{0.04}$ and $CHEu_{0.1}Li_{0.1}$ is much sharper than the peak of CH powder and resemble more the one found in free $LiCF_3SO_3$ or a polymer-salt crystalline complex. Nunes et al. [12] also detected a peak at about 10 - 11º for the system d-$U(2000)_nLiCF_3SO_3$, although this system presents a series of other peaks in salt rich domains. The position of these peaks coincides exactly with the location of the diffraction peaks of the crystalline complex with stoichiometry 3:1 that is formed between PEO and $LiCF_3SO_3$ [13]. The peak at 10º, in the present study, can be attributed to the sample or to some impurity. No peak was detected at approximately 29º, which, in the case of the system $U(2000)_nEu(CF_3SO_3)_3$, was ascribed to the diffraction of Eu-rich domains [14]. The obtained results prove that the addition of the guest europium triflate salt to CH matrix inhibits the formation of crystalline phases of free $Eu(CF_3SO_3)_3$ or CH/salt complexes.

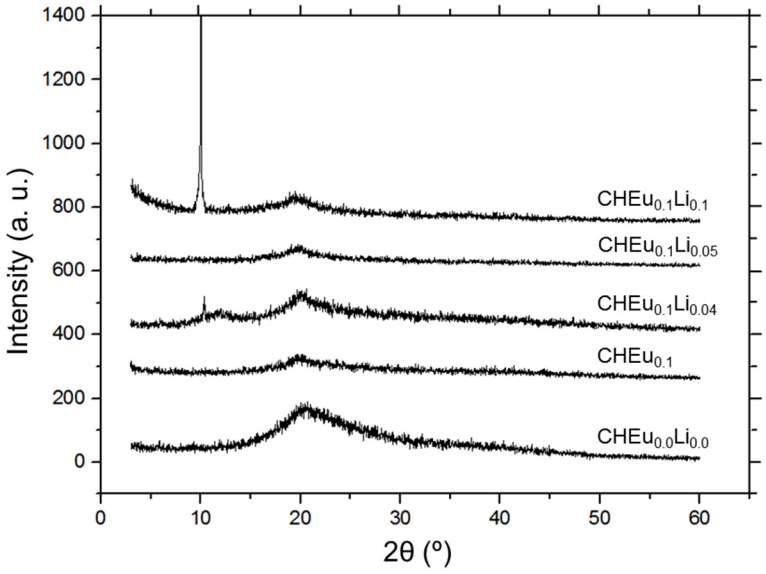

Figure 5.2 XRD patterns of $CHEu_nLi_m$ samples.

The amorphous nature of the CH based electrolyte system provides a clear advantage relative to other semi-crystalline systems, since the absence of crystallinity results in improvements in optical, mechanical and electrochemical behavior, especially because ionic movement occurs preferentially in the amorphous phase [15-17].

Scanning electron micrographs illustrating the morphology of CH and $Eu(CF_3SO_3)_3$ and $LiCF_3SO_3$ are shown in Figure 5.3. The good homogeneity without any phase separation and very good surface uniformity at the micrometer scale of samples containing 0.1 g of Eu^{III}-triflate (without Li^{I}) can be observed in the SEM micrographs in Figure 5.3 (a). Similar results were obtained for agar-based films [18]. Other SEM images reproduced in Figure 5.3 ((b), (c) and (d)) show that the samples containing mixture of both salts exhibit an irregular texture, and are very similar to the samples of SPE based on PEG with high $LiClO_4$ concentration [8]. The micrograph of $CHEu_{0.1}Li_{0.04}$ (Figure 5.3 (b)) shows a porous morphology evolving from large to lower pore size. It was verified that this is not a surface effect and it is explained because the degree of porosity is due to the low evaporation temperature of the solvent during the sample preparation. At the same time, the polymer chains show a reduced mobility, which hinder their occupation of the free space left by the evaporated solvent [19]. The images recorded for samples $CHEu_{0.1}Li_{0.05}$ and $CHEu_{0.1}Li_{0.1}$ reveal clearer lines that can be either related to undissolved or recrystallized salt, which confirms XRD data.

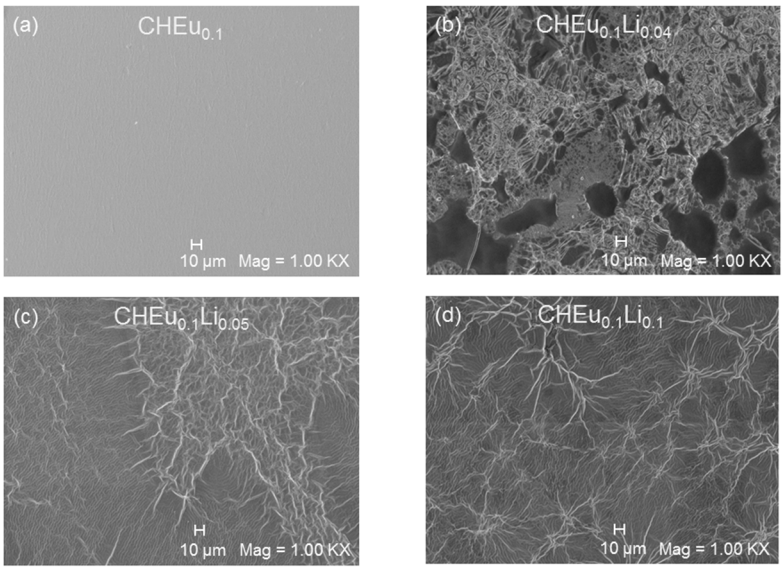

Figure 5.3 SEM micrographs of the $CHEu_nLi_m$ samples.

5.3.2 Ionic conductivity of electrolytes

The ionic conductivities of various electrolyte compositions over the temperature range from 20 to 90ºC, and as a function of salt content, are illustrated in Figure 5.4. These obtained results show a continuous variation in conductivity that is almost linear with respect to 1/T over a range of salt compositions. This plot demonstrates that all the doped

samples exhibit a typical behavior for PEs where hopping mechanism of ionic charge species is predominant. This behavior is similar to that exhibited by the same matrices doped with different salts [20-22] and contrasts with that of semi-crystalline materials based on commercial PEO host matrices [23]. The ionic conductivity (σ) values were calculated for each heating cycle using the equation (5.1):

$$\sigma = \frac{t}{A \times R_b} \tag{5.1}$$

where R_b is the bulk resistance, t is the thickness and A is the area of the sample. As shown in Figure 5.4 (fittings) the ionic conductivity temperature dependence follows the Arrhenius equation (5.2):

$$\sigma = \sigma_0 exp\left(\frac{-E_a}{RT}\right) \tag{5.2}$$

where σ_0 is the pre-exponential factor, E_a is the apparent activation energy for ion transport, R is the gas constant (8.314 J mol^{-1} K^{-1}) and T is the temperature. Table 5.2 and Figure 5.4 show the ionic conductivities (σ), and activation energy values (E_a), obtained from the above equations.

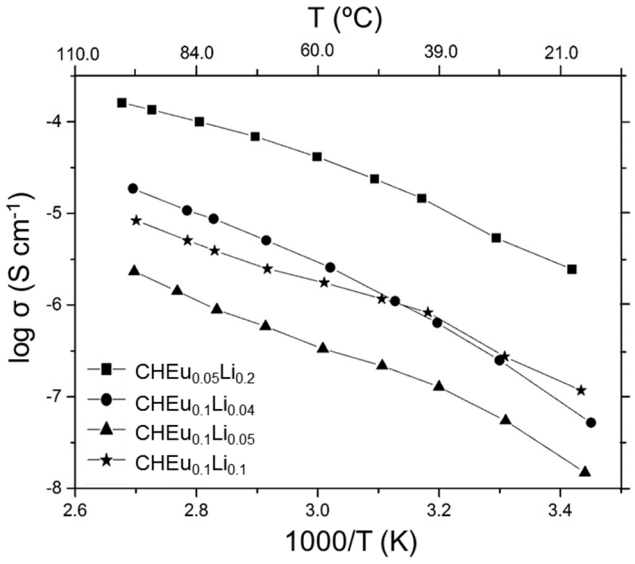

Figure 5.4 Conductivity plot of the CHEu$_n$Li$_m$ samples.

Table 5.2 Ionic conductivity and activation energy of the $CHEu_nLi_m$ samples.

Sample	σ (S cm^{-1})		E_a
	30ºC	80ºC	(kJ mol^{-1})
$CHEu_{0.3}$	$1.58x10^{-8}$	$3.33x10^{-6}$	92.17
$CHEu_{0.25}$	$1.56x10^{-6}$	$7.57x10^{-5}$	64.92
$CHEu_{0.25}Li_{0.05}$	$3.14x10^{-8}$	$4.47x10^{-6}$	84.11
$CHEu_{0.05}$	$1.74x10^{-7}$	$3.45x10^{-6}$	57.18
$CHEu_{0.05}Li_{0.09}$	$6.66x10^{-8}$	$1.04x10^{-6}$	46.56
$CHEu_{0.05}Li_{0.2}$	$5.38x10^{-6}$	$8.77x10^{-5}$	46.93
$CHEu_{0.1}$	$1.57x10^{-7}$	$1.73x10^{-5}$	74.38
$CHEu_{0.1}Li_{0.04}$	$1.79x10^{-7}$	$8.48x10^{-6}$	63.30
$CHEu_{0.1}Li_{0.05}$	$4.42x10^{-8}$	$9.07x10^{-7}$	52.81
$CHEu_{0.1}Li_{0.1}$	$2.32x10^{-7}$	$3.89x10^{-6}$	46.20

Over the whole range of studied temperatures, the sample with the highest ionic conductivity is the $CHEu_{0.05}Li_{0.2}$ with values of 5.38×10^{-6} and 8.77×10^{-5} S cm^{-1}, at 30 and 80ºC, respectively. These values are higher than those obtained for analogous polymer electrolytes incorporating europium salt [16] and very similar to those doped with lithium salts [24]. Besides temperature, ionic conductivity also depends strongly on the guest salt, both in type and concentration. Usually, increasing guest salt concentration results in an ionic conductivity increase, which is not at all observed in the present study. A high amount of $Eu(CF_3SO_3)_3$ can play opposite effects. Although the number of charge carriers increases with the increase of salt amount, a high concentration of salt leads to the decrease of free volume, as well as available coordination sites. Additionally, the influence of ion pairing should also be taken into account. The fitted E_a values of all the SPEs are depicted in Table 5.2, where one can observe that most of E_a values decrease with the increase of ionic conductivity. This behavior was normally expected, since the lower the energy barrier, the easier the ionic movement. This is probably due to the above given reason.

5.3.3 Photophysical properties

Figure 5.5 presents the photoluminescence emission spectra of the representative sample $CHEu_{0.3}$ measured with excitation at different wavelengths.

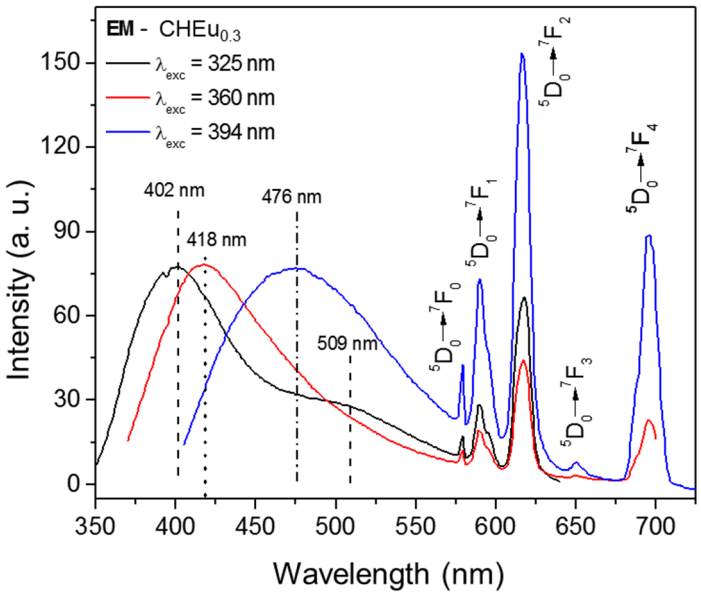

Figure 5.5 Emission spectra of the sample $CHEu_{0.30}$ with excitation at different wavelengths. The characteristic transitions of Eu^{3+} are indicated nearby the respective bands.

Besides the typical bands of Eu^{III} corresponding to transitions from the excited state $^5D_0$ to lower lying ^7F_J states, there is superimposed broad band whose energy in the blue-green spectral region is highly dependent on the chosen excitation wavelength. Similar broad bands have been observed for other bio-polymer hybrid electrolytes and their nature is attributed to the electron-hole recombination in the polymer host [25, 26]. At 360 and 394 nm there is concomitant excitation of the Eu^{III} ion and the host, however, at 325 nm (30769 cm^{-1}) only the host is excited (Eu^{III} does not have an energy level corresponding to this wavelength). Therefore, the fact that Eu^{III} emission is observed gives strong evidence of energy transfer from the host to the ion. This assumption is corroborated by examining the excitation spectrum in Figure 5.6, which was recorded by monitoring the europium emission at 616 nm. In this spectrum, not only the broad polymer band appears, suggesting once again the host → ion energy transfer, but one can also see why excitation at 394 nm is preferable in Eu^{III}-doped systems to achieve higher emission intensities as seen in Figure 5.5. Furthermore, in the spectra recorded with excitation at 325 and 360

nm, a small structure around 390 nm is observed and it corresponds to self-absorption by the ion. This peak has also been observed in Eu^{III}-based di-ureasil samples [27]. The fact that the $^5D_0 \rightarrow {}^7F_0$ transition band displays only one, well-defined peak, gives strong evidence that the Eu^{III} ion occupies a sole site of symmetry in the SPE samples. Moreover, the considerable intensity (as judged by naked eye) of the hypersensitive transition $^5D_0 \rightarrow {}^7F_2$ with respect to the purely magnetic dipole transition $^5D_0 \rightarrow {}^7F_1$ indicates that such site is of low symmetry, with no inversion center.

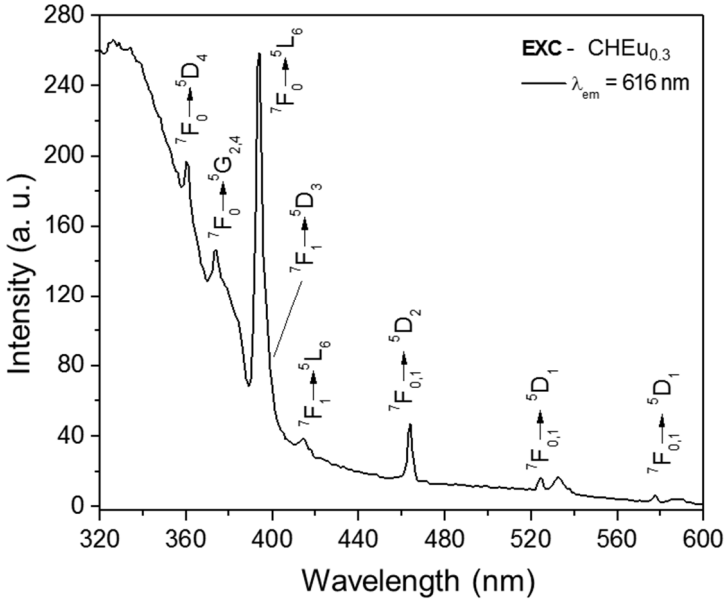

Figure 5.6 Excitation spectrum of the sample $CHEu_{0.3}$ measured by monitoring the emission at 616 nm. The characteristic transitions of Eu^{3+} are indicated by the respective bands.

The fact that the intense polymer emission accompanies that of Eu^{III}, even when excitation is done at 394 nm, suggests the combination of these bands to generate tunable visible (or white) light.

In Figure 5.7, a comparison of emission intensities and lineshapes is made for samples co-doped with Li^I. It comes out as no surprise that no changes of relative intensities and lineshapes of Eu^{III} bands, as a function of lithium concentration is observed. Still, a new functionality (PEs) is added and could potentially be combined with Eu^{III}-emission in a multifunctional material.

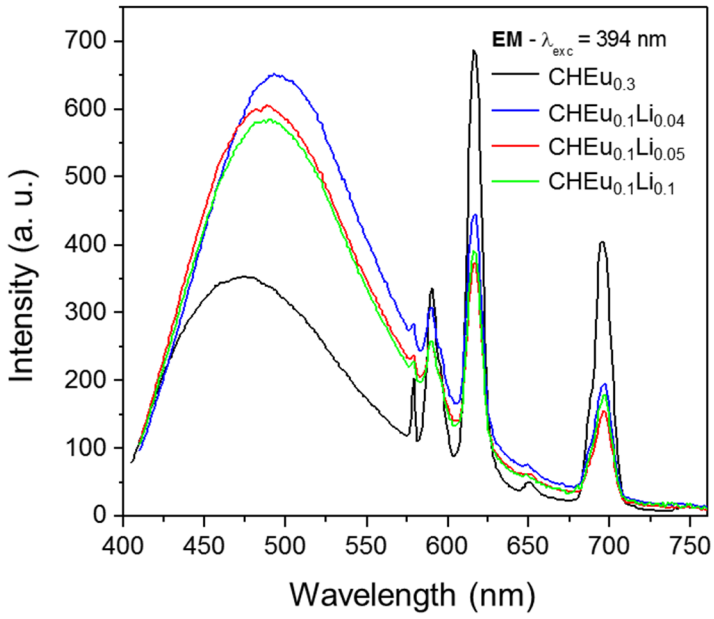

Figure 5.7 Comparison of emission spectra of samples doped with different amounts of $Eu(CF_3SO_3)_3$ and $LiCF_3SO_3$. All the spectra were measured with excitation at 394 nm.

In Figure 5.8, representative luminescence decay curves measured for the excited state $^5D_0$ by monitoring the emission at 616 nm ($^5D_0 \rightarrow {}^7F_2$) in different $CHEu_nLi_m$ samples are presented. The sample $CHEu_{0.3}$ was the only one to display nearly single-exponential decay. However, for the sake of comparison, averaged lifetime values were determined as the area below the curves corresponding to all samples, and also by assuming the value when intensities drop by a factor 1/e, yielding very similar results. The lifetime values for the samples containing lithium are slightly higher than for the sample, which does not contain this species. The values are in the range of those determined for Eu^{III}-doped agar (194 μs), DNA (528 μs), and for poly(ε-caprolactone)/siloxane biohybrids (225 and 262 μs) [25, 26]. In the latter case, the higher value also corresponds to a sample where the Li^I concentration is higher indicating that it can be positively interfering by decreasing the amount of hydroxyl ions in the first coordination sphere of the rare earth ion.

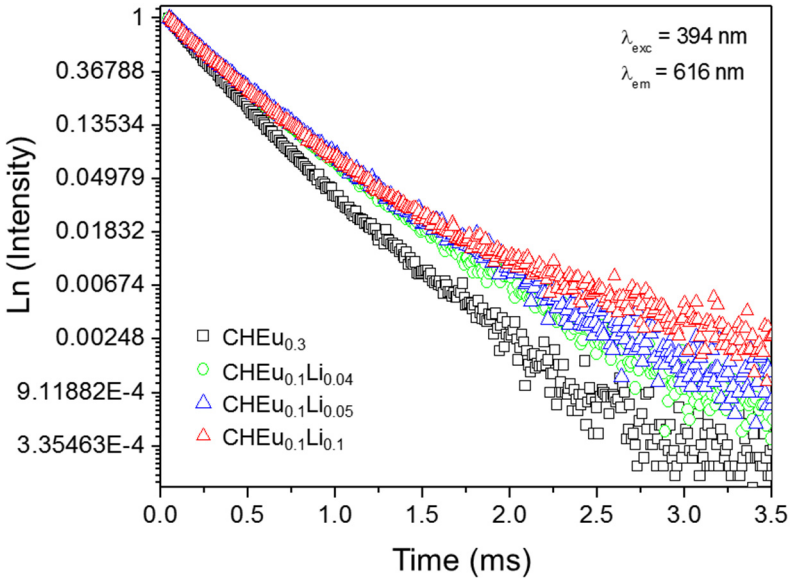

Figure 5.8 Fluorescence decay curves of $CHEu_{0.3}$ and $CHEu_{0.1}Li_m$ (m = 0.04, 0.05, 0.1 g) samples determined by single exponential fittings; λ_{exc} = 394 nm, λ_{em} = 616 nm.

By taking advantage of the concomitant emissions of polymer host and ion, and of the relative intensity variation depending on Eu^{III} concentration and excitation wavelength, the colour tuning [28] can be achieved as indicated in Figure 5.9.

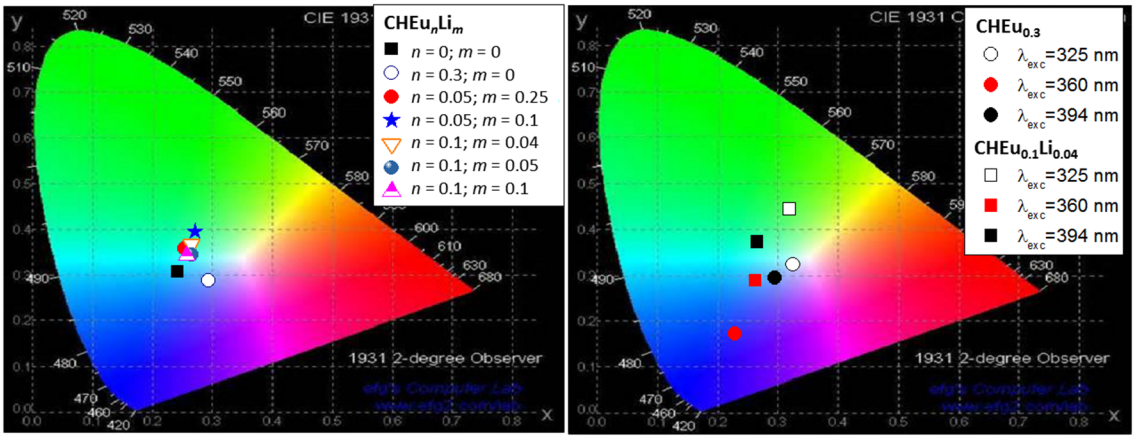

(a) (b)

Figure 5.9 CIE chromaticity diagrams showing the (x, y) color coordinates of emissions of $CHEu_mLi_n$ samples. (a) Dependence on Eu^{3+} and Li^+ relative concentrations, λ_{exc} = 394 nm; (b) Dependence on excitation wavelength for $CHEu_{0.3}$ sample.

In Figure 5.9 (a), the CIE chromaticity diagram presents the resultant colors for various $CHEu_mLi_n$ samples, where the $CHEu_{0.3}$ is closely placed at the crossing of $x = 0.3$ and $y = 0.3$ color coordinates of the CIE 1931 diagram, upon excitation at 325 nm (Figure 5.9 (b)). This sample is the closest one to the white in the diagram. The *x*- and *y*-chromaticity coordinates are presented in Table 5.3 for all the samples, together with the quantum yield values φ, measured in an integrating sphere. The maximum φ value around 2.7% is to be expected for Eu^{III} inserted in an environment where hydroxyl groups can act as efficient luminescence quenchers. Still, the values are comparable to other polymer doped hosts [29], and one possible way to increase efficiency would be to employ highly coordinated Eu^{III} complexes for which quantum yields can be as high as 85% [30].

Table 5.3 Experimental spectroscopic parameters of $CHEuLi_y$ samples (excited state $^5D_0$ lifetime τ, absolute quantum yields φ, CIE chromaticity coordinates (x and y)).

Sample	τ [$^5D_0$] (μs)	φ (± 0.05%)	CIE x-coordinate	CIE y-coordinate
CH	-	2.19	0.242	0.317
$CHEu_{0.3}$	274	1.80 (394 nm)	0.294	0.298
		2.10 (360 nm)	0.229	0.176
		0.57 (325 nm)	0.325	0.328
$CHEu_{0.05}Li_{0.1}$	341	2.24 (394 nm)	0.271	0.406
$CHEu_{0.05}Li_{0.25}$	340	2.66 (394 nm)	0.253	0.368
$CHEu_{0.1}Li_{0.04}$	344	2.40 (394 nm)	0.265	0.377
		0.32 (360 nm)	0.262	0.292
		0.71 (325 nm)	0.319	0.449
$CHEu_{0.1}Li_{0.05}$	355	2.22 (394 nm)	0.260	0.354
$CHEu_{0.1}Li_{0.1}$	351	2.30 (394 nm)	0.257	0.353

5.4. Conclusion

In this work a novel luminescent and ion conducting biohybrid electrolyte doped with $LiCF_3SO_3$ and $Eu(CF_3SO_3)_3$ by means of the solvent casting method was developed. The Gaussian-shaped broad X-ray diffraction band confirms the predominantly amorphous nature of the studied SPEs. Ionic conductivity values in the range 5.38×10^{-6} (30ºC) to 8.77×10^{-5} (80ºC) S cm^{-1} were measured, which are higher than those of analogous PEs singly doped with Eu^{III} salts, and very similar to those doped with lithium salts. Photophysical investigations indicate that by combining the emissions of the host matrix and the dopant Eu^{III} ion it is possible to tune the final emission color and ultimately generate white light. Except for a small increase in europium $^5D_0$ lifetime values (270 to ca. 350 μs), the presence of Li^I does not seem to interfere with the emissive properties, but offers the perspective of further developing and exploring these materials for multifunctional applications. The main benefit of this particular host-ions combination lies in the eco-friendly properties of the biodegradable and non-toxic host.

5.5. References

[1] N.A. Aziz, S.R. Majid, A.K. Arof, Synthesis and characterizations of phthaloyl chitosan-based polymer electrolytes, Journal of Non-Crystalline Solids, 358 (2012) 1581-1590.

[2] A. Pawlicka, F. Sentanin, A. Firmino, J.G. Grote, F. Kajzar, I. Rau, Ionically conducting DNA-based membranes for eletrochromic devices, Synthetic Metals, 161 (2011) 2329-2334.

[3] D.F. Vieira, A. Pawlicka, Optimization of performances of gelatin/$LiBF_4$-based polymer electrolytes by plasticizing effects, Electrochimica Acta, 55 (2010) 1489-1494.

[4] A.V. Yegorova, Y.V. Scripinets, A. Duerkop, A.A. Karasyov, V.P. Antonovich, O.S. Wolfbeis, Sensitive luminescent determination of DNA using the terbium (III)-difloxacin complex, Analytica Chimica Acta, 584 (2007) 260-267.

[5] B. Song, C.D.B. Vandevyver, E. Deiters, A.-S. Chauvin, I. Hemmilä, J.-C.G. Bünzli, A versatile method for quantification of DNA and PCR products based on time-resolved Eu III luminescence, Analyst, 133 (2008) 1749-1756.

[6] K. Ogawa, T. Yui, K. Okuyama, Three D structures of chitosan, International Journal of Biological Macromolecules, 34 (2004) 1-8.

[7] R. Leones, L.C. Rodrigues, M. Fernandes, R.A.S. Ferreira, I. Cesarino, A. Pawlicka, L.D. Carlos, V. de Zea Bermudez, M. Silva, Electro-optical properties of the DNA-Eu^{3+} bio-membranes, Journal of Electroanalytical Chemistry, 708 (2013) 116-123.

[8] T.J. Singh, S.V. Bhat, Morphology and conductivity studies of a new solid polymer electrolyte: $(PEG)_xLiClO_4$, Bulletin of Materials Science, 26 (2003) 707-714.

[9] M.J. Smith, C.J.R. Silva, Conductivity studies of a polymer electrolyte based on europium trifluoromethanesulphonate, Solid State Ionics, 58 (1992) 269-273.

[10] Y. Wan, K.A.M. Creber, B. Peppley, V.T. Bui, Synthesis, characterization and ionic conductive properties of phosphorylated chitosan membranes, Macromolecular Chemistry and Physics, 204 (2003) 850-858.

[11] A. Pawlicka, M. Danczuk, W. Wieczorek, E. Zygadło-Monikowska, Influence of plasticizer type on the properties of polymer electrolytes based on chitosan, The Journal of Physical Chemistry A, 112 (2008) 8888-8895.

[12] S.C. Nunes, V. de Zea Bermudez, D. Ostrovskii, M.M. Silva, S. Barros, M.J. Smith, L.D. Carlos, J. Rocha, E. Morales, Diurea cross-linked poly (oxyethylene)/siloxane ormolytes for lithium batteries, Journal of The Electrochemical Society, 152 (2005) A429-A438.

[13] P.G. Bruce, S.A. Campbell, P. Lightfoot, M.A. Mehta, Polymer electrolytes: structure and electrode processes, Solid State Ionics, 78 (1995) 191-198.

[14] V. de Zea Bermudez, L.D. Carlos, M.C. Duarte, M.M. Silva, C.J.R. Silva, M.J. Smith, M. Assunção, L. Alcácer, A novel class of luminescent polymers obtained by the sol-gel approach, Journal of Alloys and Compounds, 275 (1998) 21-26.

[15] R. Leones, F. Sentanin, L.C. Rodrigues, R.A.S. Ferreira, I.M. Marrucho, J.M.S.S. Esperança, A. Pawlicka, L.D. Carlos, M.M. Silva, Novel polymer electrolytes based on gelatin and ionic liquids, Optical Materials, 35 (2012) 187-195.

[16] R. Leones, F. Sentanin, L.C. Rodrigues, I.M. Marrucho, J.M.S.S. Esperança, A. Pawlicka, M.M. Silva, Investigation of polymer electrolytes based on agar and ionic liquids, Express Polymer Letters, 6 (2012) 1007-1016.

[17] F.M. Gray, Solid Polymer Electrolytes: Fundamentals and Technological Applications, Wiley-VCH, Weinheim, 1991.

[18] E. Raphael, C.O. Avellaneda, B. Manzolli, A. Pawlicka, Agar-based films for application as polymer electrolytes, Electrochimica Acta, 55 (2010) 1455-1459.

[19] X. Wang, L. Zhang, D. Sun, Q. An, H. Chen, Formation mechanism and crystallization of poly (vinylidene fluoride) membrane via immersion precipitation method, Desalination, 236 (2009) 170-178.

[20] P. Barbosa, L. Rodrigues, M. Silva, M. Smith, A. Gonçalves, E. Fortunato, Application of di-ureasil ormolytes based on lithium tetrafluoroborate in solid-state electrochromic displays, Journal of Materials Chemistry, 20 (2010) 723-730.

[21] S.M.G. Correia, V. de Zea Bermudez, M.M. Silva, S. Barros, R.A.S. Ferreira, L.D. Carlos, M.J. Smith, Short chain U(600) di-urea cross-linked poly(oxyethylene)/siloxane ormolytes doped with lanthanum triflate salt, Electrochimica acta, 47 (2002) 2551-2555.

[22] M.M. Silva, V. de Zea Bermudez, L.D. Carlos, A.P.P. de Almeida, M.J. Smith, Sol-gel processing and structural study of europium-doped hybrid materials, Journal of Materials Chemistry, 9 (1999) 1735-1740.

[23] M. Armand, Charge Transfer at polymer electrolytes, Faraday Discussions of the Chemical Society, 88 (1989) 65-76.

[24] S.C. Nunes, V. de Zea Bermudez, M.M. Silva, M.J. Smith, E. Morales, L.D. Carlos, R.A.S. Ferreira, J. Rocha, Sol-gel derived Li^{+}-doped poly(ε-caprolactone)/siloxane biohybrid electrolytes, Journal of Solid State Electrochemistry, 10 (2006) 203-210.

[25] R. Leones, M. Fernandes, R.A.S. Ferreira, I. Cesarino, J.F. Lima, L.D. Carlos, V. de Zea Bermudez, C.J. Magon, J.P. Donoso, M. Silva, Luminescent DNA-and agar-based membranes, Journal of Nanoscience and Nanotechnology, 14 (2014) 6685-6691.

[26] M. Fernandes, S.S. Nobre, L.C. Rodrigues, A. Gonçalves, R. Rego, M.C. Oliveira, R.A.S. Ferreira, E. Fortunato, M.M. Silva, L. Carlos, Li^{+}-and Eu^{3+}-doped poly(ε-caprolactone)/siloxane biohybrid electrolytes for electrochromic devices, ACS Applied Materials & Interfaces, 3 (2011) 2953-2965.

[27] M.C. Goncalves, V. de Zea Bermudez, R. Sá Ferreira, L.D. Carlos, D. Ostrovskii, J. Rocha, Optically functional di-urethanesil nanohybrids containing Eu^{3+} ions, Chemistry of Materials, 16 (2004) 2530-2543.

[28] L.D. Carlos, Y. Messaddeq, H.F. Brito, R.A. Sá Ferreira, V. de Zea Bermudez, S.J.L. Ribeiro, Full-Color Phosphors from Europium (III)-Based Organosilicates, Advanced Materials, 12 (2000) 594-598.

[29] R.A. Sá Ferreira, L.D. Carlos, R.R. Gonçalves, S.J.L. Ribeiro, V. de Zea Bermudez, Energy-transfer mechanisms and emission quantum yields in Eu^{3+}-based siloxane-poly (oxyethylene) nanohybrids, Chemistry of Materials, 13 (2001) 2991-2998.

[30] O. Moudam, B.C. Rowan, M. Alamiry, P. Richardson, B.S. Richards, A.C. Jones, N. Robertson, Europium complexes with high total photoluminescence quantum yields in solution and in PMMA, Chemical Communications, 43 (2009) 6649-6651.

Chapter 6

Binary Ce(III) and Li(I) triflates salt composition for solid polymer electrolytes

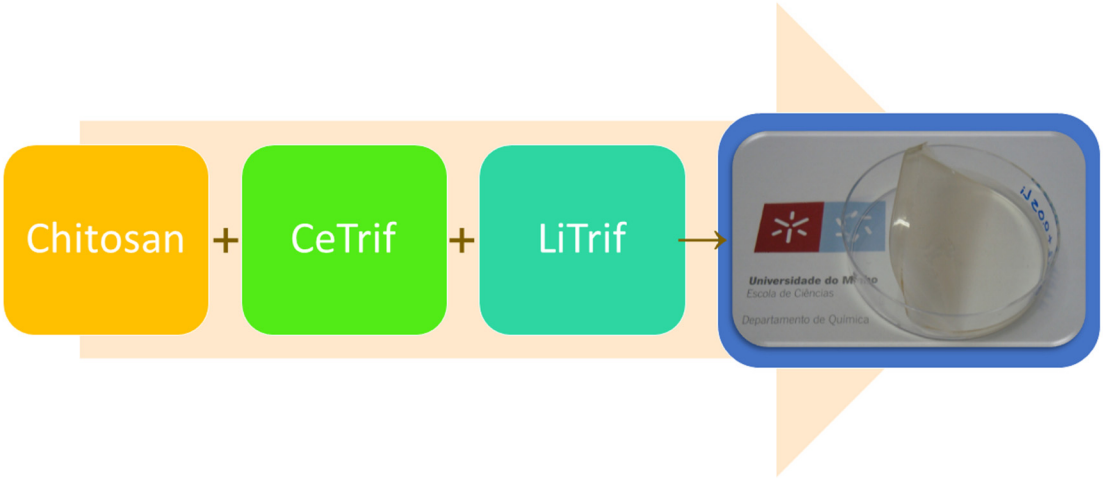

This chapter was adapted from: R. Alves, R. C. Sabadini, I. D. A. Silva, J. P. Donoso, C. J. Magon, A. Pawlicka, M. M. Silva, Binary Ce(III) and Li(I) triflates salt composition for solid polymer electrolytes, Ionics, (2017) 1-14. https://doi.org/10.1007/s11581-017-2355-8.

6.1. Objective

The main objective of this chapter is the characterization of SPEs using CH matrix plasticized with glycerol and doped with cerium and lithium triflates binary salt composition.

6.2. Experimental section

The SPEs were synthesized according to the method described previously in the chapter 2. Samples were represented by the notation $CHCe_nLi_m$, where *n* and *m* are the mass of cerium and lithium triflate, respectively. The electrolyte membranes, shown in Figure 6.1, were transparent, and their thicknesses ranged between 0.045 and 0.180 ± 0.001 mm.

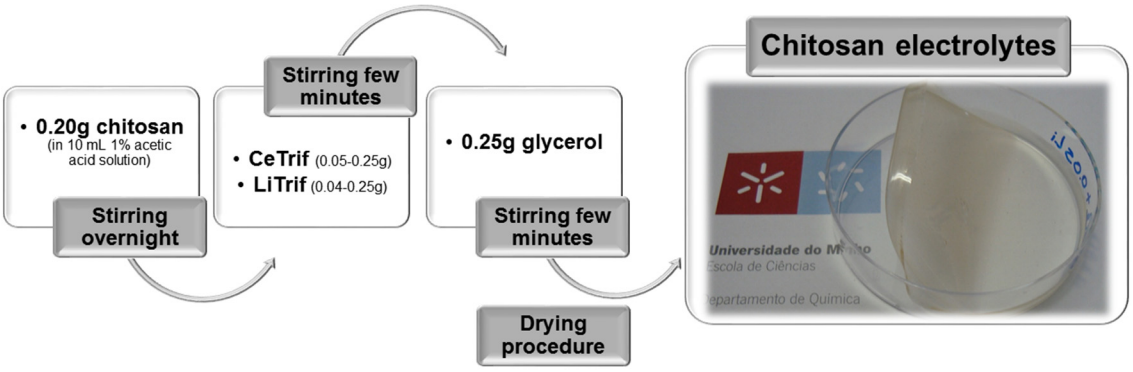

Figure 6.1 Diagram of CH-based electrolytes synthesis and physical appearance of the samples.

The thermal behavior was studied by TGA and DSC. The morphology and structure was evaluated by XRD, SEM and AFM. Complex impedance spectroscopy was used to make the conductivity measurements. Finally, the EPR analysis was used to evaluate the local coordination environment of the paramagnetic ions.

6.3. Results and discussion

6.3.1. Thermal characterization (TGA and DSC)

TGA is an effective tool for identification on the thermal stability and the thermograms of the samples are presented in Figure 6.2 (a-c). The obtained results reveal that for all the electrolytes the degradation process occurs in three stages. For pure CH membrane the degradation occurs in two stages, and it was thermally stable up to 265ºC [1]. In an early study with cerium triflate, the sample of CH matrix also presented two degradation stages, but when salt is added the decomposition occurs in three stages that started in the interval of 128 and 143ºC [2]. In a study of CH-NH_4NO_3-EC membrane the authors obtained two-stage decomposition [3]. The first one corresponds to desorption process, which occurs at 50 - 100ºC and has a weight loss of about 15%. This first stage is followed by a total decomposition that occurs in between 150 and 200ºC with 60% of the weight loss. The total decomposition began at 174ºC, which is a relatively lower value when compared with most pure CH membranes where the total decomposition occurs at 200ºC, and this difference is probably due to the presence of EC plasticizer. In the case of this study, the addition of lithium salt to cerium electrolytes does not cause significant changes in the thermograms aspect, and the degradation process of these samples also occurs in three stages. The curves of the samples with and without lithium triflate in Figure 6.2 (b1) are practically overlapped, and the main difference is the remaining residue that is higher in lithium-free sample. In relation to the degradation temperature, the addition of lithium makes the samples more stable in almost all cases as shown by the degradation temperature graphs present in Figure 6.2 (a2), (b2) and (c2). In samples containing two salts, the degradation started in the interval of 136 - 153ºC, which is a relatively higher temperature range than that obtained for samples containing only cerium triflate. In both samples, with and without lithium, the decomposition occurs below 200ºC, which is probably due to the presence of glycerol as plasticizer. The second stage occurred between 200 - 300ºC, and the degradation process ended at about 500ºC; however, the weight loss continued slowly as the temperature was increased up to 900ºC. The predominant stage of thermal degradation was caused probably by depolymerization of CH chains. The fact that degradation occurs in three stages may be due to the different interactions of the salts and the plasticizer with polysaccharide chains [2]. The remaining residues were in the range of 24 - 30% for the samples without and 11 - 18% with lithium triflate in the electrolytes composition.

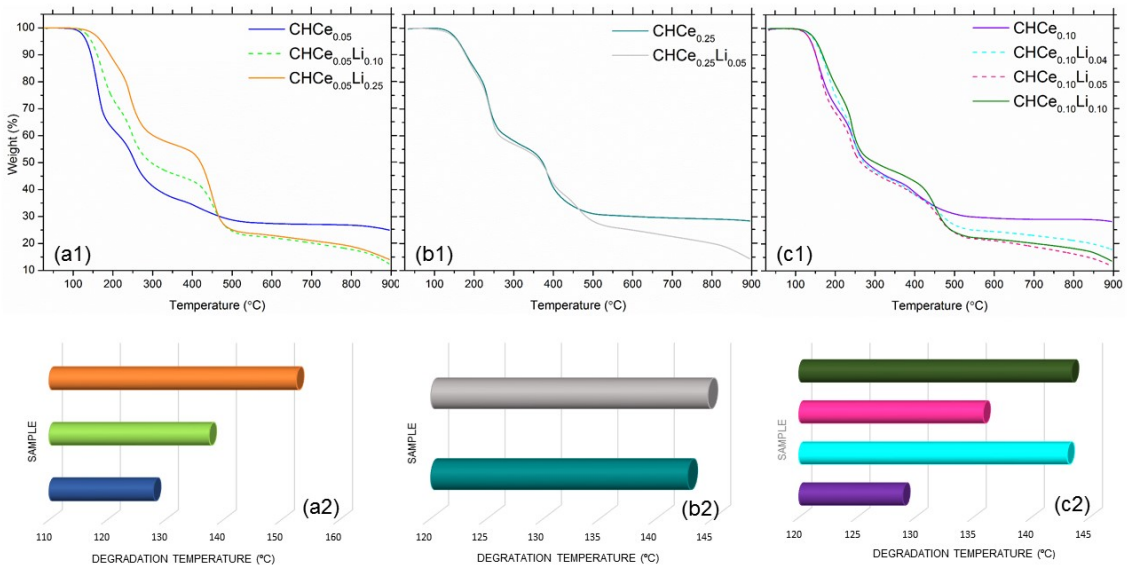

Figure 6.2 TGA and degradation temperatures of CHCe$_n$Li$_m$ electrolytes.

The DSC results of CHCe$_n$Li$_m$ based electrolytes are shown in Figure 6.3. The DSC measurements were performed in the -60 to 200ºC temperature interval, and no glass transition temperature was detected within this range, so their semi-crystalline nature was confirmed. This behavior is very similar to that obtained with other natural polymer ionically conducting membranes [4, 5]. Although samples have predominantly amorphous character, they presented some peaks that appear at about 175ºC in most of the samples containing cerium triflate, which may be due to the presence of the crystalline domains. These peaks can be related to undissolved salt or a complex formation between the matrix and the salt. Some samples also presented a weak and large endothermic peak, which can be attributed to acetal crosslinking break. As found for other samples, this crosslinking break is due to the catalytic properties of acetic acid residues in the electrolytes [6].

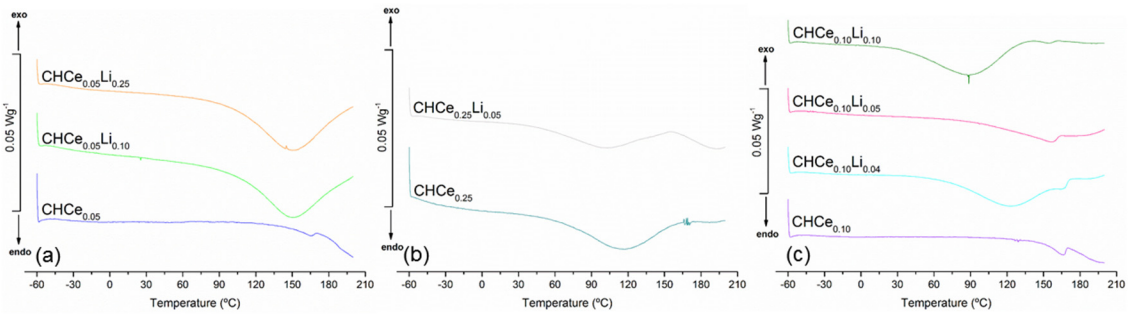

Figure 6.3 DSC curves of CHCe$_n$Li$_m$ electrolytes.

6.3.2. Impedance analysis

Figure 6.4 (a-c) shows a typical impedance plots of CHCe$_{0.05}$Li$_m$ prepared with 0.05 g of cerium triflate and different quantities of lithium triflate, and measured at various temperatures. The impedance plots show a semicircle at high frequencies and a spike at low frequencies. In this figure, one can also observe a disappearance of a depressed semicircle at high frequency with the increase in temperature, which reveals the absence of capacitive nature and just diffusion process [7]. At low frequencies, information about the electrode/electrolyte interface is obtained, and if the interaction is ideal vertical spikes are observed [8]. In present and other studies, the spike is inclined at an angle less than 90º, and may be due to the roughness or non-homogeneous of the electrode/electrolyte interface [9].

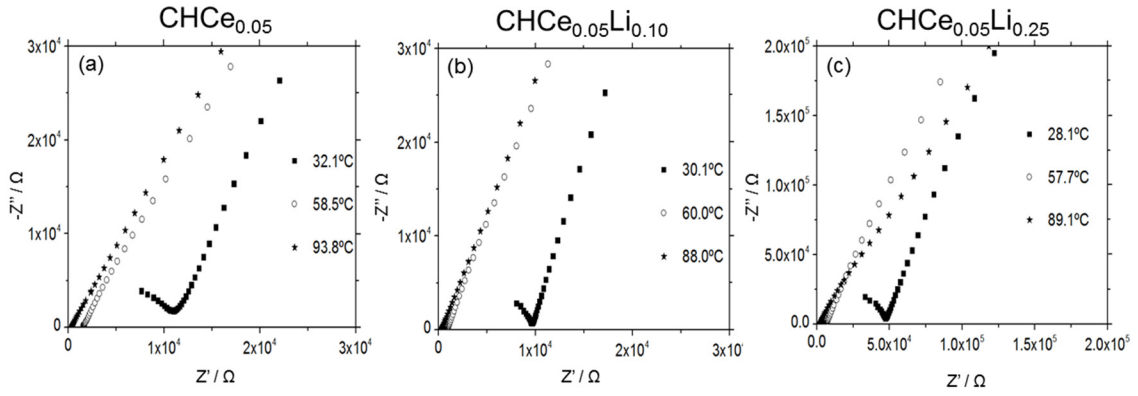

Figure 6.4 Complex impedance plots of CHCe$_{0.05}$Li$_m$, measured at different temperatures.

The ionic conductivity values can be obtained using the equation (6.1):

$$\sigma = \frac{t}{A \times R_b} \tag{6.1}$$

where t is the thickness of sample, R_b is the bulk resistance, and A is the contact area between the electrolyte and the electrode. The R_b values were calculated from the intercept of the semicircle or the intercept of the spike with the real axis. The bulk resistance values plotted in Figure 6.4 decrease with the increase of the temperature indicating an increase of the ions mobility and the thermal movement of polymer chains [10]. The R_b values are higher for lower conductivity values, but an increase in salt concentration increases the number of mobile charge carriers, which leads to the decrease in R_b values. However, the salt excess leads to the recombination of ions, a decrease in the amorphousness and, consequently, an increase in R_b values and a decrease in ionic conductivity.

The evolution of the ionic conductivity as a function of temperature is shown in Figure 6.5. The ionic conductivity depends on factors such as salt concentration and temperature [11]. The higher conductivity value obtained in this work shows that the ionic conductivity can be increased by using a mixture of salts. The best ionic conductivity values were obtained for the samples with the same total amount of salt of 0.15 g. Thus, $CHCe_{0.05}Li_{0.10}$ and $CHCe_{0.10}Li_{0.05}$ are the samples with higher, but still modest, conductivity values, namely 2.63×10^{-6} and 2.28×10^{-6} S cm^{-1} at 30ºC. At higher temperatures, thermal movement of polymer chain segments and dissociation of salts would be improved, which results in an increase of the conductivity, and values of 9.63×10^{-5} and 5.84×10^{-5} S cm^{-1} were obtained at 90ºC for the samples referred above. The difference in conductivity values may also be attributed to the different ratio of CeTrif-LiTrif used in the present work. In the case of the $CHCe_{0.05}Li_{0.10}$ the incorporation of lithium triflate enhances the room temperature ionic conductivity by one order of magnitude, which may be attributed to the contribution of Li^+ ions. The effect of the addition of LiTrif in SPEs was also evaluated in another study, where the authors obtained a greater increase of three to four orders of magnitude in conductivity values at room temperature [12]. The ionic conductivity increases with the increase in total salts amount

to reach a maximum, and this is probably due to the increase in the number of mobile charge carriers. However, for higher salt levels a decrease in the conductivity values is certainly related to undissolved or recrystallized salt. On the other hand, at higher salt levels, the ions are able to recombine and form neutral ion pairs leading to a decrease in the number density of mobile ions and a decrease in the ionic conductivity [13].

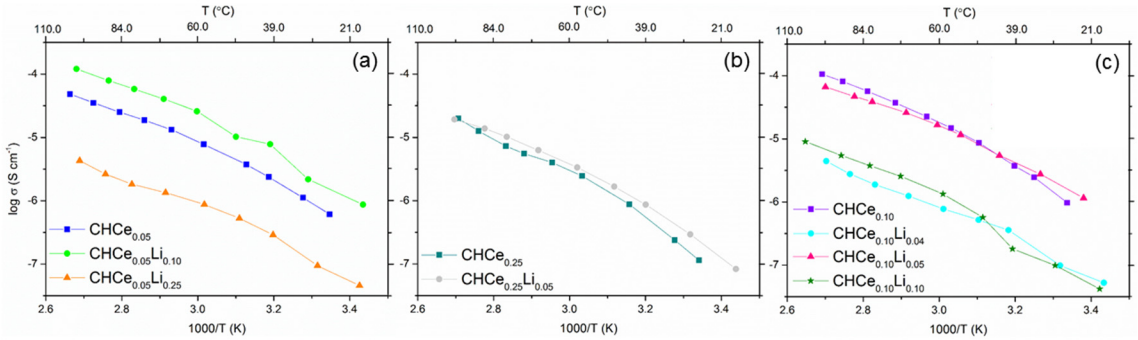

Figure 6.5 Conductivity plots of $CHCe_nLi_m$-based electrolytes as a function of inverse of temperature.

From the temperature dependence of ionic conductivity is possible to deduce that practically all samples displayed almost linear ($r^2 \sim 1$) relationship of log σ vs 1000/T. This indicates that the ionic conductivity is thermally activated and the plots obey the Arrhenius equation (6.2):

$$\sigma = \sigma_0 exp\left(\frac{-E_a}{RT}\right) \qquad (6.2)$$

where σ_0 is a pre-exponential factor, E_a is the activation energy for ion transport, R is the gas constant (8.314 J mol^{-1} K^{-1}), and T is the temperature. The E_a value was calculated using the slope of the fittings of obtained data from Arrhenius equation (6.2). For the electrolyte $CHCe_{0.10}Li_{0.05}$ the E_a value is 49.45 kJ mol^{-1}, a very similar value to that obtained in a study using other natural polymer as host [14].

6.3.3. X-ray diffraction analyses

The XRD analysis is a useful tool to determine the structure and crystallization of the polymer matrices [14]. XRD analysis has been performed in order to investigate the effected of the mixed salts in the system, and the respective diffraction patterns of the samples $CHCe_nLi_m$ are shown in Figure 6.6 (a-c). Figure 6.6 reveals that all the samples presented a peak at 2θ = 10º, which may be attributed to the cerium triflate salt as previously demonstrated in another study [2]. On the other hand, the incorporation of lithium triflate makes some samples more crystalline as in the case of $CHCe_{0.05}Li_{0.25}$ and $CHCe_{0.10}Li_{0.04}$. The new peaks that appear in XRD data of these samples are certainly related to the diffraction of salt domains. In a study of $U(600)_nLiCF_3SO_3$ xerogels, some samples also present new peaks with lithium addition, namely at approximately 34º, which are also related with Li^+-domains [15]. The XRD obtained results corroborate with conductivity results since the samples with the presence of crystalline domains, namely $CHCe_{0.05}Li_{0.25}$, $CHCe_{0.25}$, and $CHCe_{0.10}Li_{0.04}$ are also those with less conductivity. On the other side, the samples with similar XRD patterns, $CHCe_{0.10}$ and $CHCe_{0.10}Li_{0.05}$, also present very similar conductivity values.

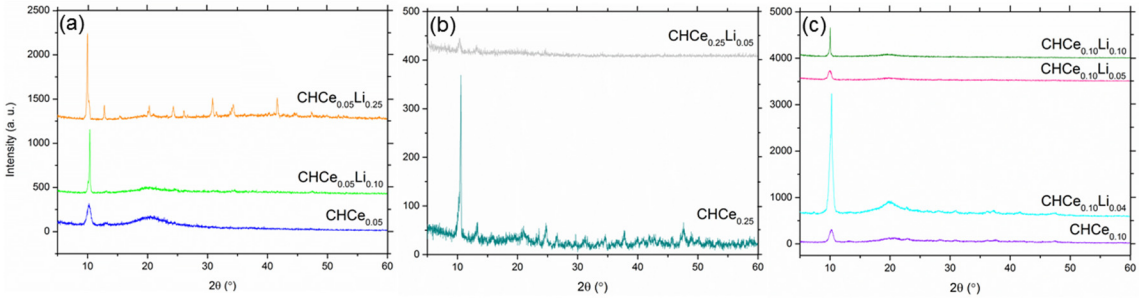

Figure 6.6 XRD diffractions of $CHCe_nLi_m$ -based electrolytes.

6.3.4. Scanning Electron Microscopy analyses

Figure 6.7 shows the SEM micrographs of the polymer electrolytes films containing only one salt (cerium triflate) and a mixture of two salts (cerium and lithium triflate).

As shown in Figure 6.7 (a1), (b1), and (c1) for the samples without lithium triflate the surface morphologies are very similar to those obtained with other natural polymers [16, 17]. Also in this case, the electrolytes present a uniform surface morphology without any phase separation.

The samples containing a binary system of two salts have less homogeneous surfaces, which is clear in the remaining images of Figure 6.7.

Figure 6.7 (a) shows the results of the samples with the same cerium amount of 0.05 g and varied quantity of lithium salt of 0.10 and 0.25 g. As already seen above, the addition of 0.10 g of lithium triflate made the samples more conductive (Figure 6.5 (a)) probably due to the presence of lithium ions. On the other hand, when a large amount of lithium is added, in this case 0.25 g, the ionic conductivity decreases probably due to undissolved or recrystallized salt, which justifies the clearer lines in SEM images (Figure 6.7 (a3)) and crystalline peaks in XRD (Figure 6.6 (a)).

In Figure 6.7 (b) are presented the SEM micrographs of samples with 0.25 g of cerium triflate and different quantities of lithium triflate. The addition of a small amount of lithium salt (0.05 g) results in a less regular structure and in a more conductive sample. At low magnification, Figure 6.7 (b2.1) and (b2.2), a granular structure is observed. In Figure 6.7 (b2) it is seen that some crystalline aggregates are adjacent taking shape of a semi-crystalline morphology, which corroborates XRD data (Figure 6.6 (b)). In a study of blends with different mass ratios of PMMA/PVdF the SEM images at different magnifications revealed a granular structure at low magnification [18]. The extreme PMMA/PVdF compositions of 80/20 and 30/70 are more amorphous and crystalline structures, respectively. In 60/40 blend ratio the samples have semi-crystalline morphology because PVdF crystalline aggregates are adjacent.

When lithium triflate is added to CH-based samples with fixed 0.10 g of cerium triflate the resulting SEM images are presented in Figure 6.7 (c). The first increment of lithium (0.04 g) results in a poorly conductive sample, which can be explained by recrystallized or undissolved salt. This is confirmed by the peaks observed in XRD data (Figure 6.6 (c)) and the irregular surface presented in SEM micrograph (Figure 6.7 (c2)). Also in the case of higher lithium amounts (0.10 g), although the samples show a porous morphology (Figure 6.7 (c4)), the conductivity is close to that obtained for 0.04 g of lithium salt and again it may be due to undissolved salt. The increments of 0.05 g of lithium salt in DSC and XRD investigations suggests a lower degree of crystallinity and predominance of the amorphous phase, which results in a higher value of ionic conductivity.

All the prepared samples also appeared translucent and showed very good adhesion properties.

6.3.5. Atomic Force Microscopy analysis

Aiming to evaluate the homogeneity and changes in the surface topography of the electrolytes the AFM analyses were carried out. Therefore, morphological characteristics of CH doped with one salt (cerium triflate) and two salts (cerium and lithium triflate) were examined by AFM, and Figure 6.8 displays characteristic images of these samples. The scanning area of 2.00 μm x 2.00 μm and the roughness, expressed in roughness mean square (RMS) of CH electrolytes, are presented in Figure 6.8. In the case of the samples containing 0.05 g of cerium triflate and different quantities of lithium triflate, Figure 6.8 (a), the RMS varies between 7.10 and 124 nm. The more conductive sample ($CHCe_{0.05}Li_{0.10}$) presented smaller roughness of 7.10 nm, while the less conductive sample ($CHCe_{0.05}Li_{0.25}$) showed higher roughness of 124 nm. From these results it was stated that the most conductive sample exhibits a lower surface roughness value, and the same remarks were done for samples of CH doped with europium triflate [19]. For the samples with 0.25 g of cerium triflate and different quantities of lithium triflate, the AFM results are presented in Figure 6.8 (b). Similarly to conductivity results also in this case the roughness values are very close each other. The RMS values varies between 8.43 and 10.2 nm, and the most conductive sample ($CHCe_{0.25}Li_{0.05}$) exhibits a higher surface roughness of 10.2 nm. This behavior is opposite to those referred in the literature for samples with chitosan doped with cerium triflate [2].

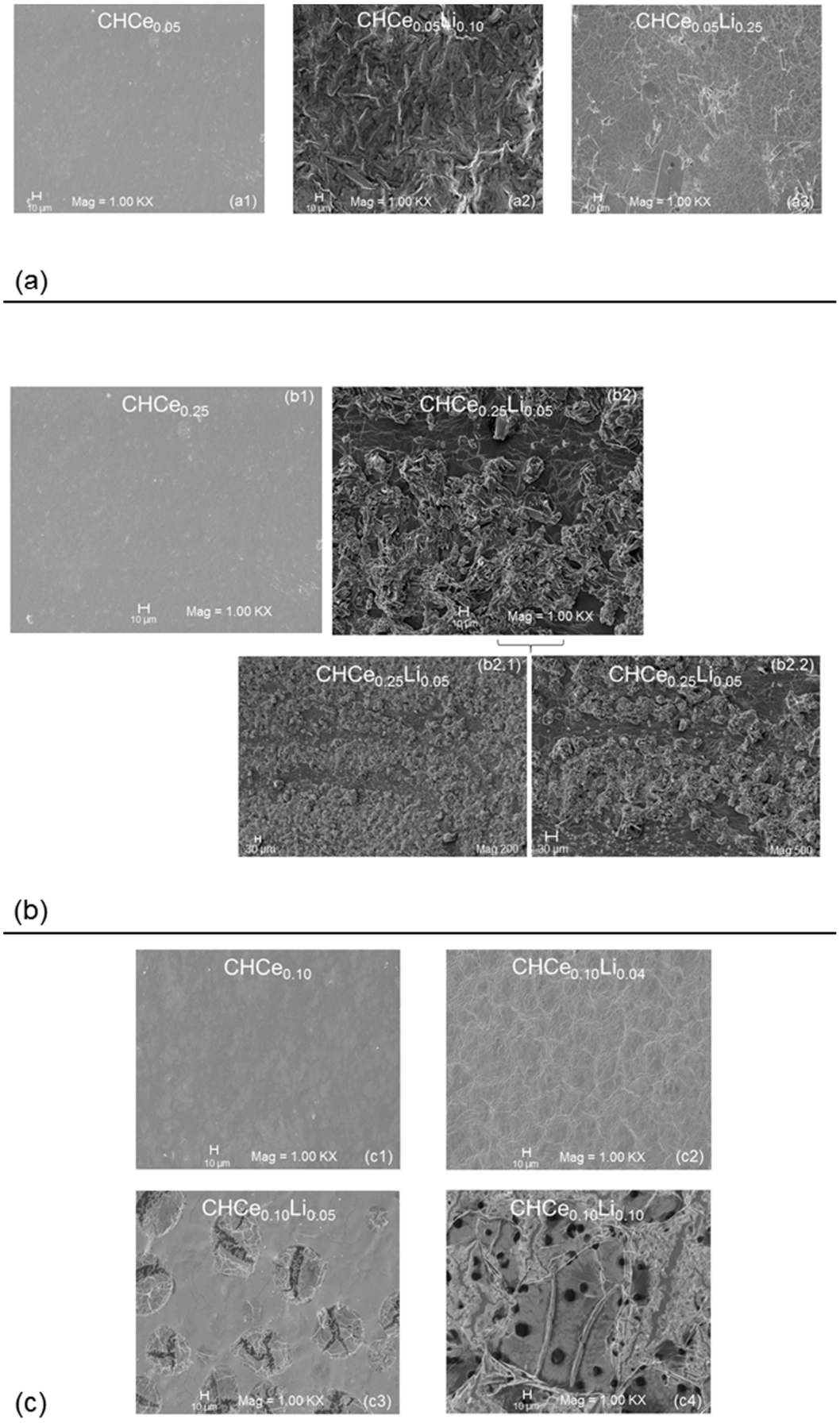

Figure 6.7 SEM micrographs of $CHCe_nLi_m$ -based electrolytes.

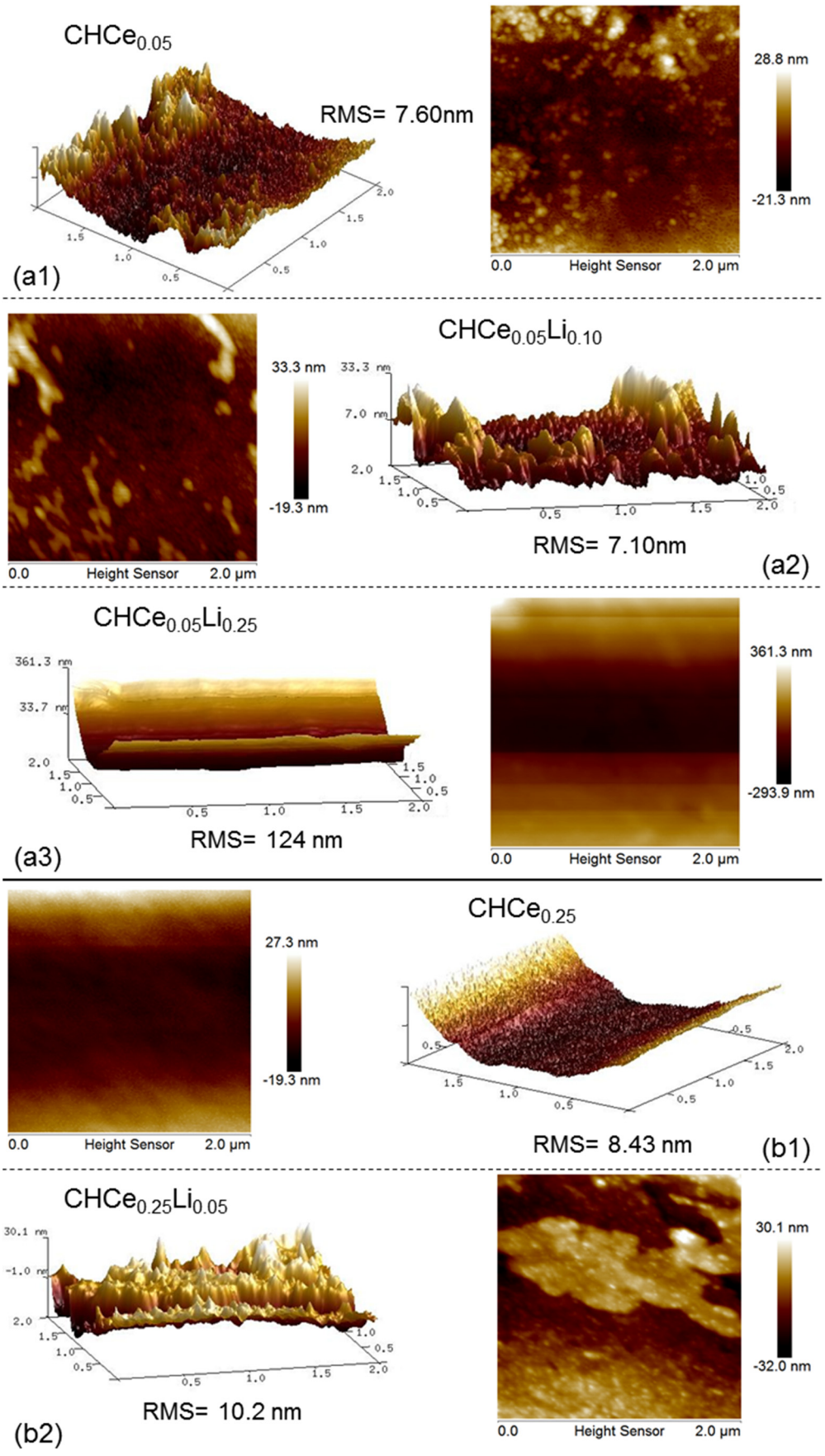

Figure 6.8 AFM images of $CHCe_nLi_m$ -based electrolytes.

6.3.6. Electron Paramagnetic Resonance analysis

Trivalent cerium ion, Ce^{3+}, is a paramagnetic ion with $4f^1$ electronic configuration and ^2F free-ion ground state. Spin orbit coupling causes the separation between $^2F_{7/2}$ and $^2F_{5/2}$ levels, the latter being the ground state separated by 2200 cm^{-1} (~ 0.27 eV) from the $^2F_{7/2}$ excited state. Since the unpaired electron is in the 4f shell and there are two further filled shells (5s and 5p), crystal field effects are smaller than in transition metal ions, where the unpaired electron is in the latest occupied shell. In an axial field, the six-fold J = 5/2 from the $^2F_{5/2}$ level splits into three degenerate Kramer doublets, $M_J = \pm 1/2, \pm 3/2$, and $\pm 5/2$. For tetragonal symmetries, the expected g-values are $g_{\|} = 0.86$ and $g_{\perp} = 2.57$ for a $M_J = \pm 1/2$ doublet ground state; $g_{\|} = 2.57$ and $g_{\perp} = 0$ for a $M_J = \pm 3/2$ ground state; and $g_{\|} = 4.29$ and $g_{\perp} = 0$ for a $M_J = \pm 5/2$ ground state [20-22]. Sometimes, admixture of J levels should be considered to describe experimentally observed g-values [23]. As natural cerium has no isotope with non-zero nuclear spin, the EPR spectrum of Ce^{3+} is composed of a single line without hyperfine structure. Reliable EPR spectra of Ce^{3+} have been reported almost solely for single crystals and polycrystalline materials [21-25].

No signals were observed in the CW-EPR spectra of the three samples investigated. The absorption EPR line shape of Ce^{3+} of sample $CHCe_{0.05}$ was obtained by the pulsed EPR technique EDFS (Figure 6.9 (a)). The observed broad signal (~ 10^4 G) was previously attributed to Ce^{3+}ions in glasses and polycrystalline materials [26, 27]. The principal values of the g-tensor, $g_{zz} = g_{\|} = 0.3$ and $g_{xx} = g_{yy} = g_{\perp} = 1.61$, were obtained from the EDFS spectrum. The observed *g*-values are close to those calculated for a $M_J = \pm 1/2$ doublet ground state. The discrepancy can be explained by assuming admixture with the first excited state $^2F_{7/2}$ [23]. It is interesting to note that the g-values of Ce^{3+} in the CH-CeTrif membranes ($g_{\|} = 0.3$, $g_{\perp} = 1.61$) are rather different from those reported for Ce^{3+} in $La(CF_3SO_3)_3$ crystals ($g_{\|} = 3.81$, $g_{\perp} = 0.26$ for the a $M_J = \pm 5/2$ doublet and $g_{\|} = 0.977$, $g_{\perp} = 2.15$ for the a $M_J = \pm 1/2$ doublet) [21], suggesting that the local coordination environment of the paramagnetic Ce^{3+} is not the same in these system.

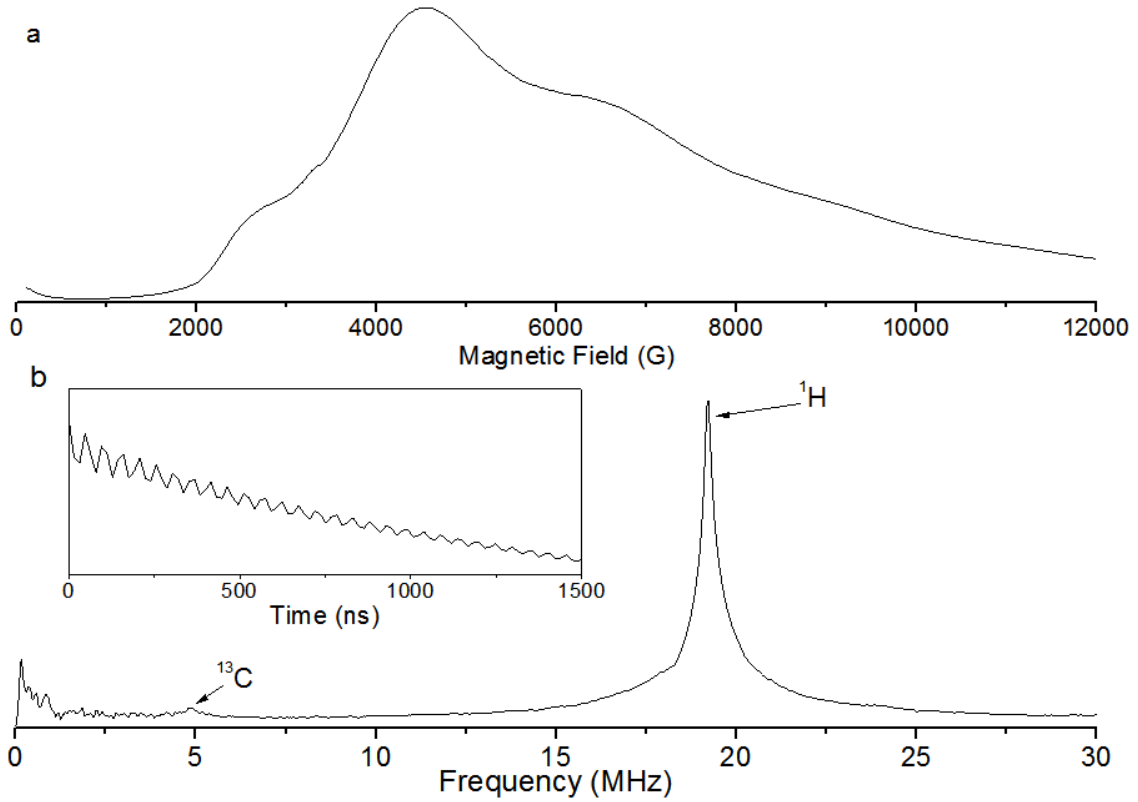

Figure 6.9 Echo-detected field-sweep absorption spectra, EDFS (a) and electron spin echo envelope modulation, ESEEM (b), decay and spectrum of sample $CHCe_{0.05}$. ESEEM experiment was performed at 6 K at a magnetic field of 4500 G, showing a feature at ~19.2 MHz assigned to ^{1}H and a weak feature at ~ 5 MHz assigned to ^{13}C nuclei.

In order to clarify the local environment of Ce^{3+} in the CH-CeTrif membranes the spin-echo pulsed EPR techniques ESEEM and HYSCORE was reported. Figure 6.9 (b) shows the ESEEM decay and spectrum of sample $CHCe_{0.05}$. The envelope decay curve is obtained from the electron spin-echo amplitude recorded as a function of the pulse separation. These decay curves often exhibit a periodic modulation whose frequencies correspond to the Larmor frequencies of nuclear species surrounding the paramagnetic electron spin. Figure 6.9 (b) shows the spectrum obtained from the Fourier transform of the electron spin echo decay. The identification of the nuclear species is performed by comparing the frequency of the peak in the ESEEM spectrum with the Larmor frequencies of nuclei at the magnetic field of the ESEEM experiment. The intense peak at around 19 MHz in Figure 6.9 (b) corresponds to ^{1}H nuclei (nuclear spin I = ½, gyromagnetic ratio γ = 4.2576 kHz/G, natural abundance 100%). The weak peak at around 5 MHz can be assigned to ^{13}C nuclei (I = ½, γ = 1.07 kHz/G, natural abundance 1.1%). It is interesting

to note that there are no peaks corresponding to ^{19}F nuclei (I = ½, γ = 4.0055 kHz/G, natural abundance 100%) in the ESEEM spectra of Figure 6.9 (b) suggesting that the $CF_3SO_3^-$ group does not participate in the complexation of the Ce^{3+} ion.

Information on the magnetic nuclei coupled to the paramagnetic Ce^{3+} in the CH-CeTrif membranes, was obtained with the two-dimensional pulse technique HYSCORE. The spectrum of sample $CHCe_{0.05}$ depicted in Figure 6.10 exhibits an intense signal close to the (19.16 MHz) point of the diagonal line. This isotropic feature results from the interaction between the Ce^{3+} electronic spin and the ^1H nuclei. No features are observed at the Larmor frequency corresponding to the ^{19}F.

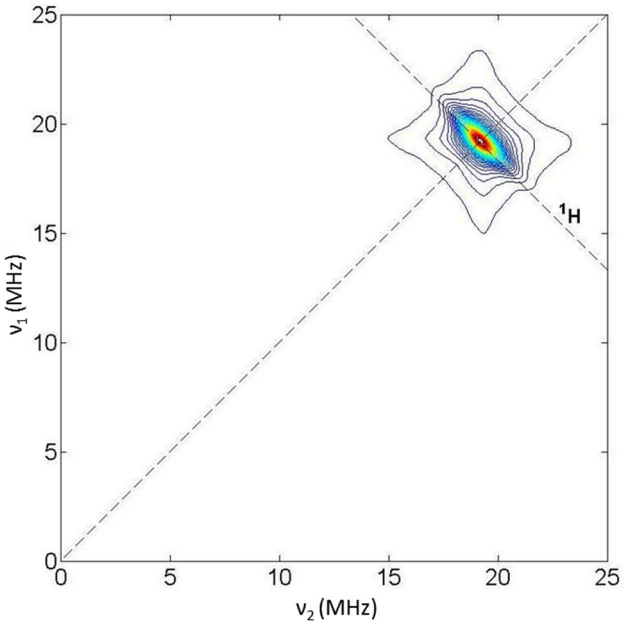

Figure 6.10 Hyperfine Sublevel Correlation, HYSCORE, spectrum of sample $CHCe_{0.05}$ at 6 K with magnetic field strength of 4500 G and τ = 120 ns. Dashed lines mark the position of features due to ^1H.

This interpretation is supported by the observation of the proton peak in the three-pulse ESEEM spectrum (Figure 6.9 (b)). Numerical simulation of the experimental HYSCORE spectrum was performed using a spin Hamiltonian, which includes the electronic and nuclear Zeeman interactions and the hyperfine interaction between the Ce^{3+} unpaired electron spin and the ^1H nuclear spin, equation 6.2 [28, 29]:

$$H = \beta_e H \cdot g \cdot S + \beta_n g_n H \cdot I + S \cdot A^H \cdot I^H \quad (6.2)$$

where β_e is the Bohr magneton, β_n is the nuclear magneton and and I^H is the ^{1}H nuclear spin. The other symbols have they usual meaning. Euler angles (α, β, γ) were included to account for the fact that the g and A^H tensors are not diagonal at the same coordinate system and are defined according to the EasySpin package [30, 31].

The best-fit for the experimental spectrum is achieved with the axial g-tensor interacting with the ^{1}H nucleus. The measured and the simulated HYSCORE spectra of sample $CHCe_{0.05}$ are shown in Figure 6.11. For the simulations, the A^H tensor as $a_{iso}1 + T$, where a_{iso} is the isotropic hyperfine coupling and T is a traceless tensor containing only dipolar hyperfine coupling were written. The values used to generate the best-fit simulation are listed in Table 6.1. The intense proton peaks found in the HYSCORE spectra belong to protons of CH with hyperfine couplings a_{iso} = 0.6 MHz, $T_\perp$ = 3.4 MHz, which are comparable those reported for $Cu(H_2O)_6$ in MCM-41 (a_{iso} = 1.5 MHz, $T_\perp$ = 4.8 MHz) [32] and pyridine - copper complex (a_{iso} = 4 MHz, $T_\perp$ = 2.6 MHz) [21].

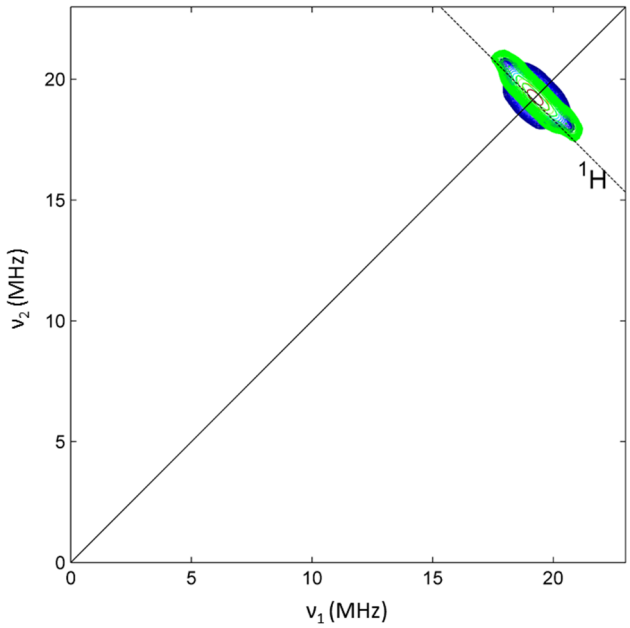

Figure 6.11 HYSCORE spectrum of sample $CHCe_{0.05}$ (blue contours) and its numerical simulation (green contours). The dashed line marks the position of features due to ^{1}H. Both experimental and numerical spectra were normalized. The parameters used to generate the numerical simulation are displayed in Table 6.1.

Table 6.1 Parameters used to generate the numerical simulation of the HYSCORE spectrum at 4500 G. For the simulations, we assumed an axial g-tensor with principal values $g_{xx} = g_{yy} = g_{\perp} = 1.61$ and $g_{zz} = g_{\parallel} = 0.3$. The three Euler angles (α, β, γ) rotates the A-tensor from the coordinate system where the g-tensor is diagonal.

	T_{xx} (MHz)	T_{yy} (MHz)	T_{zz} (MHz)	a_{iso} (MHz)	α (°)	β (°)	γ (°)
site Ce^{3+}	-3.6	-3.6	7.2	0.6	0	62	0

Assuming that the anisotropic part of the hyperfine interaction ($T_{\perp}$ = 3.4 MHz) can be described by a point-dipolar interaction, the distance (r) between the unpaired electron of Ce^{3+} ion and the protons of the CH macromolecule can be estimated from the equation 6.3 [28, 33, 34]:

$$T_{\perp} = \frac{g_e g_n \beta_e \beta_n}{h r^3} \tag{6.3}$$

where h is the Planck constant, g_e = 2.0023 is the free electron g-factor, and $g_n = \hbar\gamma_n/\beta_n$ = 5.5857 is the ^{1}H nuclear g-factor. A Ce−H distance of 2.83 Å (0.28 nm) was found which is consistent with the distance between the cation and macromolecular protons in polymer electrolytes [35].

6.4. Conclusion

This paper reports thermal analysis, conductivity, XRD, SEM, AFM, and EPR measurements in electrolytes formed by CH, prepared from acetic acid solution and containing glycerol and binary system of two salts: cerium and lithium triflates. The obtained results were compared to the membranes with only one salt system. All prepared samples presented good flexibility, homogeneity, and transparency. The thermal analysis revealed that the degradation occurs in three stages, and the samples are thermally stable up to 128 - 153ºC. The best room temperature ionic conductivity, 10^{-6} S cm^{-1} (at 30ºC), was obtained for the samples with 0.15 g of total salt amount. Most of the electrolytes are amorphous, and the appearance of crystalline peaks in XRD data are due to the diffraction

of salt domains. Because there was no signal in CW-PR spectra, pulsed EPR technique EDFS was used to study interaction of Ce^{3+} ion with CH network. The observed broad signal (~ 10^4 G), attributed to Ce^{3+}ions, had values of the g-tensor, $g_{zz} = g_{||} = 0.3$ and $g_{xx} = g_{yy} = g_{\perp} = 1.61$, which were close to those calculated for a $M_J = \pm 1/2$ doublet ground state and explained by assuming admixture with the first excited state $^2F_{7/2}$. To investigate a local coordination environment of the paramagnetic Ce^{3+} the spin-echo pulsed EPR techniques ESEEM and HYSCORE technique were used. The results revealed no peaks corresponding to ^{19}F, suggesting that the $CF_3SO_3^-$ group does not participate in the complexation of the Ce^{3+} ion. HYSCORE numerical simulation revealed that the paramagnetic Ce^{3+} in the CH-CeTrif membranes is coupled to ^1H nuclei of CH, and an Ce-H distance is 2.83 Å (0.28 nm).

6.5. References

[1] Y. Wan, K.A.M. Creber, B. Peppley, V.T. Bui, Chitosan-based solid electrolyte composite membranes: I. Preparation and characterization, Journal of Membrane Science, 280 (2006) 666-674.

[2] R. Alves, F. Sentanin, R.C. Sabadini, A. Pawlicka, M.M. Silva, Influence of cerium triflate and glycerol on electrochemical performance of chitosan electrolytes for electrochromic devices, Electrochimica Acta, 217 (2016) 108-116.

[3] L.S. Ng, A.A. Mohamad, Effect of temperature on the performance of proton batteries based on chitosan-NH_4NO_3-EC membrane, Journal of Membrane Science, 325 (2008) 653-657.

[4] R. Alves, M.M. Silva, The Influence of Glycerol and Formaldehyde in Gelatin-Based Polymer Electrolytes, Molecular Crystals and Liquid Crystals, 591 (2014) 64-73.

[5] R. Leones, L.C. Rodrigues, M. Fernandes, R.A.S. Ferreira, I. Cesarino, A. Pawlicka, L.D. Carlos, V. de Zea Bermudez, M. Silva, Electro-optical properties of the DNA-Eu^{3+} bio-membranes, Journal of Electroanalytical Chemistry, 708 (2013) 116-123.

[6] E. Lima, E. Raphael, F. Sentanin, L.C. Rodrigues, R.A.S. Ferreira, L.D. Carlos, M.M. Silva, A. Pawlicka, Photoluminescent polymer electrolyte based on agar and containing europium picrate for electrochemical devices, Materials Science and Engineering: B, 177 (2012) 488-493.

[7] C.O. Avellaneda, D.F. Vieira, A. Al-Kahlout, E.R. Leite, A. Pawlicka, M.A. Aegerter, Solid-state electrochromic devices with Nb_2O_5:Mo thin film and gelatin-based electrolyte, Electrochimica Acta, 53 (2007) 1648-1654.

[8] A.M. Stephan, R. Thirunakaran, N.G. Renganathan, V. Sundaram, S. Pitchumani, N. Muniyandi, R. Gangadharan, P. Ramamoorthy, A study on polymer blend electrolyte based on PVC/PMMA with lithium salt, Journal of power sources, 81 (1999) 752-758.

[9] G.M. Wu, S.J. Lin, C.C. Yang, Preparation and characterization of PVA/PAA membranes for solid polymer electrolytes, Journal of Membrane Science, 275 (2006) 127-133.

[10] C.O. Avellaneda, D.F. Vieira, A. Al-Kahlout, S. Heusing, E.R. Leite, A. Pawlicka, M.A. Aegerter, All solid-state electrochromic devices with gelatin-based electrolyte, Solar Energy Materials and Solar Cells, 92 (2008) 228-233.

[11] R.D. Alves, L.C. Rodrigues, J.R. Andrade, M. Fernandes, J.V. Pinto, L. Pereira, A. Pawlicka, R. Martins, E. Fortunato, V. de Zea Bermudez, M.M. Silva, $Gelatin_nZn(CF3_SO_3)_2$ polymer electrolytes for electrochromic devices, Electroanalysis, 25 (2013) 1483-1490.

[12] A. Kumar, R. Sharma, M.K. Das, P. Gajbhiye, K.K. Kar, Impacts of ceramic filler and the crystallite size of polymer matrix on the ionic transport properties of lithium triflate/poly(vinylidene fluoride-co-hexafluoropropene) based polymer electrolytes, Electrochimica Acta, 215 (2016) 1-11.

[13] M.F. Shukur, R. Ithnin, M.F.Z. Kadir, Electrical properties of proton conducting solid biopolymer electrolytes based on starch-chitosan blend, Ionics, 20 (2014) 977-999.

[14] S. Rajendran, M. Sivakumar, R. Subadevi, Investigations on the effect of various plasticizers in PVA-PMMA solid polymer blend electrolytes, Materials Letters, 58 (2004) 641-649.

[15] S.M.G. Correia, V. de Zea Bermudez, M.M. Silva, S. Barros, R.A.S. Ferreira, L.D. Carlos, A.P. Passos de Almeida, M.J. Smith, Morphological and conductivity studies of di-ureasil xerogels containing lithium triflate, Electrochimica acta, 47 (2002) 2421-2428.

[16] R.D. Alves, L.C. Rodrigues, J.R. Andrade, A. Pawlicka, L. Pereira, R. Martins, E. Fortunato, M.M. Silva, Study and characterization of a novel polymer electrolyte based on agar doped with magnesium triflate, Molecular Crystals and Liquid Crystals, 570 (2013) 1-11.

[17] G. Ribeiro, M. Conde, J. Carvalho, L.C. Rodrigues, R. Alves, R.A.S. Ferreira, A. Pawlicka, L.D. Carlos, M.M. Silva, Natural Membranes for Application in Biomedical Devices, Molecular Crystals and Liquid Crystals, 562 (2012) 147-155.

[18] I. Nicotera, L. Coppola, C. Oliviero, M. Castriota, E. Cazzanelli, Investigation of ionic conduction and mechanical properties of PMMA-PVdF blend-based polymer electrolytes, Solid State Ionics, 177 (2006) 581-588.

[19] R. Alves, A.S.S. de Camargo, A. Pawlicka, M.M. Silva, Luminescent polymer electrolytes based on chitosan and containing europium triflate, Journal of Rare Earths, 34 (2016) 661-666.

[20] A. Abragam, B. Bleaney, Electron paramagnetic resonance of transition ions, OUP Oxford, 2012.

[21] D.T. Petasis, G.H. Bellesis, N.S. VanderVen, S.A. Friedberg, Electron paramagnetic resonance of Ce^{3+} in $La(CF_3SO_3)_3 \cdot 9H_2O$, Journal of Applied Physics, 70 (1991) 5998-6000.

[22] L. Pidol, O. Guillot-Noël, A. Kahn-Harari, B. Viana, D. Pelenc, D. Gourier, EPR study of Ce^{3+} ions in lutetium silicate scintillators $Lu_2Si_2O_7$ and Lu_2SiO_5, Journal of Physics and Chemistry of Solids, 67 (2006) 643-650.

[23] M. Yamaga, M. Honda, K. Shimamura, T. Fukuda, T. Yosida, Electron spin-resonance study on Ce^{3+} in $BaLiF_3$, Journal of Physics: Condensed Matter, 12 (2000) 5917.

[24] J.D. Barrie, L.A. Momoda, B. Dunn, D. Gourier, G. Aka, D. Vivien, ESR and optical spectroscopy of Ce^{3+}: β″-alumina, Journal of Solid State Chemistry, 86 (1990) 94-100.

[25] F.F. Popescu, V. Bercu, J.N. Barascu, M. Martinelli, C.A. Massa, L.A. Pardi, M. Stefan, S.V. Nistor, M. Nikl, Study of the Kramers rare earth ions ground multiplet with a large orbital contribution by multifrequency EPR spectroscopy: Ce^{3+} in $PbWO_4$ scintillator, Optical Materials, 32 (2010) 570-575.

[26] C.J. Magon, J.P.D. Gonzalez, J.F. Lima, H. Eckert, E.D. Zanotto, J. Lumeau, L. Glebova, L. Glebov, Electron Paramagnetic Resonance (EPR) studies on the photo-thermo ionization process of photo-thermo-refractive glasses, Journal of Non-Crystalline Solids, 452 (2016) 320-324.

[27] M. Chiesa, K. Mattsson, S. Taccheo, T. Robin, L. Lablonde, D. Mechin, D. Milanese, Defects induced in Yb^{3+}/Ce^{3+} co-doped aluminosilicate fiber glass preforms under UV and γ-ray irradiation, Journal of Non-Crystalline Solids, 403 (2014) 97-101.

[28] A. Pöppl, M. Hartmann, W. Böhlmann, R. Böttcher, Coordination Geometry of the Copper-Pyridine Complex in Frozen Solution As Studied by Proton and Deuterium Two-Dimensional Hyperfine Sublevel Correlation Electron Spin Resonance Spectroscopy, The Journal of Physical Chemistry A, 102 (1998) 3599-3606.

[29] P.J. Carl, D.E.W. Vaughan, D. Goldfarb, Interactions of Cu (II) ions with framework Al in high Si:Al zeolite Y as determined from X-and W-band pulsed EPR/ENDOR spectroscopies, The Journal of Physical Chemistry B, 106 (2002) 5428-5437.

[30] V. Chechik, E. Carter, D. Murphy, Electron Paramagnetic Resonance, Oxford Chemistry Primers, Oxford, 2016.

[31] S. Stoll, R.D. Britt, General and efficient simulation of pulse EPR spectra, Physical Chemistry Chemical Physics, 11 (2009) 6614-6625.

[32] A. Pöppl, L. Kevan, A practical strategy for determination of proton hyperfine interaction parameters in paramagnetic transition metal ion complexes by two-dimensional HYSCORE electron spin resonance spectroscopy in disordered systems, The Journal of Physical Chemistry, 100 (1996) 3387-3394.

[33] H. Vezin, A. Moissette, M. Hureau, C. Brémard, trans-Stilbene Incorporation in Acidic Medium-Pore ZSM-5 Zeolite: A Pulsed EPR Study, ChemPhysChem, 7 (2006) 2474-2477.

[34] S. Maurelli, G. Berlier, M. Chiesa, F. Musso, F. Corà, Structure of the Catalytic Active Sites in Vanadium-Doped Aluminophosphate Microporous Materials. New Evidence from Spin Density Studies, The Journal of Physical Chemistry C, 118 (2014) 19879-19888.

[35] J.P. Donoso, T.J. Bonagamba, H.C. Panepucci, L.N. Oliveira, W. Gorecki, C. Berthier, M. Armand, Nuclear magnetic relaxation study of poly(ethylene oxide)-lithium salt based electrolytes, The Journal of Chemical Physics, 98 (1993) 10026-10036.

Chapter 7

The effect of glycerol amount in chitosan electrolytes containing different lanthanide salts: A comparison when applied in electrochromic devices

This chapter was adapted from: R. Alves, F. Sentanin, R. C. Sabadini, A. Pawlicka, M. M. Silva, Influence of cerium triflate and glycerol on electrochemical performance of chitosan electrolytes for electrochromic devices, Electrochimica Acta 217 (2016) 108-116. R. Alves, F. Sentanin, R. C. Sabadini, A. Pawlicka, M. M. Silva, Innovative electrolytes based on chitosan and thulium for solid state applications: Synthesis, structural, and thermal characterization, Journal of Electroanalytical Chemistry 788 (2017) 156-164. R. Alves, F. Sentanin, R. C. Sabadini, A. Pawlicka, M. M. Silva, Solid polymer electrolytes based on chitosan and $Dy(CF_3SO_3)_3$ for electrochromic devices, Solid State Ionics 310 (2017) 112-120. R. Alves, F. Sentanin, R. C. Sabadini, A. Pawlicka, M. M. Silva, Green Polymer Electrolytes of Chitosan Doped with Erbium Triflate, Journal of Non-Crystalline Solids 482 (2018) 183-191. R. Alves, F. Sentanin, R. C. Sabadini, M. Fernandes, V. de Zea Bermudez, A. Pawlicka, M. M. Silva, Samarium (III) Triflate-doped Chitosan Electrolyte for Solid State Electrochromic Devices, Electrochimica Acta (2017) *in press*.

7.1. Objective

The main objective of this chapter is verify the effect of the glycerol amount in the samples. So, starting from the best conducting sample of cerium triflate, new samples were prepared with higher glycerol amount and the conductivity results was evaluated. With these results, the optimum glycerol quantity was chosen and the samples with other salts were prepared with this glycerol amount and the optimum salt level. The samples with higher glycerol amount were applied in small ECDs and their performance were evaluated.

7.2. Experimental section

Samples were prepared according to the procedure described previously in chapter 2, and in Figure 7.1 is presented the electrolytes preparation scheme, and their physical appearance. The samples were represented by the notation CHLnTrif$_x$Gly$_y$, where Ln = Ce, Tm, Dy, Sm or Er, x = salt mass used, and y = glycerol amount, accordingly to Table 7.1. The thickness of the samples varied between 0.063 and 0.190 ± 0.001 mm, in samples with less glycerol amount, and between 0.216 and 0.270 ± 0.001 mm, for electrolytes with higher glycerol quantity.

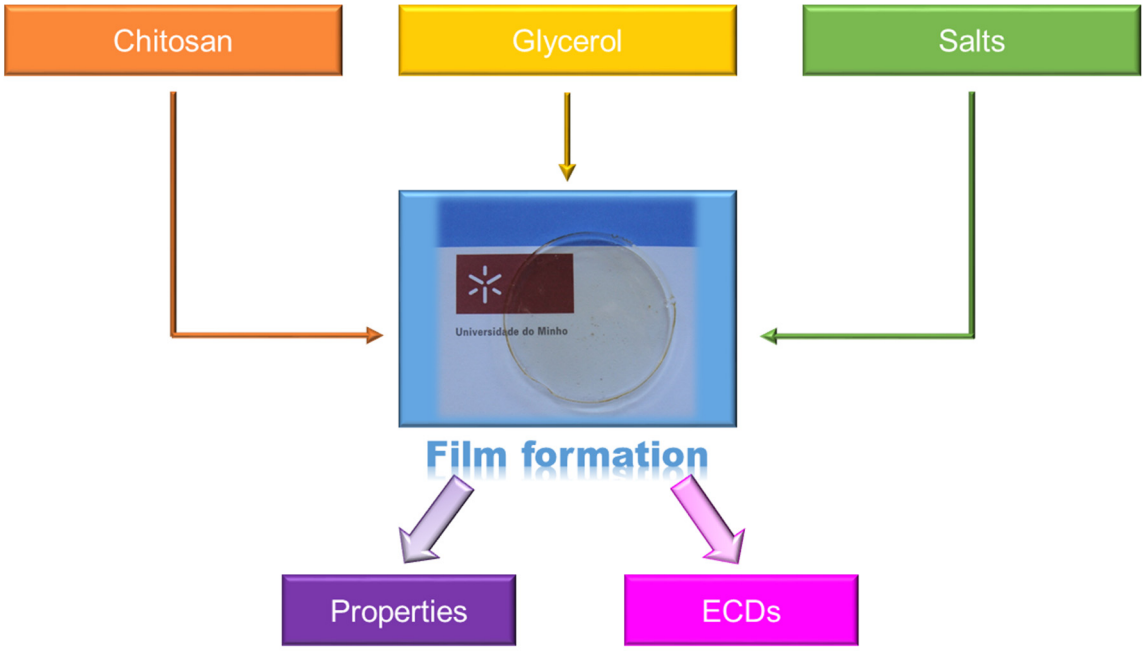

Figure 7.1 Samples preparation scheme, and physical appearance of the electrolytes.

Table 7.1 Composition and designation of samples.

Samples designation	*x* (g) (±0.00001)	*y* (g) (±0.00001)
$CHCeTrif_{0.10}Gly_{0.25}$	0.10188	0.26700
$CHCeTrif_{0.10}Gly_{0.40}$	0.10006	0.40605
$CHCeTrif_{0.10}Gly_{0.55}$	0.10354	0.55807
$CHCeTrif_{0.10}Gly_{0.70}$	0.10345	0.70760
$CHTmTrif_{0.05}Gly_{0.25}$	0.05263	0.26203
$CHTmTrif_{0.05}Gly_{0.70}$	0.05245	0.70616
$CHDyTrif_{0.15}Gly_{0.25}$	0.15303	0.25282
$CHDyTrif_{0.15}Gly_{0.70}$	0.15236	0.70509
$CHSmTrif_{0.05}Gly_{0.25}$	0.05232	0.25365
$CHSmTrif_{0.05}Gly_{0.70}$	0.05050	0.70891
$CHErTrif_{0.05}Gly_{0.25}$	0.05230	0.25276
$CHErTrif_{0.05}Gly_{0.70}$	0.05511	0.70680

The total ionic conductivities were determined by impedance spectroscopy. The thermal behavior was evaluated by thermal analysis (TGA and DSC). The morphology and structure were evaluated by XRD, and SEM.

Also, the best, but moderate, ionically conducting electrolytes were applied in electrochromic devices with glass/ITO/PB or WO_3/ $CHLnTrif_xGly_{0.70}$-based electrolyte/CeO_2-TiO_2/ITO/glass configuration, and their electrochemical and spectral characteristics were recorded.

7.3. Results and discussion

7.3.1. Impedance spectroscopy

Aiming to verify the effect of glycerol amount in the ionic conductivity, samples with fixed 0.10 g of cerium salt and either 0.25, 0.40, 0.55, and 0.70 g of glycerol were prepared, and the conductivity results of these samples are presented in Figure 7.2.

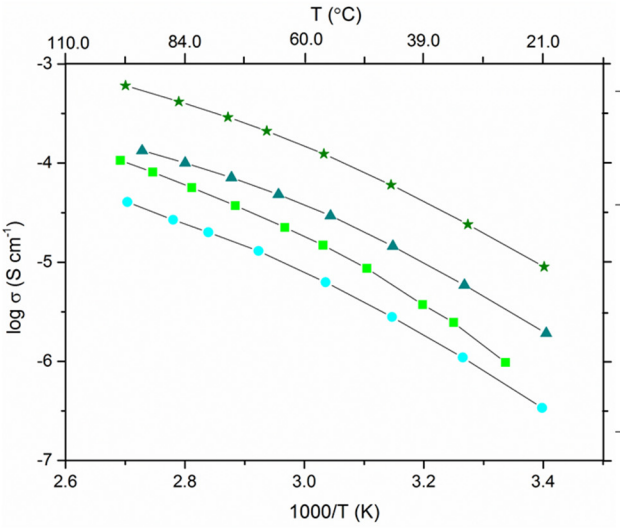

Sample	σ (S cm^{-1}) T = 30ºC	σ (S cm^{-1}) T = 90ºC
CHCeTrif$_{0.10}$Gly$_{0.25}$	1.15×10^{-6}	7.94×10^{-5}
CHCeTrif$_{0.10}$Gly$_{0.40}$	6.50×10^{-7}	3.29×10^{-5}
CHCeTrif$_{0.10}$Gly$_{0.55}$	3.82×10^{-6}	1.24×10^{-4}
CHCeTrif$_{0.10}$Gly$_{0.70}$	1.67×10^{-5}	4.93×10^{-4}

Figure 7.2 Conductivity plots of CHCeTrif$_{0.10}$Gly$_y$-based electrolytes as a function of inverse of temperature, y = 0.25, 0.40, 0.55, and 0.70 g. Conductivity values at 30 and 90ºC in inset.

As already expected, an increase of glycerol amount promotes an increase of ionic conductivity of the samples, except of the sample with 0.40 g of glycerol, and this can be seen in Figure 7.2. Another kind of analyses, such XRD and SEM, would be need to try to understand what happen for this sample, but an incomplete dissolution of the plasticizer or polymer/plasticizer phase separation can be possible explanations. There are many reports on the effect of plasticizer on the ionic conductivity values [1-4]. Usually, a presence of plasticizer promotes an enhancement of ionic conductivity because it contributes to an increase of the free volume of the polymer matrix. The large size of the free volume leads to an increase of the mobility of polymeric chain that, results in the improvement of the ionic transport [5]. In gelatin-based electrolytes plasticized with 7 to 48% of glycerol, the conductivity increased as a function of the plasticizer content for all samples in whole temperature range. For the sample with 25% of glycerol, the conductivity values were of 5×10^{-5} and 3.6×10^{-4} S cm^{-1} at room temperature and 80ºC, respectively [6]. In samples with hydroxyethylcellulose, lithium triflate, and different quantities of glycerol, the conductivity values increased from 1.26×10^{-6} to 1.06×10^{-5} S cm^{-1} for the samples with 12 and 48% at 30ºC, respectively. A decrease of conductivity above 48% was explained in terms of polymer/plasticizer phase separation because of high quantity of plasticizer [7]. This is not observed in this case since the sample with the highest glycerol amount presents the best conductivity values. For films of pectin with

different quantities of glycerol, the conductivity results increased from 10^{-5} S cm^{-1} for the samples with 37 wt% of glycerol to 4.7×10^{-4} S cm^{-1} for the sample with 68 wt% of glycerol, at room temperature. The presence of high plasticizer contents probably promotes a better separation of polymeric chains that, results in an increase of the conductivity values [8]. Sample with 0.40 g of glycerol displays similar behavior of ionic conductivity as a function of inverse of temperature when compared to other samples, but it has lower values than the less conductive sample, i.e., with 0.25 g of glycerol. For instance, the reason for that is being investigated. The mechanism of ionic conduction follows the VTF model, what means that the ionic transport is mainly promoted by the polymeric movement. In these cases, the high quantities of plasticizer probably promote a better separation of polymeric chains leading to more pronounced movements. Comparing the $CH(CeTrif)_{0.10}Gly_{0.25}$ with the $CH(CeTrif)_{0.10}Gly_{0.70}$ sample, it is observed that incorporation of higher plasticizer amount increases the conductivity values from 1.46×10^{-6} to 1.67×10^{-5} S cm^{-1}, at 30ºC, and so 0.70 g was the glycerol amount chosen to prepare the remaining samples.

The ionic conductivity plots of $CHLnTrif_xGly_y$, for Ln = Tm, Dy, Sm, and Er, as a function of temperature are shown in Figure 7.3, and as expected, an increase in glycerol amount promotes an increase of ionic conductivity. Plasticization is a most effective way to improve conductivity, and the role of the plasticizer is to dissociate the salt, which leads to the increase in the number of mobile ions and contributes to the conductivity enhancement [9]. In the present study, the increase in plasticizer quantity leads to an increase in ionic conductivity by 1 or 2 orders of magnitude, as can be seen in the table present in Figure 7.3. The addition of high plasticizer amounts provides samples with high conductivities, and promotes a better contact between electrodes and electrolyte, for conductivity measurements. The use of plasticizer improves the ionic conductivity because it allows a dissociation of ion aggregates and increases amorphous phase content. In PEs, the amorphous phase is the high conducting, and so the addition of plasticizers can help to enhance the ionic conductivity.

The plots in Figure 7.3 show that as temperature increases the conductivity also increases. The ionic conductivity increases with the increase in temperature due to the thermal movement of polymer chain segments, so there is an improvement of salt dissociation. This increase is interpreted as a hopping mechanism between coordinating sites, local structural relaxation, and segmental motions of polymer-salt complexes. As square mean

root of the fittings of plots in Figure 7.3 are almost unity ($r^2 \approx 1$), so the results obey Arrhenius law expressed in equation (7.1):

$$\sigma = \sigma_0 exp\left(\frac{-E_a}{RT}\right) \tag{7.1}$$

where σ is the ionic conductivity, σ_0, E_a, R, and T are the pre-exponential factor, the apparent activation energy for ion transport, the gas constant (8.413 J mol^{-1} K^{-1}), and the temperature, respectively [10]. The E_a was calculated from the slope of the graph for each sample, and the obtained values vary between 52.27 - 65.48 and 47.81 - 55.72 kJ mol^{-1} for the samples with 0.25 and 0.70 g of glycerol, respectively. Therefore, the activation energy decreases from the sample with less glycerol quantity to the sample with higher plasticizer amount, as can be seen from the E_a values present in the Figure 7.3. This implies that, in all cases, and independently to the salt, the electrolyte with high glycerol amount is the highest conducting sample and possesses the lowest activation energy, which is usually expected because the lower energy barrier results in easier ionic movement [10].

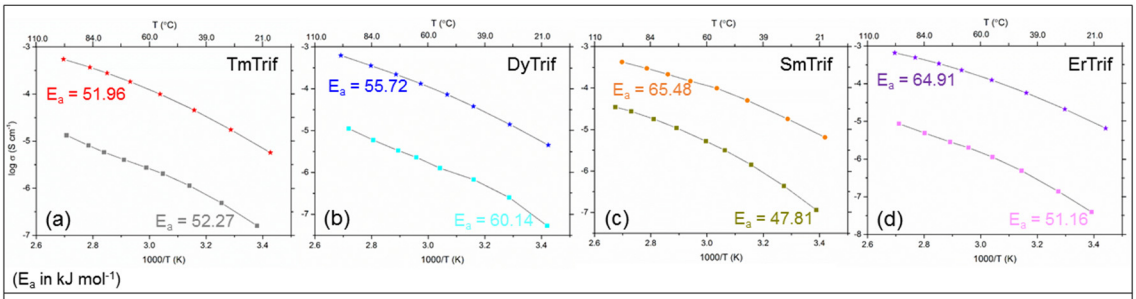

(E_a in kJ mol^{-1})

	σ (S cm^{-1})							
T (ºC)	TmTrif		DyTrif		SmTrif		ErTrif	
	-■- 0.25 gly	-★- 0.70 gly	-■- 0.25 gly	-★- 0.70 gly	-■- 0.25 gly	-★- 0.70 gly	-■- 0.25 gly	-★- 0.70 gly
30	3.47×10^{-7}	1.60×10^{-5}	1.85×10^{-7}	1.31×10^{-5}	3.65×10^{-7}	1.68×10^{-5}	1.15×10^{-7}	2.06×10^{-5}
90	1.07×10^{-5}	4.84×10^{-4}	9.55×10^{-6}	5.05×10^{-4}	2.68×10^{-5}	3.87×10^{-4}	8.15×10^{-6}	5.91×10^{-4}

Figure 7.3 Conductivity plots and E_a values of CHLnTrif$_x$Gly$_y$-based electrolytes as a function of inverse of temperature, for y = 0.25 or 0.70 g, and (a) TmTrif$_{0.05}$, (b) DyTrif$_{0.15}$, (c) SmTrif$_{0.05}$ and (d) ErTrif$_{0.05}$. Conductivity values at 30 and 90ºC in inset.

7.3.2. Thermal behavior

Thermogravimetric analyses were carried out to evaluate the effect of the salt and the plasticizer on the thermal stability of CH. The thermal stability measured at increasing temperature was investigated for each synthesized sample, and the TGA and DTGA curves are shown in Figure 7.4. The thermal degradation seems to occur in three stages, for the samples with dysprosium triflate (Figure 7.4 (a)), and in two stages, for the samples with samarium and erbium triflate (Figure 7.4 (b) and (c)). These results may be due to the different interactions of salt and glycerol with polysaccharide chains, and the difference in the obtained stages is related to the different salt amount used to produce the electrolytes. In DyTrif more salt was used to prepare the samples (0.15 g) and three stages are observed, while in Sm and Er systems, where 0.05 g were used, in thermograms only two steps are perceptible.

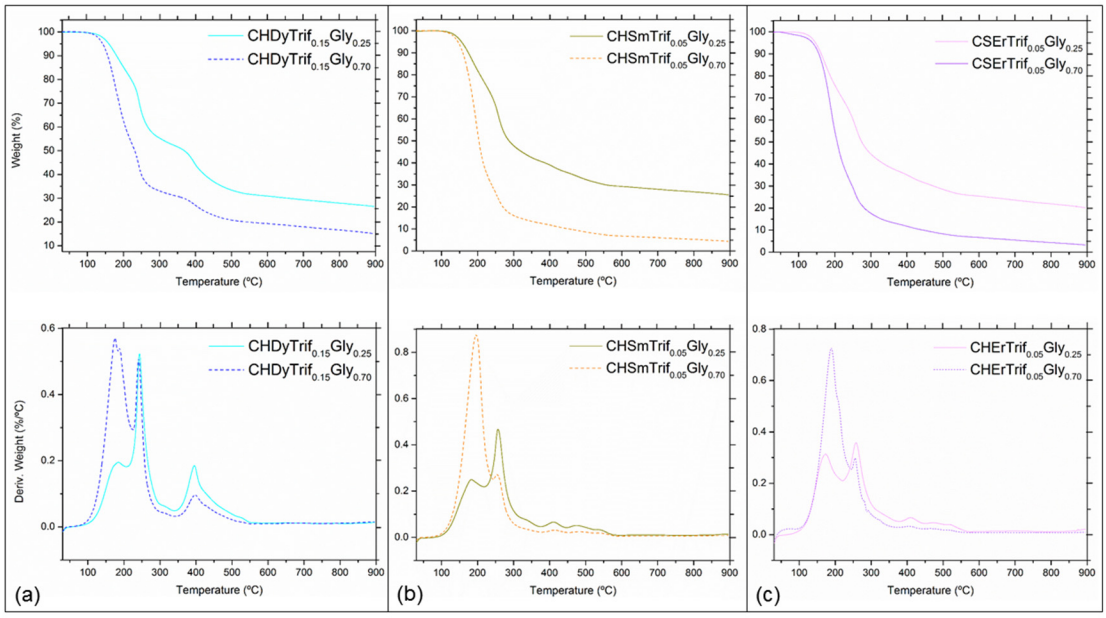

Figure 7.4 TGA and DTGA curves for the samples with Dy (a), Sm (b), and ErTrif (c).

When comparing the results, it can be observed that the first stage is more pronounced for the sample with higher glycerol amount (dash lines in Figure 7.4), and the onset decomposition starts between 134 - 158ºC with a weight loss above 40% in all cases. In electrolytes with less glycerol quantity (solid lines in Figure 7.4) the first weight loss is below 30%, and it occurs between 135 - 139ºC. In this first step, the weight loss increase with the increase in glycerol amount, and so it may be related to the degradation of

glycerol. Also in a study of a blend starch-CH doped with NH_4Cl and containing 35 wt% of glycerol, the authors attributed the weight loss of ~20% at about 136 - 177ºC to the degradation of glycerol in the electrolyte [11].

In DyTrif system, the increase in the glycerol amount made the samples less thermally stable, but did not alter significantly the degradation temperature of the samples, that decreases from 135 to 134ºC. For the Sm and Er systems, the increase in plasticizer amount promotes an increase of the onset decomposition from 138 to 145ºC, and 139 to 158ºC, respectively. These results allow to conclude that the increase of the plasticizer amount contribute to the host matrix stabilization. The relatively low value obtained for the first degradation step is probably due to presence of acetic acid used in the film preparation, the degradation of plasticizer in the electrolytes, and also due to the salt added to the matrix that probably acts as catalyst for polymeric chain disintegration. However, despite the low values obtained, the onset temperature for all the samples are considered adequate for solid-state electrochemical devices.

The second step was observed above 200ºC, and it may explains the decomposition peak observed at about 241 - 258ºC in the DTGA curves, Figure 7.4 (b). This stage may be due to a complex process including depolymerization, dehydration of the saccharide rings, and decomposition of units of polymers. In a study of gellan gum and CH biohydrogels the DTGA curve of CH displayed a degradation peak at 302ºC. In these biohydrogels the peak related to the degradation of CH appeared, however, at lower temperature (245ºC) [12]. The shift of the peak to lower temperatures is probably due to the salt and plasticizer used, and to their different interactions with polymer chains. On the other hand, when CH powder was transformed into a CH film the decomposition occurred at lower temperature because of traces of acetic acid that probably induced its thermal decomposition [13].

The third and last stage increases in the samples with less glycerol amount, and it is more perceptible in the DyTrif electrolytes, Figure 7.4 (a), probably due to the fact that it has more salt amount. For all samples, the degradation process ended at approximately 500ºC and the weight loss continued slowly as the temperature increased up to 900ºC. The remaining residues were in the 20 - 27 % range, for the samples with less glycerol amount, and the values decreases from 3.3 - 15 % range in the electrolytes with higher glycerol quantity.

The thermal history of the materials is very important to get more details about their possible practical application. T_g is an important parameter, which can influence the ionic conduction mechanism and SPE's conductivity values. The local movement of polymer chain helps to increase the conductivity, so polymers with T_g bellow the operating temperature are desirable for electrochemical applications. The DSC curves of CH electrolytes doped with different LnTrif salts and containing different glycerol amounts are shown in Figure 7.5. The analyses were performed in the temperature range from -60 to 200ºC, and the maximum temperature of 200ºC used was selected to limit possible CH degradation. Figure 7.5 results show no T_g, which is an indication that all samples are predominantly amorphous. Another conclusion that may be retrieved from this figure is that all samples produced an endothermic event above 120ºC, assigned to the sol-gel transition [14]. A closer examination reveals differences in the peak area and position of this endotherm. These differences are related to the kind of salt and glycerol amount used in the preparation of the samples. In samples where glycerol co-exists with water the boiling point depends on the relative portion of both components. In the present case, the boiling point of the mixture would be about 100ºC, for the samples with lower glycerol amount, and about 114ºC for the electrolyte with higher glycerol quantity, which may explain the large endothermic peak observed in Figure 7.5 (c). On another hand, one large endothermic peak can be seen in Sm sample with less plasticizer amount. A similar peak appeared in CH-based electrolytes doped with thulium triflate and it was attributed to waters release due to both hydrophilic nature of CH and salt [15]. The other endotherm events, that appeared centered at above 175ºC, may be related to the beginning of the sample's decomposition.

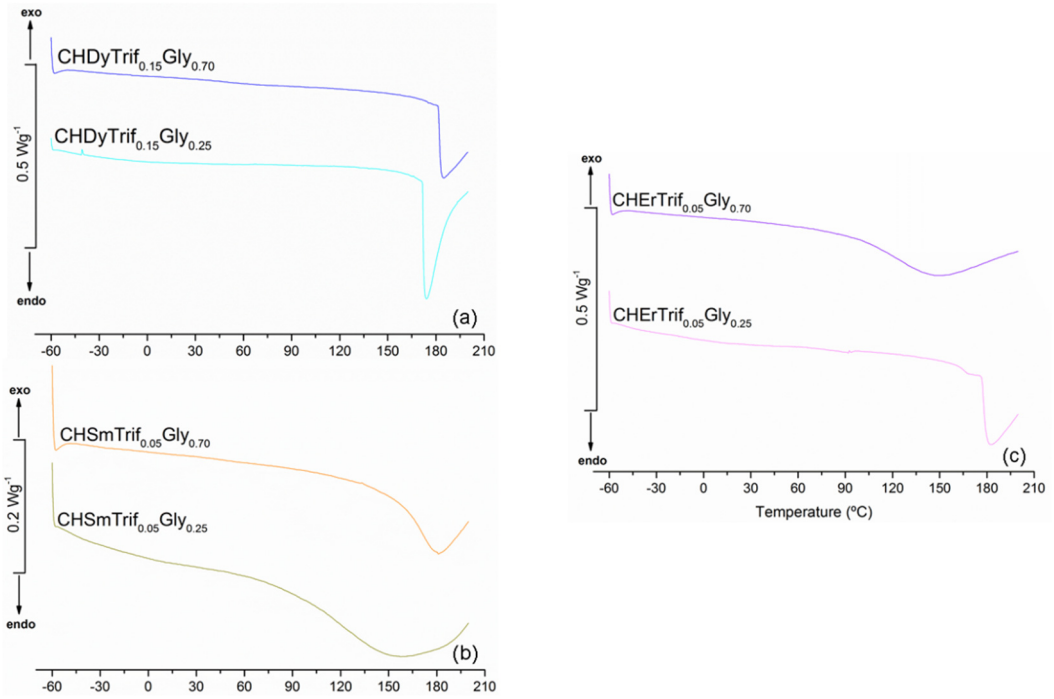

Figure 7.5 DSC thermograms of CHLnTrif$_x$Gly$_y$-based electrolytes, for Ln = Dy (a), Sm (b), and Er (c), and for x = 0.05 - 0.15 g and y = 0.25 or 0.70 g.

7.3.3. Morphology and structure

The effect of glycerol on the structure of CH-based polymer electrolyte doped with Dy and SmTrif was investigated by X-ray diffraction. Figures 7.6 (a) and (b) show the XRD diffraction patterns of doped samples of DyTrif and SmTrif with different glycerol amounts, respectively. In the 3 - 60º 2θ range, a few sharp peaks and one broad peak centered at about 20º were observed, and this broad diffraction peak suggest the amorphous nature of the PEs [1, 16-18]. This peak is weakened in the samples with less glycerol amount, which may be due to the local change in the sample's amorphous nature caused by the interaction between the constituents of the polymer/salt complexes. In the electrolytes with DyTrif, Figure 7.6 (a), both samples presented one sharp peak that appear at about 2θ ~ 30º and it corresponds to the salt. Also in SmTrif-based electrolytes, Figure 7.6 (b), the small crystalline peaks observed are attributed to samarium salt, and indicate the formation of aggregates, or that the salt is not totally accommodated in the matrix. On another hand, a new peak is observed at about 35º for the sample with DyTrif and higher glycerol amount. This peak may suggest some local ordering due to the excess of glycerol. In a study of CH-oxalic acid polymer electrolytes with 50% oxalic acid

content a new peak at 2θ ~ 36º was observed in the XRD diffractograms suggesting the presence of the local ordering due to the excess of oxalic acid content [19]. Although the presence of the sharp peaks in XRD, the broad amorphous peaks remains around 20º, suggesting the predominance of the amorphous nature of the electrolyte. Also in a work of CH acetate doped with NH_4Cl the broad diffraction peak around 20º suggests the amorphous nature of the electrolytes, and the appearance of salt's sharp peaks doesn't affect the change of the broad amorphous phase around 20º [16]. In summary, the increase in glycerol amount promotes an increase in the amorphous portion and makes the samples more conductive, and these results agree with the conductivity values.

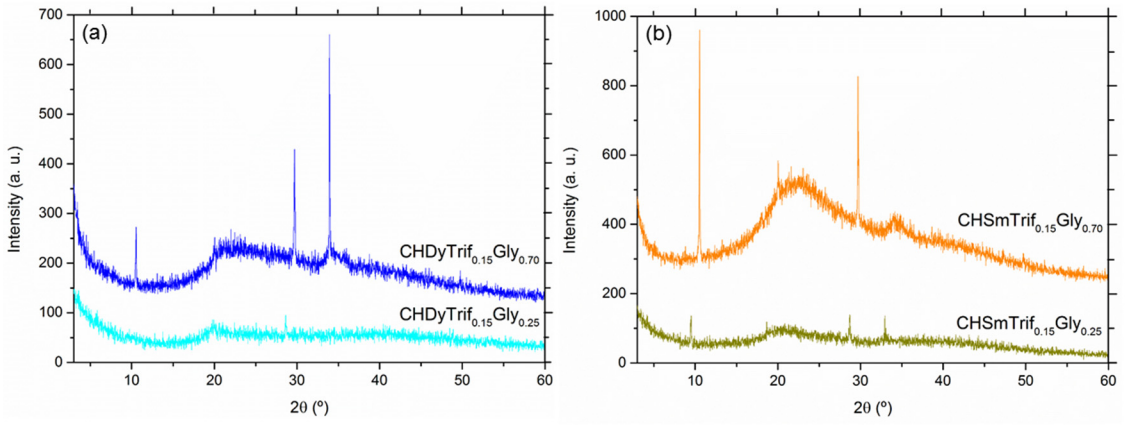

Figure 7.6 XRD diffractograms of (a) $CHDyTrif_{0.15}Gly_y$ (y = 0.25 or 0.70 g), and (b) $CHSmTrif_{0.05}Gly_y$ (y = 0.25 or 0.70 g) based electrolytes.

SEM micrographs were obtained with the magnification of 500 x and 5.00 kx and these pictures evidence different surface morphologies depending on the salt and glycerol amount. Practically all samples exhibited good homogeneity, good surface uniformity, and also some irregularities, Figure 7.7. Besides these irregularities, no other phase separation on sample's surface is observed indicating that glycerol was uniformly incorporated in the samples formulation. Touch test of the samples also evidenced dry surface and no glycerol exudation process. The surface's irregularities and the white points observed may be related with some salt located outside the sample, and reveals the occurrence of small crystalline regions, as suggested by XRD results. On another hand, the samples with higher glycerol amount also presented some cracks an imperfections on their surfaces. The presence of cracks was consistent with poor mechanical properties, as already demonstrated in a study of gelatin/$LiBF_4$-based polymer electrolytes plasticized

with glycerol [20]. Finally, all the obtained samples were slightly yellow but translucent and showed good adhesion properties.

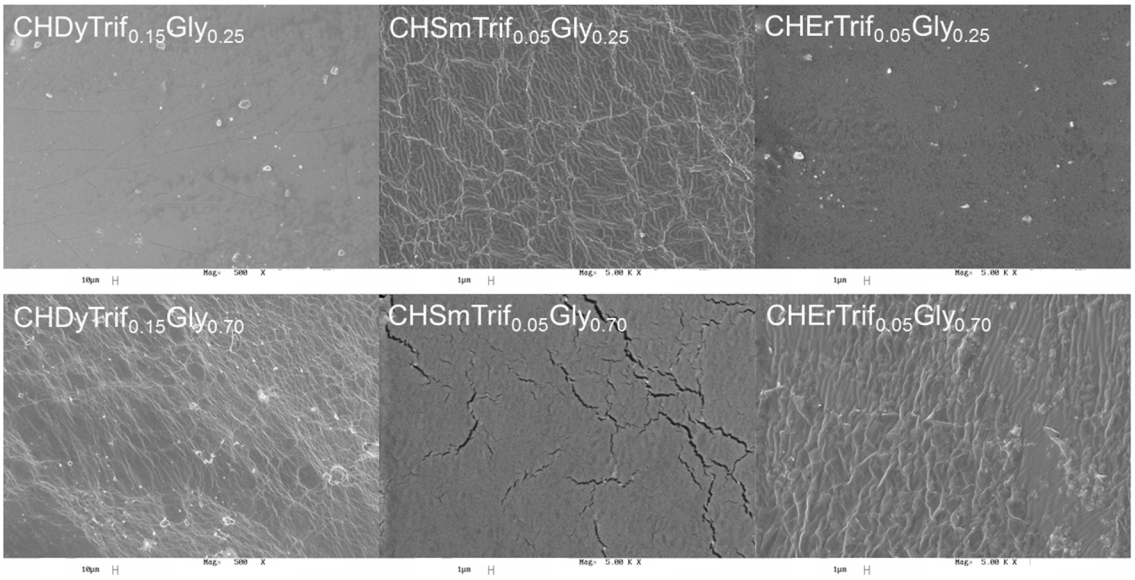

Figure 7.7 SEM micrographs of CHLnTrif$_x$Gly$_y$-based electrolytes, for Ln= Dy, Sm or Er, x = 0.05 or 0.15 g, and y = 0.25 or 0.70 g.

The AFM analyses were used to evaluate the morphology and changes on the surface topography of the samples. Figure 7.8 displays AFM images and roughness values of the samples with different salt amounts with scanning area of 2.0 µm x 2.0 µm. In the samples with different glycerol amounts, the increase in glycerol quantity promoted and increase in conductivity and a decrease in roughness values. The plasticizer help in dissociating ions, decrease the crystallinity, and increasing the molecular motion, which leads to an enhancement in conductivity values. In this case, the roughness decreased from 16.9 nm, in the sample with 0.25 g of glycerol (CHErTrif$_{0.05}$Gly$_{0.25}$), to 8.67 nm for the electrolyte with 0.70 g of glycerol (CHErTrif$_{0.05}$Gly$_{0.70}$). In thin films the roughness of the samples promotes an incomplete contact between the electrode and the electrolyte [21]. In these cases, the contact area is not continuous and consists of many discrete points contacts, and so the current not pass the whole cross-section, which leads to the conductivity decrement.

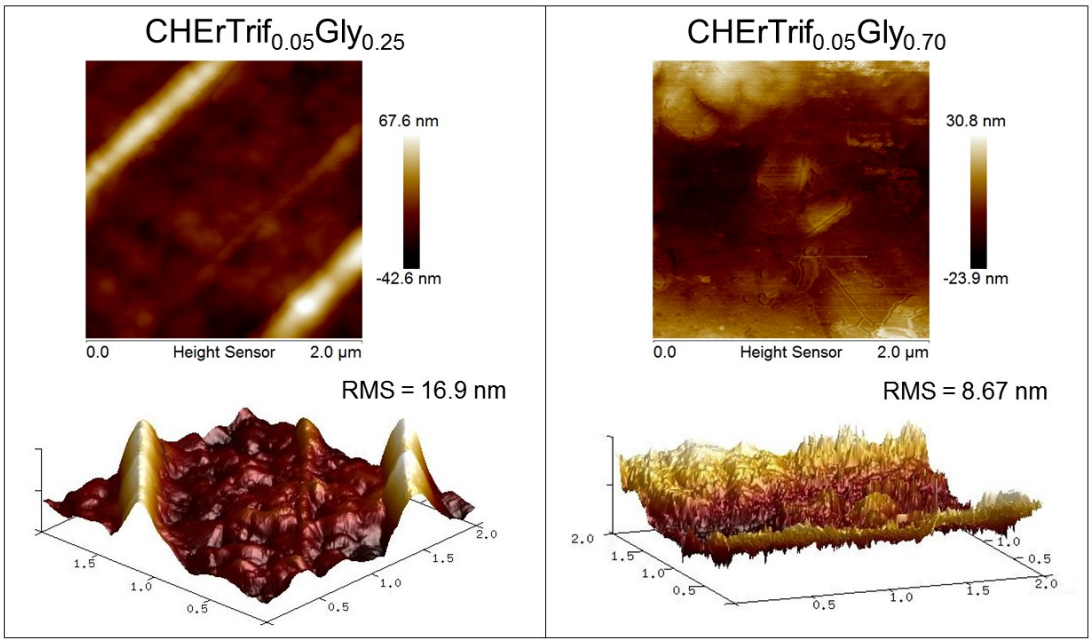

Figure 7.8 AFM images of CHErTrif$_{0.05}$Gly$_y$-based electrolytes for y = 0.25 or 0.70 g.

7.3.4. Electrochromic devices

Because of the highest, but still modest, conductivity values, the samples with more glycerol amount were chosen to assemble 2 cm^2 electrochromic devices with glass/ITO/PB or WO_3/CHLnTrif$_x$Gl$_y$/CeO_2-TiO_2/ITO/glass configuration.

7.3.4.1. ECDs with WO_3

Figure 7.9 shows the results of the charge density measured during 10th and 500th cycles for the ECDs with WO_3. In ECD with DyTrif, Figure 7.9 (a), for the 10th cycle, the inserted charge at -2.8 V reaches -3.0 mC cm^{-2} in 15 s, and for the 500th cycle the charge density decreases to -0.8 mC cm^{-2}. In the case of the ECD with SmTrif, Figure 7.9 (b), for the 10th cycle the inserted charge at -2.8 V reaches -1.5 mC cm^{-2} in 15 s. However, for the 500th cycle a reduction to -0.5 mC cm^{-2} is observed. In the ECD with CeTrif (not shown here) a decrease of the charge density from -3.5 to -2.8 mC cm^{-2} was observed after 200 color/bleaching cycles. The charge density value for the initial sweeps were higher than -1.8 mC cm^{-2} at -2.5 V reported for the ECD with DNA-based electrolytes [22], similar to -4.0 mC cm^{-2} at -2.0 V for ECD with DNA Er^{3+} [23], but lower than -6.6 mC cm^{-2} at -3.5 V for reported elsewhere [24]. This decrease can be attributed to the

incomplete extraction of the inserted charge, which leads to the decrease of the device reversibility. A not complete charge extraction is also seen in both curves, as the inserted charge is greater that extracted one. The charge decrease on cycling might be related to the degradation of the interfacial contact between the electrolyte and the conducting materials, which is attributed to the volumetric change caused by the expansion and shrinkage of the active materials. This could lead to an increase in the charge transfer resistance too. Additionally, due to the formation of passive films of ions of salt during charge/discharge cycles the activation of these ions decreased as the cycle test was repeated. Another explanation for this decrease of the reversibility can be due to the non-perfect nanoporous structure of the WO_3 and CeO_2-TiO_2 thin films, where the charges accommodate during the insertion and extraction processes. The charge extraction occurs faster and, for DyTrif and SmTrif, the ECD is already transparent after applying +2.8 V potential for 2 s. This extraction is comparable to the ECD with gelatin-based electrolyte [25]. As mentioned above, the negative voltage application onto electrochromic coating layer of the ECD leads to the coloration of the device to blue color, which is associated with WO_3 reduction because of simultaneous electrons and ions insertion, accordingly to equation 1.4. The inversion of the applied voltage to +2.8 V results in the bleaching of the device due to WO_3 oxidation and ions deintercalation. Similar results were obtained with ECD containing agar and europium picrate, where in coloured state (blue), the WO_3 was reduced by simultaneous europium ions and electrons insertion, and in bleached state (light yellow), both the salt ions and electrons were extracted [18].

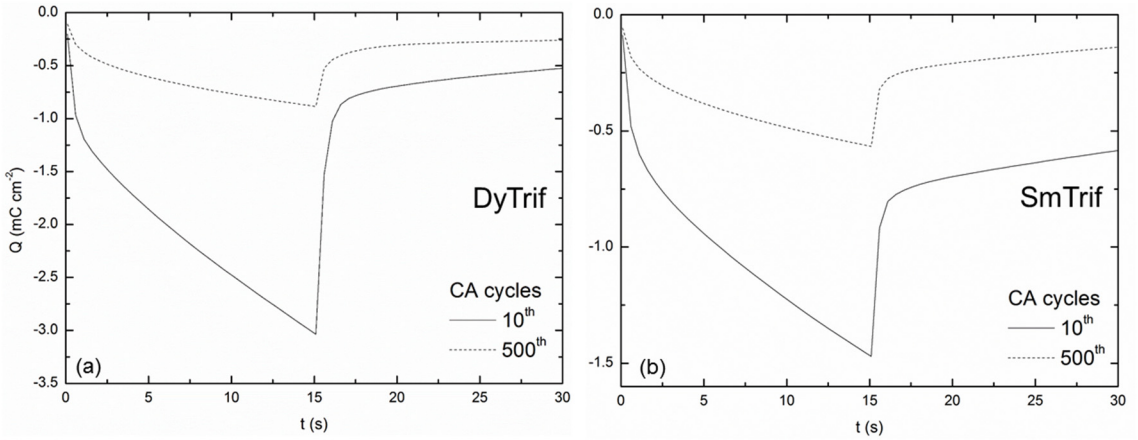

Figure 7.9 Charge density of the ECD with glass/ITO/WO_3/CHLnTrif$_x$Gly$_{0.70}$/CeO_2-TiO_2/ITO/glass configuration, for LnTrif$_x$ = DyTrif$_{0.15}$ (a) and SmTrif$_{0.05}$ (b).

Figure 7.10 (a) shows the cyclic voltammograms of the ECD with DyTrif measured during 10^{th} and 500^{th} cycles. The voltammogram of the 10^{th} cycle presented two cathodic peaks: a main peak at -1.4 V and the second one at 0.0 V, and two anodic peaks centered at -0.4 and 1.2 V. The cathodic process is due to the reduction of the WO_3 and is accompanied by its blue coloration, while the anodic peaks are attributed to the bleaching of the device. The successive voltammetric cycles promote changes in the voltammograms, namely, the current density decreases and the cathodic peaks shift to more positive potentials. As in ECD with the configuration Nb_2O_5/gelatin-electrolyte/$(CeO_2)_{0.81}$-TiO_2 the shape of the CV does not change drastically and the two oxidation observed processes can be due to the presence of the residual water in the electrolyte [26]. Typical cyclic voltammograms of the ECD with SmTrif, recorded during the 10 and 500^{th} chronoamperometric cycles at 100 mVs^{-1}, are shown in Figure 7.10 (b). A large cathodic peak is observed at -1.2 V, and a large anodic peak has its maximum centered at 0.3 V. During the first 10 cycles, there is also a small shoulder at 2.0 V associated with another oxidation process, probably due to the electrolyte used. In a study of an ECD using WO_3 as electrochromic cathodic electrode and gelatin electrolyte the voltammogram also showed a small shoulder at 0.8 V, but in this case, it was associated with another oxidation process, probably due to the LiI/I_2 used in the preparation of the electrolyte [27]. The observed cathodic peak was associated with the reduction of WO_3 and the change of color to blue. On the other hand, the reverse potential promotes anodic reactions that are attributed to the bleaching of WO_3, and the device returns to its initial state (transparent). As observed in other systems, the feature of the voltammograms does not change drastically under cycling, but the current density decreases and the cathodic and anodic peaks are slightly displaced to more positive values [28, 29].

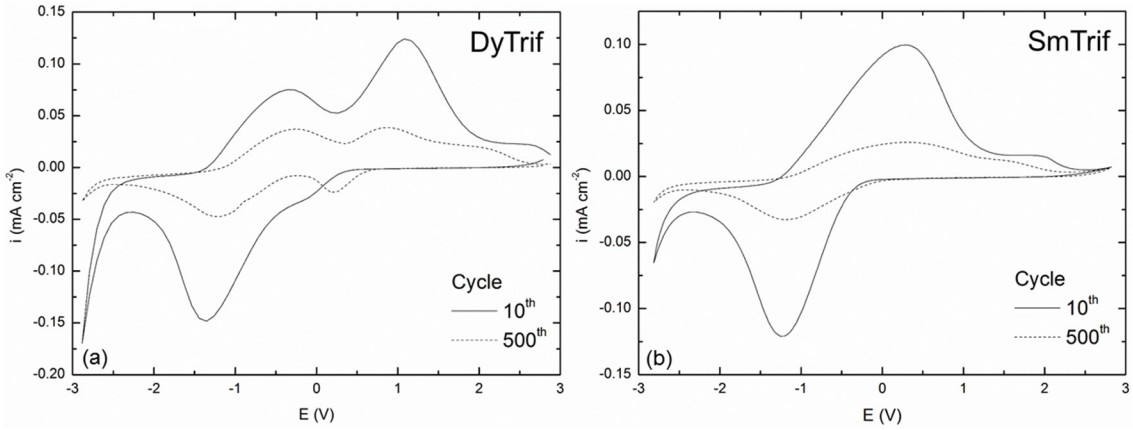

Figure 7.10 Cyclic voltammograms of the ECD with glass/ITO/WO_3/CHLnTrif$_x$Gly$_{0.70}$/CeO_2-TiO_2/ITO/glass configuration, for LnTrif$_x$ = DyTrif$_{0.15}$ (a) and SmTrif$_{0.05}$ (b).

Typical cyclic voltammograms of the ECD with Ce and SmTrif measured at different scan rates are shown in Figure 7.11. The peak potential is scan rate dependent. Figure 7.11 (a) shows cyclic voltammograms of the ECD with CeTrif, that were recorded at scan rates of 50, 100, 200, 300, and 500 mV.s^{-1}, obtained by sweeping the potential in the range of -2.0 to +2.3 V. This figure reveals that an increase of the voltammetric scan rate promotes an increase of the cathodic current to -0.9 mA cm^{-2} and also shifts the anodic peak to more positive potentials (0.5 V at 500 mV s^{-1}). In the case of the ECD with SmTrif, Figure 7.11 (b), an increase in the scan rate promotes an increase of both reduction and oxidation peaks current, and their shift to more negative and positive potentials, respectively. The cathodic peak at -1.07 V, when recorded at 50 mV s^{-1}, has a current density of -0.07 mA cm^{-2}, and it shifts to -1.71 V with current density of -0.40 mA cm^{-2} when recorded at 500 mV s^{-1}. With the anodic peak the opposite occurs, its maximum at 0.21 V and 0.06 mA cm^{-2} is registered at 50 mV s^{-1} and shifts to 0.54 V and 0.25 mA cm^{-2} when registered at 500 mV s^{-1}. The cathodic to anodic peak areas gives about 0.92 at 50 and 500 mV s^{-1}, which indicates a not completely reversible process, similarly to the situation found in a study of ECD with WO_3 and containing a DNA membrane [30].

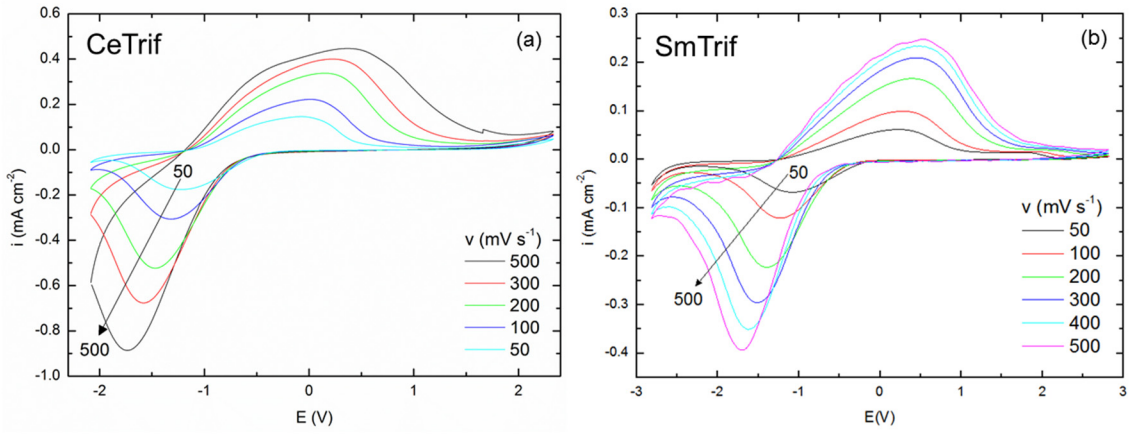

Figure 7.11 Cyclic voltammograms at different scan rates of the ECD with glass/ITO/WO_3/CHLnTrif$_x$Gly$_{0.70}$/CeO_2-TiO_2/ITO/glass configuration, for LnTrif$_x$ = CeTrif$_{0.10}$ (a) and SmTrif$_{0.05}$ (b).

For the determination of transmittance and absorbance differences the UV-vis spectra were obtained in the blue coloured and bleached states, i.e., after the application of -2.8 and +2.8 V, for the ECD with Dy and SmTrif, and after application of -2.0 and +2.3 V, for the ECD with CeTrif, during 15 s each. The ECD with WO_3 electrochromic layer is almost transparent just after assembling (Figure 7.12, black line), and after the negative potential application the device changed from almost transparent to blue color. This change in color is associated with WO_3 reduction and simultaneous positive ion insertion. The application of inverse potential promotes a return of the device to its initial state, as a result of WO_3 oxidation and cation desinsertion.

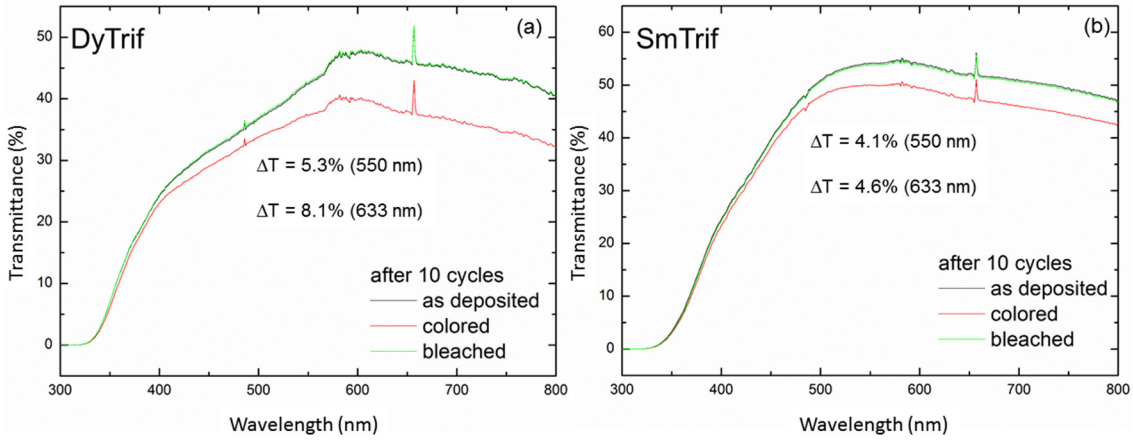

Figure 7.12 Transmittance of the ECD with glass/ITO/WO_3/CHLnTrif$_x$Gly$_{0.70}$/CeO_2-TiO_2/ITO/glass configuration, for LnTrif$_x$ = DyTrif$_{0.15}$ (a) and SmTrif$_{0.05}$ (b).

The color change (transmittance change, ΔT) and the optical density change (Δ(OD) = -log ($T_{colored}/T_{bleached}$)) at 550 and 633 nm are presented in Table 7.2. The human eye is sensitive to light waves for which the wavelength is between about 400 and 700 nm (VIS region) and so the transmittance of ECD in the 550-633 nm region was chosen [23].

Table 7.2 Transmittance change and optical density change at 550 and 633 nm.

	550 nm		663 nm	
	ΔT (%)	OD	ΔT (%)	OD
DyTrif	5.3	0.0581	8.1	0.0836
SmTrif	4.1	0.0322	4.6	0.0372
CeTrif	3.7	0.0672	5.0	0.0871

7.3.4.2. ECDs with PB

The ECD with PB was subjected to cyclic voltammetry between -2.8 and +2.8 V potentials at different scan rates from 50 to 300 or 500 mV s^{-1}, Figure 7.13. The voltammogram of PB film reveals four characteristics peaks, namely, oxidation and reduction peaks characteristics of Prussian Blue (PB), Prussian White (PW, Everitt's salt), and Prussian Green (PG, Berlin Green), accordingly to the equations 1.5 and 1.6 [31]. At 0.04 and 0.2 V the peaks are attributed to PB ↔ PW formation; the well-defined peak at +0.2 V is related to conversion of the "water insoluble PB" to "water soluble PB", and the peak at ~0.8 V is associated to the Prussian Green formation (PG ↔ PB). In ECD with DyTrif, Figure 7.13 (a), four peaks are seen but only at lower scan rates (50 and 100 mV s^{-1}), namely, two cathodic peaks at -0.75 and 0.5 V and two anodic peaks at 0.3 and 1.9 V. However, for higher scan rates three peaks, two cathodic and one anodic, are observed instead of four. In ErTrif ECD, two cathodic peaks, at -0.65 and 1.20 V and one anodic peak at 1.90 V (at scan speed of 50 and 100 mV s^{-1}) are seen in Figure 7.13 (b). In the case of the ECD with TmTrif, two cathodic peaks, at -0.75 and 1.13 V, and one anodic peak at 1.75 V (at scan speed of 50 and 100 mV s^{-1}) are seen in Figure 7.13 (c). In ECDs with DNA-Er^{3+} three peaks were also observed: two cathodic peaks at -0.8 and 0.9 V and one anodic peak at 1.0 V that can be attributed to PW, PB, and PG, respectively [32]. In

this case, the anodic peak was responsible for the blue coloration of the PB and, consequently, the ECD. The difference in peak potentials is probably due to the different electrolytes used. The increase in the scan rate does not change significantly the voltammograms shape, but peaks' shift is observed. The increase in the cathodic current is accompanied by the change of the device to bleached state (transparent), while the anodic peak is responsible for blue coloring of the device.

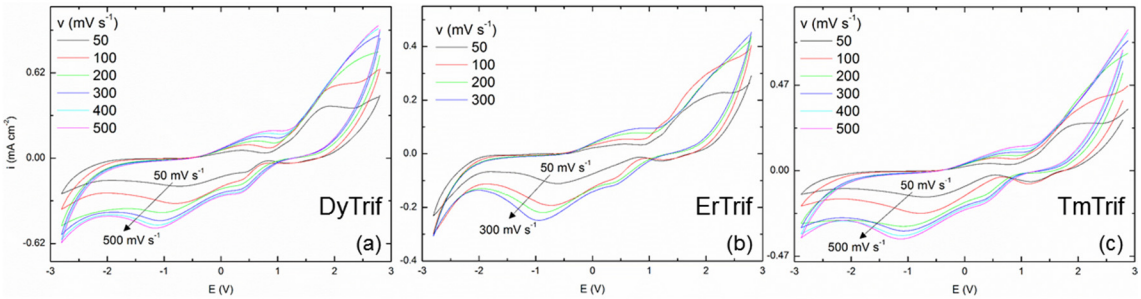

Figure 7.13 Cyclic voltammetry at different scan rates of the ECD with glass/ITO/PB/CHLnTrif$_x$Gly$_{0.70}$/CeO$_2$-TiO$_2$/ITO/glass configuration, for LnTrif$_x$ = DyTrif$_{0.15}$ (a), ErTrif$_{0.05}$ (b), and TmTrif$_{0.05}$(c).

The ECD with PB electrochromic layer is blue just after assembly (Figure 7.14, black line).

During negative potential application, a reduction of PB occurs leading to the bleaching of the device. The inverse process, coloration and/or oxidation, changes the ECD from transparent to blue. The transmittance change and optical density change at 550 and 633 nm are presented in Table 7.3.

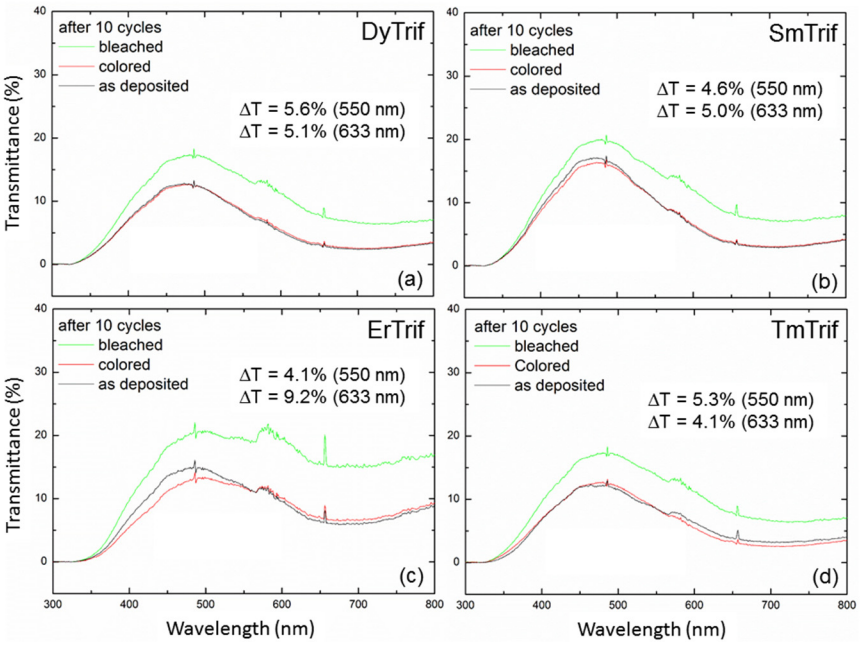

Figure 7.14 Transmittance of the ECDs with glass/ITO/PB/CHLnTrif$_x$Gly$_{0.70}$/CeO$_2$-TiO$_2$/ITO/glass configuration, for LnTrif$_x$ = DyTrif$_{0.15}$ (a), SmTrif$_{0.05}$ (b), ErTrif$_{0.05}$ (c), and TmTrif$_{0.05}$ (d).

Table 7.3 Transmittance change and optical density change at 550 and 633 nm.

	550 nm		663 nm	
	ΔT (%)	OD	ΔT (%)	OD
TmTrif	5.3	0.210	4.1	0.290
ErTrif	4.6	0.160	5.0	0.344
SmTrif	4.1	0.209	9.2	0.371
DyTrif	5.6	0.222	5.1	0.391

Although in both cases (with WO_3 and PB) the values are not very high, the color change difference is clearly visible in almost whole visible spectral range from 450 to 800 nm. In conclusion, these results show that the electrolytes with higher glycerol amount are promising electrolytes to be applied in this kind of applications, but the performance of the ECDs needs to be investigated in more depth.

7.4. Conclusion

A family of lanthanides triflate doped CH materials and containing different glycerol amounts was prepared by solvent casting method, and the behavior of the samples was evaluated. As expected, an increase in glycerol amount promotes an increase of ionic conductivity by 1 or 2 orders of magnitude. On another hand, the activation energy is lower for the samples with higher plasticizer amount. These results are in very good agreement because the lower energy barrier results in easier ionic movement. The differences in the minimum decomposition temperature and in the stages obtained from the TGA results may be due to the different interactions of salt and glycerol with the polysaccharide chain, and also due to the different salt and plasticizer amount used to prepare the electrolytes. The first stage was more pronounced for the samples with higher glycerol amount, and so it may be related to the degradation of the plasticizer. The second step may be due to a complex process including depolymerization, dehydration of the saccharide rings, and decomposition of units of polymer. The third and last stage increases in the samples with less glycerol amount and it is more perceptible in electrolytes with more salt amount. From DSC results, no T_g was observed and this is an indication that the samples are predominantly amorphous. Also in XRD, the broad peak observed around 20º suggests the amorphous nature of the electrolytes. SEM micrographs evidence different surface morphologies depending on the salt and glycerol amount, and practically all samples exhibited good homogeneity, good surface uniformity, and also some irregularities. Besides these irregularities, no other phase separation on sample's surface is observed indicating that glycerol was uniformly incorporated in the samples formulation. In the samples with different glycerol amounts, the increase in glycerol quantity promoted and increase in conductivity and a decrease in roughness values. In thin films the roughness of the samples promotes an incomplete contact between the electrode and the electrolyte, which leads to the conductivity decrement. Finally, the samples with higher glycerol amount, that shown the highest, but still modest, conductivity values, were chosen to assemble small electrochromic devices. In the device with WO_3, the negative voltage application onto electrochromic coating layer of the ECD leads to the coloration of the device to blue color, which is associated with WO_3 reduction because of simultaneous electrons and ions insertion. The inversion of the applied voltage results in the bleaching of the device due to WO_3 oxidation and ions deintercalation. In the successive voltammetric cycles, the feature of the voltammograms does not change

drastically, but the current density decreases and the cathodic and anodic peaks are slightly displaced to more positive values. The ECD with WO_3 electrochromic layer is almost transparent just after assembling, and after the negative potential application the device changed from almost transparent to blue color. This change in color is associated with WO_3 reduction and simultaneous positive ion insertion. The application of inverse potential promotes a return of the device to its initial state, as a result of WO_3 oxidation and cation desinsertion. The increase in the cathodic current is accompanied by the change of the device to bleached state (transparent), while the anodic peak is responsible for blue coloring of the device, in the device with PB. During negative potential application, a reduction of PB occurs leading to the bleaching of the device. The inverse process, coloration and/or oxidation, changes the ECD from transparent to blue. In both cases, the increase in the scan rate does not change significantly the voltammograms shape, but peaks' shift is observed. The ΔT varies between 3.7 - 5.3 % and 4.6 - 8.1 % at 550 and 663 nm, respectively, for the devices with WO_3, and between 4.1 - 5.6 % and 4.1 - 9.2 % at550 and 663 nm, respectively, for the ECDs with PB. Although in both cases the transmittance change and optical density change are not very high, the color change difference is clearly visible in almost whole visible spectral range. So, the results show that the electrolytes with higher glycerol amount are promising electrolytes to be applied in this kind of applications, but the performance of the ECDs needs to be investigated in more depth.

7.5. References

[1] A. Pawlicka, M. Danczuk, W. Wieczorek, E. Zygadło-Monikowska, Influence of plasticizer type on the properties of polymer electrolytes based on chitosan, The Journal of Physical Chemistry A, 112 (2008) 8888-8895.

[2] S. Gupta, P.K. Varshney, Effect of plasticizer concentration on structural and electrical properties of hydroxyethyl cellulose (HEC)-based polymer electrolyte, Ionics, 23 (2017) 1613-1617.

[3] X. Ma, J. Yu, K. He, N. Wang, The effects of different plasticizers on the properties of thermoplastic starch as solid polymer electrolytes, Macromolecular Materials and Engineering, 292 (2007) 503-510.

[4] K. Mishra, S.S. Pundir, D.K. Rai, Effect of polysorbate plasticizer on the structural and ion conduction properties of PEO-NH_4PF_6 solid polymer electrolyte, Ionics, 23 (2017) 105-112.

[5] A. Firmino, J.G. Grote, F. Kajzar, J.-C. M'Peko, A. Pawlicka, DNA-based ionic conducting membranes, Journal of Applied Physics, 110 (2011) 033704 (5pp).

[6] A. Al-Kahlout, D. Vieira, C.O. Avellaneda, E.R. Leite, M.A. Aegerter, A. Pawlicka, Gelatin-based protonic electrolyte for electrochromic windows, Ionics, 16 (2010) 13-19.

[7] G.O. Machado, H.C.A. Ferreira, A. Pawlicka, Influence of plasticizer contents on the properties of HEC-based solid polymeric electrolytes, Electrochimica Acta, 50 (2005) 3827-3831.

[8] J.R. Andrade, E. Raphael, A. Pawlicka, Plasticized pectin-based gel electrolytes, Electrochimica Acta, 54 (2009) 6479-6483.

[9] L.S. Ng, A.A. Mohamad, Protonic battery based on a plasticized chitosan-NH_4NO_3 solid polymer electrolyte, Journal of Power Sources, 163 (2006) 382-385.

[10] R. Alves, L.P. Ravaro, A. Pawlicka, M.M. Silva, A.S.S. de Camargo, Eco-Friendly Luminescent Hybrid Materials Based on Eu^{III} and Li^{I} Co-Doped Chitosan, Journal of the Brazilian Chemical Society, 26 (2015) 2590-2597.

[11] M.F. Shukur, R. Ithnin, M.F.Z. Kadir, Electrical properties of proton conducting solid biopolymer electrolytes based on starch-chitosan blend, Ionics, 20 (2014) 977-999.

[12] R.C. Sabadini, V.C.A. Martins, A. Pawlicka, Synthesis and characterization of gellan gum: chitosan biohydrogels for soil humidity control and fertilizer release, Cellulose, 22 (2015) 2045-2054.

[13] S.F. Wang, L.J. Shen, Y. Tong, L. Chen, I.Y. Phang, P.Q. Lim, T.X. Liu, Biopolymer chitosan/montmorillonite nanocomposites: preparation and characterization, Polymer Degradation and Stability, 90 (2005) 123-131.

[14] S.C. Nunes, R.F.P. Pereira, N. Sousa, M.M. Silva, P. Almeida, F.M.L. Figueiredo, V. de Zea Bermudez, Eco-Friendly Red Seaweed-Derived Electrolytes for Electrochemical Devices, Advanced Sustainable Systems, 1 (2017) (17pp).

[15] R. Alves, F. Sentanin, R.C. Sabadini, A. Pawlicka, M.M. Silva, Innovative electrolytes based on chitosan and thulium for solid state applications: Synthesis, structural, and thermal characterization, Journal of Electroanalytical Chemistry, 788 (2017) 156-164.

[16] J.F. Du, Y. Bai, W.Y. Chu, L.J. Qiao, Synthesis and performance of proton conducting chitosan/NH_4Cl electrolyte, Journal of Polymer Science Part B: Polymer Physics, 48 (2010) 260-266.

[17] D.F. Vieira, C.O. Avellaneda, A. Pawlicka, Conductivity study of a gelatin-based polymer electrolyte, Electrochimica Acta, 53 (2007) 1404-1408.

[18] E. Lima, E. Raphael, F. Sentanin, L.C. Rodrigues, R.A.S. Ferreira, L.D. Carlos, M.M. Silva, A. Pawlicka, Photoluminescent polymer electrolyte based on agar and containing europium picrate for electrochemical devices, Materials Science and Engineering: B, 177 (2012) 488-493.

[19] I.A. Fadzallah, S.R. Majid, M.A. Careem, A.K. Arof, A study on ionic interactions in chitosan-oxalic acid polymer electrolyte membranes, Journal of Membrane Science, 463 (2014) 65-72.

[20] D.F. Vieira, A. Pawlicka, Optimization of performances of gelatin/$LiBF_4$-based polymer electrolytes by plasticizing effects, Electrochimica Acta, 55 (2010) 1489-1494.

[21] E. Wanzenberg, F. Tietz, D. Kek, P. Panjan, D. Stöver, Influence of electrode contacts on conductivity measurements of thin YSZ electrolyte films and the impact on solid oxide fuel cells, Solid State Ionics, 164 (2003) 121-129.

[22] A. Pawlicka, F. Sentanin, A. Firmino, J.G. Grote, F. Kajzar, I. Rau, Ionically conducting DNA-based membranes for eletrochromic devices, Synthetic Metals, 161 (2011) 2329-2334.

[23] R. Leones, M. Fernandes, F. Sentanin, I. Cesarino, J.F. Lima, V. de Zea Bermudez, A. Pawlicka, C.J. Magon, J.P. Donoso, M.M. Silva, Ionically conducting Er^{3+}-doped DNA-based biomembranes for electrochromic devices, Electrochimica Acta, 120 (2014) 327-333.

[24] A. Pawlicka, A. Firmino, D. Vieira, F. Sentanin, J.G. Grote, F. Kajzar, Gelatin-and DNA-based ionic conducting membranes for electrochromic devices, Proceedings of SPIE, 2009, pp. 74870J.

[25] E. Lima, R. Mattos, F. Sentanin, L.C. Rodrigues, M.M. Silva, R.A.S. Ferreira, L.D. Carlos, A. Pawlicka, Functional novel polymer electrolytes containing europium picrate, Materials Research Innovations, 15 (2011) s3-s7.

[26] C.O. Avellaneda, D.F. Vieira, A. Al-Kahlout, S. Heusing, E.R. Leite, A. Pawlicka, M.A. Aegerter, All solid-state electrochromic devices with gelatin-based electrolyte, Solar Energy Materials and Solar Cells, 92 (2008) 228-233.

[27] L. Ponez, F.C. Sentanin, S.R. Majid, A.K. Arof, A. Pawlicka, Ion-conducting membranes based on gelatin and containing LiI/I_2 for electrochromic devices, Molecular Crystals and Liquid Crystals, 554 (2012) 239-251.

[28] R. Alves, F. Sentanin, R.C. Sabadini, A. Pawlicka, M.M. Silva, Influence of cerium triflate and glycerol on electrochemical performance of chitosan electrolytes for electrochromic devices, Electrochimica Acta, 217 (2016) 108-116.

[29] R. Leones, F. Sentanin, L.C. Rodrigues, R.A.S. Ferreira, I.M. Marrucho, J.M.S.S. Esperança, A. Pawlicka, L.D. Carlos, M.M. Silva, Novel polymer electrolytes based on gelatin and ionic liquids, Optical Materials, 35 (2012) 187-195.

[30] M. Mîndroiu, R.G. Zgârian, F. Kajzar, I. Rău, H.C.L. De Oliveira, A. Pawlicka, G.T. Tihan, DNA-based membranes for potential applications, Ionics, 21 (2015) 1381-1390.

[31] L.M.N. Assis, L. Ponez, A. Januszko, K. Grudzinski, A. Pawlicka, A green-yellow reflective electrochromic device, Electrochimica Acta, 111 (2013) 299-304.

[32] L.M.N. Assis, R. Leones, J. Kanicki, A. Pawlicka, M.M. Silva, Prussian blue for electrochromic devices, Journal of Electroanalytical Chemistry, 777 (2016) 33-39.

Chapter 8

A study on properties of chitosan-PEO electrolyte containing europium salt

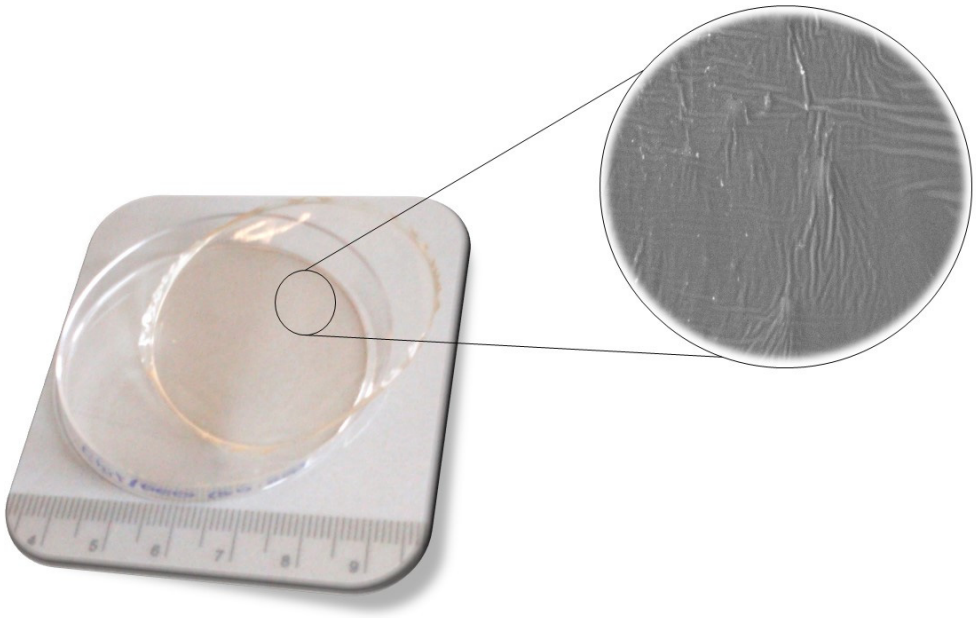

This chapter was adapted from: R. Alves, R. C. Sabadini, A. Pawlicka, M. M. Silva, A Study on Properties of Chitosan-PEO Electrolyte Containing Europium Salt, Molecular Crystal and Liquid Crystals 655 (2017) 79-86. (DOI: 10.1080/15421406.2017.1361301)

8.1. Objective

The main objective of this chapter is verify the effect of the blending of polymers. So, CH and PEO powders were mixed in different ratios, and a fixed amount of europium triflate and glycerol were added to each mixture.

8.2. Experimental

The PEs were prepared by the solvent cast technique. CH and PEO powders were mixed in different ratios and a fixed amount of europium salt and glycerol was added to each mixture. The composition and designation of the samples are listed in Table 8.1 and the synthesis scheme and the physical appearance of the samples are presented in Figure 8.1. The synthesis of the samples is very similar to that used in the preparation of CH-based electrolytes [1], and according to the chapter 2. The thickness of the samples varied between 0.128 and 0.165 ± 0.001 mm.

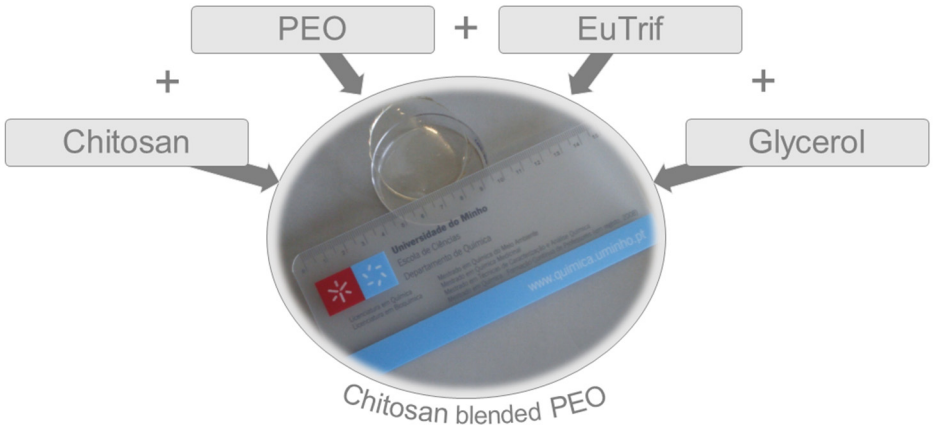

Figure 8.1 Synthesis scheme and the physical appearance of the prepared samples.

Table 8.1 Composition and designation of samples.

Composition		Designation
CH (g) (±0.00001)	**PEO (g) (±0.00001)**	**(CH:PEO)**
0.10106	0.10140	50:50
0.12169	0.08114	60:40
0.16016	0.04061	80:20

The properties of these samples were studied by TGA, SEM, XRD, and complex impedance spectroscopy.

8.3. Results and discussion

8.3.1. Thermal behavior of the electrolytes

The thermal stability of the plasticized electrolytes based on CH blended PEO and containing europium triflate was evaluated by thermogravimetric analysis of the samples upon heating. In Figure 8.2 (a) are presented TGA curves of samples and the observed stages for the degradation process may be attributed to the different interactions of the salt and plasticizer with the polysaccharides chains. In Figure 8.2 (b) one can see that the first degradation starts between 145 and 152ºC, which are considered adequate for solid-state electrochemical devices under normal conditions. The degradation process ends at about 500ºC and continues slowly as the temperature is increased up to 900ºC. The remaining residues of these samples represent about 8.3 - 21% of the starting materials and they are relatively lower than those obtained in a system of CH doped with europium triflate [2].

In DTGA curve of the sample with 80:20 composition, Figure 8.2 (c), two main peaks are observed: the first at 244ºC and the second one at about 418ºC. The peak at 244ºC may be related to the decomposition of CH, while the second, at about 418ºC, can be due to the degradation of PEO. In a study of pure CH and pure PEO, the DTGA curves exhibit a peak at about 240 and 425ºC, respectively [3]. The peak at 240ºC corresponds to thermal and oxidative decomposition of CH, vaporization, and elimination of volatile products. The peak at 425ºC is associated to the total degradation of PEO. The differences in peak position in relation to the present study are probably due to the composition of the samples, and to the salt and plasticizer added to the blended matrix, which probably act as catalyst for polymeric chains disintegration.

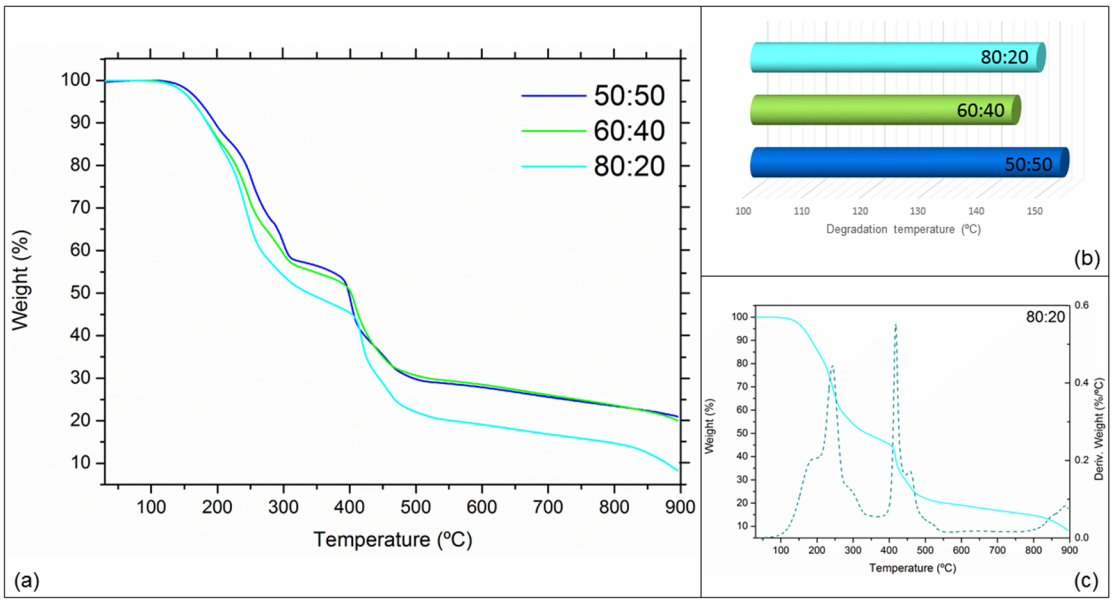

Figure 8.2 (a) TGA curves and (b) degradation temperatures of CH-PEO samples with 50:50, 60:40, and 80:20 compositions; (c) TGA and DTGA curves of sample with 80:20 composition.

8.3.2. Morphology and structure

The samples' surface morphology was studied by SEM, and the obtained results are presented in Figure 8.3. According to SEM micrographs in Figure 8.3 (a) and (b), the surface of samples seems to be homogeneous, with good surface uniformity, and with no obvious phase separation. The CH-PEO compositions 50:50 (Figure 8.3 (a)) and 60:40 (Figure 8.3 (b)) show very similar surface, which may explain the similar conductivity results obtained. On the other hand, the CH-PEO sample with 80:20 composition presents some white points (Figure 8.3 (c)) that are probably due to undissolved polymer or salt. In electrolytes containing CH and a mixture of two salts (europium and lithium triflate), the presence of clearer lines at the surface can be either related to undissolved or recrystallized salt [4]. In a study of CH doped with ionic liquids the observed micro-vesicles are probably due to undissolved polymer or glycerol [5].

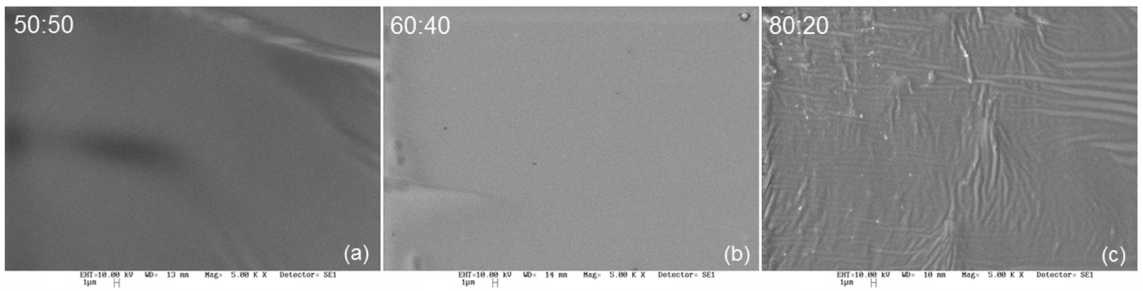

Figure 8.3 SEM micrographs of CH-PEO samples with (a) 50:50, (b) 60:40 and (c) 80:20 compositions.

Figure 8.4 (a-c) depicts X-ray diffraction patterns of salt, polymers' powders, and SPEs films. The europium salt powder, Figure 8.4 (a), presents very crystalline peaks. The PEO powder, Figure 8.4 (b), exhibits two more intense peaks at $2\theta = 19.2$ and 23.4º, and other weaker crystalline peaks that confirms the semi-crystalline structure of the polymer. In the case of the CH powder, two broad peaks at $2\theta = 9.42$ and 20.0º are observed. These results are in good agreement with those obtained for pure PEO and pure CH films [6]. In relation to CH-PEO electrolytes, the sample with 60:40 composition do not display major peaks in the diffractograms (Figure 8.4 (c)). This indicates that this electrolyte is more amorphous than others, and corroborates with SEM results. XRD traces of two other samples with 50:50 and 80:20, there are observed some small peaks. When comparing the XRD patterns of these electrolytes, Figure 8.4 (c), with the europium salt patterns, Figure 8.4 (a), it can be concluded that these peaks may be attributed to the salt. Furthermore, this indicates that europium triflate is not totally accommodated in polymeric blend matrix, and this is in good agreement with SEM results. In a study of (CH-PEO)-NH_4I electrolytes, the presence of small peaks is attributed to the salt, indicating that the salt is not totally dissolved in the blended matrix [6].

Both SEM and XRD results seem to be in good agreement with the conductivity values discussed in the below section.

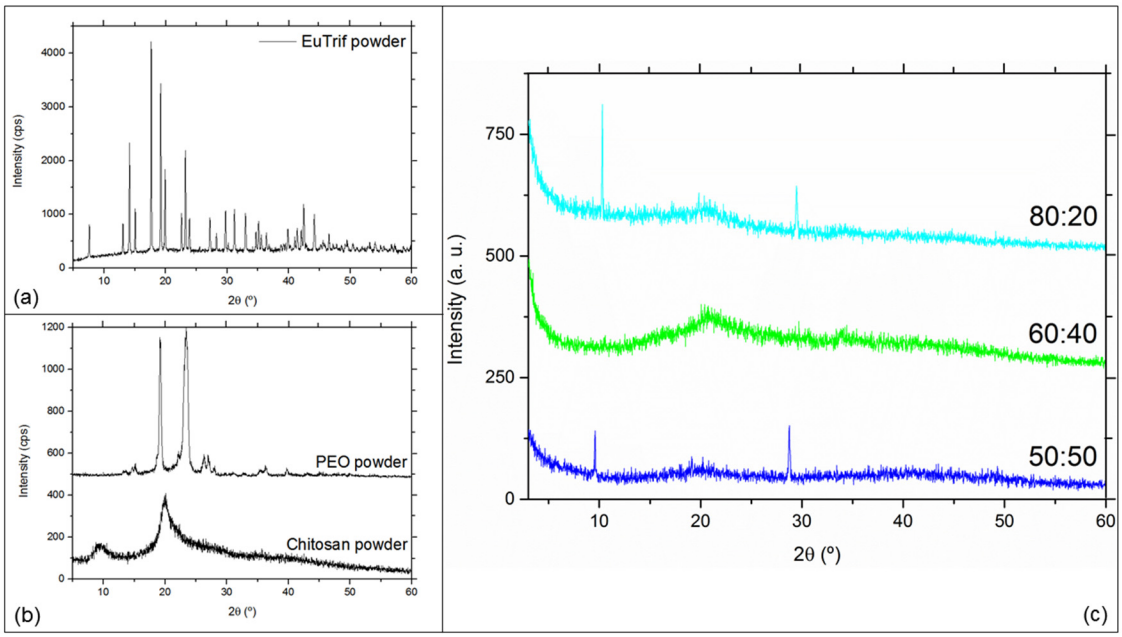

Figure 8.4 XRD patterns of (a) europium triflate, (b) CH and PEO powders, and (c) CH-PEO electrolytes doped with europium triflate.

8.3.3. Impedance spectroscopy

The results of ionic conductivity as a function of temperature for plasticized CH-PEO samples doped with europium triflate are presented in Figure 8.5. The ionic conductivity was calculated using the value of bulk resistance (R_b) at the intercept of the semi-circle with the real axis of the Nyquist plot, and according to equation (8.1):

$$\sigma = \frac{t}{A \times R_b} \tag{8.1}$$

where t is the thickness of the sample and A is the contact area between the electrolyte and the electrode. It is known that the ionic conductivity depends on several factors such as, ionic conducting species concentration, cationic or anionic types of charge carriers, charge carriers' mobility, and the temperature [7]. In relation to the temperature, and as one can observe in Figure 8.5, for all samples, an increase in temperature promotes an increase in the ionic conductivity values. Analyzing the ionic conductivity values in the table of the Figure 8.5, the samples with compositions 50:50 and 60:40 presented very

similar values, which corroborates with SEM results. In the case of the sample CH-PEO 80:20 a decrease in ionic conductivity may be related to the fact that the salt could not be totally accommodate in the matrix, which is in good agreement with SEM and XRD results. The sample CH-PEO 50:50 shows the highest conductivity of 1.92×10^{-8} S cm^{-1} at 30ºC. This value is two orders of magnitude lower than 1.40×10^{-6} S cm^{-1} at room temperature obtained for CH/PEO blend containing 30 wt% LiTFSI [8]. The difference in the obtained values may be related to the kind of salt used, since the lanthanide ions used in the present study are larger than lithium ions, which difficult the charge carriers' mobility and leads to a decrease in ionic conductivity.

As mentioned above, the conductivity seems to increase with the temperature and the Arrhenian log σ vs 1000/T relationship has been observed. When temperature dependent conductivity plot is Arrhenian, it indicates that the ionic conduction is via hopping mechanism and can be described by equation (8.2) [9]:

$$\sigma = \sigma_0 \exp\left(\frac{-E_a}{RT}\right) \tag{8.2}$$

where σ_0 is the pre-exponential factor, E_a is the apparent activation energy for ion transport, R is the gas constant (8.314 J mol^{-1} K^{-1}), and T is the temperature. The activation energy (E_a) can be obtained using equation (8.2) because the conductivity is thermally assisted. As seen in Figure 8.5, the film with highest conductivity has lowest E_a. Also in CH/PEO blends with LiTFSI the activation energy was evaluated using Arrhenius equation, and the film with highest conductivity has lowest E_a [10]. The activation energy is the required energy for the movement of the ions from one donor site to another in conduction path [11]. The decrease of E_a with increasing conductivity observed in this study indicates that in high conducting sample the ions require less energy to migrate. Similar behavior was also observed in plasticized CH/PEO blend, where the higher conducting electrolyte showed lower activation energy [12].

Despite the low conductivity values obtained in relation to other systems, the remaining results of this study encourage further investigation in this kind of samples, namely creating new blend compositions to overcome this problem.

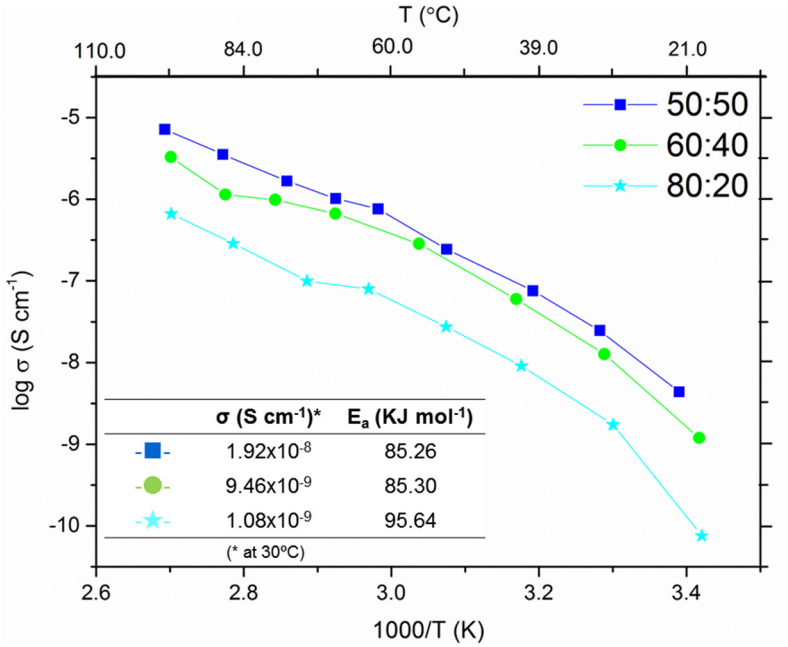

Figure 8.5 Log of conductivity plots of CH-PEO electrolytes as a function of inverse of temperature.

8.4. Conclusion

Plasticized CH-PEO electrolytes doped with europium triflate were prepared by solvent cast technique and their behavior was evaluated. The degradation temperature of the samples started at 145ºC, which is a minimum considered as adequate for electrolytes applied in solid-state electrochemical devices under normal conditions. SEM images presented homogeneous and good surface uniformity of CH-PEO samples with 50:50 and 60:40 compositions, except the one with 80:20 that had some white spots attributed to undissolved polymer and/or salt. XRD patterns of the samples revealed that the one with 60:40 composition is predominantly amorphous and others show some small crystalline peaks that may be attributed to the salt and can explain the decrease in the ionic conductivity. The sample with composition 50:50 shows the highest conductivity value of 1.92×10^{-8} S cm^{-1} at 30ºC and lowest activation energy of 85.26 kJ mol^{-1}. In the future, it would be interesting try to produce new natural-synthetic polymer SPEs compositions because TGA, SEM, and XRD results obtained in this study encourage further investigation in this kind of system.

8.5. References

[1] R. Alves, F. Sentanin, R.C. Sabadini, A. Pawlicka, M.M. Silva, Influence of cerium triflate and glycerol on electrochemical performance of chitosan electrolytes for electrochromic devices, Electrochimica Acta, 217 (2016) 108-116.

[2] R. Alves, J.P. Donoso, C.J. Magon, I.D.A. Silva, A. Pawlicka, M.M. Silva, Solid polymer electrolytes based on chitosan and europium triflate, Journal of Non-Crystalline Solids, 432 (2016) 307-312.

[3] C.G.T. Neto, J.A. Giacometti, A.E. Job, F.C. Ferreira, J.L.C. Fonseca, M.R. Pereira, Thermal analysis of chitosan based networks, Carbohydrate Polymers, 62 (2005) 97-103.

[4] R. Alves, L.P. Ravaro, A. Pawlicka, M.M. Silva, A.S.S. de Camargo, Eco-Friendly Luminescent Hybrid Materials Based on Eu^{III} and Li^{I} Co-Doped Chitosan, Journal of the Brazilian Chemical Society, 26 (2015) 2590-2597.

[5] R. Leones, R.C. Sabadini, J.M.S.S. Esperança, A. Pawlicka, M.M. Silva, Playing with ionic liquids to uncover novel polymer electrolytes, Solid State Ionics, 300 (2017) 46-52.

[6] M.H. Buraidah, L.P. Teo, C.M. Au Yong, S. Shah, A.k. Arof, Performance of polymer electrolyte based on chitosan blended with poly(ethylene oxide) for plasmonic dye-sensitized solar cell, Optical Materials, 57 (2016) 202-211.

[7] E. Raphael, C.O. Avellaneda, B. Manzolli, A. Pawlicka, Agar-based films for application as polymer electrolytes, Electrochimica Acta, 55 (2010) 1455-1459.

[8] N.H. Idris, H.B. Senin, A.K. Arof, Dielectric spectra of LiTFSI-doped chitosan/PEO blends, Ionics, 13 (2007) 213-217.

[9] M.F. Shukur, M.F.Z. Kadir, Z. Ahmad, R. Ithnin, Transport properties of Chitosan/PEO blend based proton conducting polymer electrolyte, Advanced Materials Research, 488-489 (2012) 114-117.

[10] N.H. Idris, S.R. Majid, A.S.A. Khiar, M.F. Hassan, A.K. Arof, Conductivity studies on chitosan/PEO blends with LiTFSI salt, Ionics, 11 (2005) 375-377.

[11] R. Alves, F. Sentanin, R.C. Sabadini, A. Pawlicka, M.M. Silva, Innovative electrolytes based on chitosan and thulium for solid state applications: Synthesis, structural, and thermal characterization, Journal of Electroanalytical Chemistry, 788 (2017) 156-164.

[12] M.F. Shukur, R. Ithnin, H.A. Illias, M.F.Z. Kadir, Proton conducting polymer electrolyte based on plasticized chitosan-PEO blend and application in electrochemical devices, Optical Materials, 35 (2013) 1834-1841.

Chapter 9

Conclusion

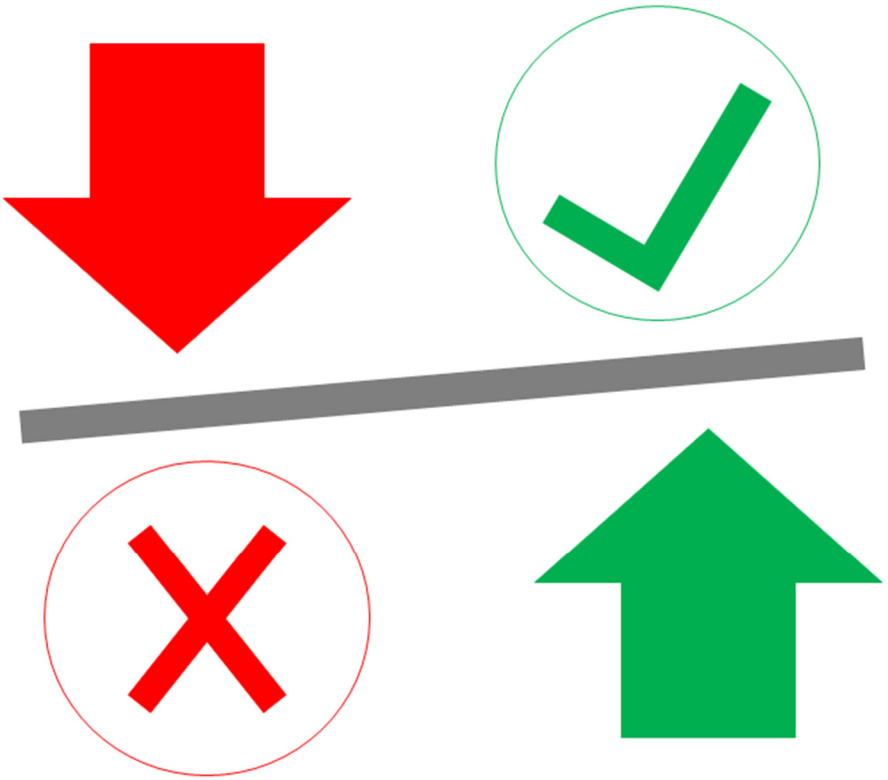

9.1. Conclusion

In the present work PEs were prepared via solvent cast method and they were characterized in terms of their thermal, morphological, structural, photophysical and conducting points of view.

To prepare a polymer electrolyte, one host polymer is required to act as a base matrix, and CH was chosen due to its high availability, and also due to its interesting properties. A main drawback of the PEs is the low ionic conductivity obtained, and so in the present work approaches such as addition of salts, mixed salt, plasticization and blend of polymers were made.

PEs containing trivalent rare earth cations can create new opportunities for innovative devices due to the luminescent behavior of the guest salt, and in this work seven different lanthanide salts, with the same triflate anion, were chosen to prepare the electrolytes. The study of different salts added to the matrix revealed that the addition of salt contributed to an increase in the thermal stability of the electrolytes, and the samples are predominantly amorphous. The ionic conductivity results showed that the conductivity values increase with the increment of temperature, and depending on the salt, the concentration, and how the ions move within the matrix, the model governing for the ionic transport can be either Arrhenius or VTF type.

The photoluminescent properties of SPEs based on CH and containing europium triflate were evaluated, and these studies indicated the characteristic emission and excitation transitions of Eu^{3+}.

A binary salt systems using lithium salt as the auxiliary component were produced in order to improve the performance of the electrolytes. These samples with mixed cations can potentially exhibit both the emission properties due to the lanthanide ions, and the conductivity due to the lithium ions. In electrolytes doped with europium and lithium salts the conductivity values are higher than those of the electrolytes singly doped with europium salt. Also the presence of lithium salt does not seem to interfere with the emissive properties. By combining the emission of the host matrix and the dopant europium ions it is possible to tune the final emission color and generate white light.

In a binary system of two salts: cerium and lithium triflates, the best ionic conductivity, 10^{-6} S cm^{-1} (at 30ºC), was obtained for the samples with 0.15 g of total salt amount.

Plasticization is one of the most effective way to enhance the conductivity, and glycerol was chosen because it is a fruitful and versatile plasticizer. As expected, an increase in glycerol amount promotes an increase in ionic conductivity, in this case, by 1 or 2 orders of magnitude, and so these samples were chosen to assemble small electrochromic devices. The devices with WO_3 are almost transparent just after assembling and after the negative potential application the devices changed from transparent to blue color. The ΔT varies between 3.7 - 5.3 % and 4.6 - 8.1 % at 550 and 663 nm, respectively. The EDCs with PB are blue color just after assembling and after the negative potential application occurs the bleaching of the devices. The ΔT varies between 4.1 - 5.6 % and 4.1 - 9.2 % at 550 and 663 nm, respectively. Although in both cases, the transmittance change values are not very high, the color change differences are clearly visible in almost whole visible spectral range, and so these samples are promising electrolytes to be applied in this kind of applications.

In plasticized chitosan-PEO blend, although the modest conductivity values, the remaining results obtained encourage further investigation in this kind of system, namely, trying to produce new natural-synthetic polymer compositions.

In general, and although the moderate conductivity values, the electrolytes developed in this work showed adequate thermal stability with predominantly amorphous morphology.

9.2 Future work

The results obtained in this work encouraging further investigation in this kind of materials. In this sense will be interesting:

- Prepare new CH:PEO blend composition;
- Select the best blend composition and prepared new samples with other salts;
- Prepare new natural-synthetic polymer blend composition, using for example, CH:PVA;
- Produce novel electrolytes with other natural polymers, such as starch, as host, and the same lanthanide ions, or ionic liquids, and verify their performance when applied in ECDs;
- Research other polymers that do not absorb in the same range of the lanthanide ions, in order to obtain new materials with luminescent properties.